Optical Fiber Sensor Technology

THOMAS G. GIALLORENZI, JOSEPH A. BUCARO, ANTHONY DANDRIDGE, G. H. SIGEL, JR., JAMES H. COLE, SCOTT C. RASHLEIGH, MEMBER, IEEE, AND RICHARD G. PRIEST

(Invited Paper)

Abstract—**The current state of the art of optical fiber sensors is reviewed. The principles of operation are detailed and the various types of fiber sensors are outlined. Achievable performance and limitations are discussed and a description of technology used to fabricate the sensor is presented. The characteristics of acoustic, magnetic, gyro, laser diode, and other sensors are described. Trends in the development of this sensor technology and expected application areas are briefly outlined.**

I. Overview and Introduction

OPTICAL fiber sensor development has matured to the point where the impact of this new technology is now evident. Fiber sensors offer a number of advantages: increased sensitivity over existing techniques, geometric versatility in that fiber sensors can be configured in arbitrary shapes, a common technology base from which devices to sense various physical perturbations (acoustic, magnetic, temperature, rotation, etc.) can be constructed, dielectric construction so that it can be used in high voltage, electrically noisy, high temperature, corrosive, or other stressing environments, and inherent compatibility with optical fiber telemetry technology. Progress in demonstrating these advantages has been substantial in the past few years with over 60 different sensor types being developed. This large number of individual devices is usually categorized into amplitude or phase (interferometric) sensors. In the former case the physical perturbation interacts with the fiber or some device attached to the fiber to directly modulate the intensity of the light in the fiber. The advantages of intensity sensors, which are described in detail in the body of this paper, are the simplicity of construction and the compatibility with multimode fiber technology. In some cases, sensitivity is traded off in order to realize these advantages. In view of the fact that extreme sensitivity is not required for most applications and that these devices are competitive with existing devices, a large market appears to exist for this class of sensor.

The phase (or interferometric) sensor, whether for magnetic, acoustic, rotation, etc., sensing, theoretically offers orders of magnitude increased sensitivity over existing technologies. In the case of the acoustic sensor constructed utilizing optical fiber interferometers, these theoretical predictions have been verified to the limit of state of the art in acoustic measurements.

Manuscript received October 13, 1981.

The authors are with the Naval Research Laboratory, Washington, DC 20375.

Additionally, other advantages have been accrued because these fiber acoustic sensors can be configured as extended elements permitting amplitude shading for sidelobe reduction, noise cancellation, and/or in fiber signal processing. In the case of the magnetic sensor, it appears that fiber sensors operating at room temperature offer detection sensitivities comparable to or exceeding cryogenic SQUID technology, which normally operate between 4 and 10 K. Phase sensors therefore satisfy a market where geometric versatility and high sensitivity are the pacing requirements.

Development of optical fiber sensors started in earnest in 1977 even though some isolated demonstrations preceded this date. During the past four years, many laboratories have entered this field resulting in rapid progress. As an example, between 1977 and 1979 demonstrated fiber acoustic sensor sensitivities improved by about 100 dB so that many of these sensors now rival or surpass previous electroacoustic performance. Magnetic, acoustic, pressure, temperature, acceleration, gyro, displacement, fluid level, torque, photoacoustic, current, and strain sensors are among the fiber optic sensor types being investigated. Since fiber sensors are constructed using dielectric materials and compatible with fiber telemetry, this technology offers unparalleled flexibility.

While progress has been rapid and many sensor types have been demonstrated, the technology is not yet fully developed nor exploited. Practical problems remain in the areas of noise sources and detection processes, in packaging, and in optimized fiber coatings. As an example, nonreciprocal noise in the fiber gyro has prevented the ultimate sensitivity from being realized. In the magnetic sensor, lengths of magnetically sensitive coated fiber are only available in short lengths (approximately 1 m) whereas kilometer lengths are desired. Finally, sensor packaging to survive the stringent conditions encountered in operational deployment has not been completed. These problems are areas of current efforts, and work in many of these problem areas has only recently been initiated so that they would not be expected at this time to be completely resolved.

This paper is designed to describe the technology, define what the current state of the art is, review a number of considerations important to those who may attempt to construct these sensors, and give the reader a feeling for the potential of this newly emerging technology. Section II discusses the most highly developed sensor to date, the acoustic sensor. A description of techniques to sensitize or desensitize fibers to acoustic fields is presented. Noise sources, frequency depen-

dent effects, and configurational response are outlined. The projected and measured performance levels are described along with a brief description of sensor packaging.

In Section III the fiber magnetic sensor is discussed. Effects of coatings and mandrels on sensitivity, frequency dependence of the sensor response, and noise sources are described. The expected performance and state of the art is presented. Section IV describes fiber optic angular rate of rotation sensors (gyroscopes). These devices promise significant increases in rotation sensing performance; however, noise problems have prevented the realization of this performance. A review of these noise considerations, the different gyro techniques and configurations demonstrated to date, and the status of the technology will be described in this section.

Amplitude sensors are presented in Section V. The operating principles, advantages, limitations, and demonstrated performance are outlined. Section VI describes diode laser sensors. These sensors utilize in most cases a three mirror laser cavity structure in which one mirror's position is affected by the field to be sensed. These sensors may or may not have fibers as part of the cavities. Noise sources, advantages, limitations, and demonstrated performance are outlined.

Acceleration, current, temperature, photoacoustic, torque, liquid level, etc., sensors are briefly discussed in Section VII. Several types use phase effects, whereas others utilize amplitude effects. These sensors are discussed in this section primarily because they are in an early state of development. While the discussion is brief, it is hoped that the references will provide additional helpful information. The final section describes technology used in support of the development of fiber sensors, particularly detection and laser technologies. The laser source imposes limitations on the performance of fiber sensors and these limitations are presented in this section. The descriptions of the various detection schemes and tradeoffs between them are also detailed so that the reader can appreciate the approaches available and the limitations of each. The paper concludes with final remarks on future directions and the expected utility of fiber optical sensor technology.

II. Fiber Optic Acoustic Sensor

Fiber Optic Interferometer

Fiber optic interferometer acoustic sensors [1], [2] generally employ the Mach-Zehnder arrangement shown in Fig. 1. A laser beam is split, with part of the beam being transmitted by a reference fiber and the other part being transmitted in a sensing fiber which is exposed to the acoustic field. In the reference arm some means is provided for either shifting the optical frequency (e.g., a Bragg modulator) or for phase modulating (e.g., a fiber stretcher [3] or integrated optic phase shifter). The two beams are recombined, allowed to interact on the surface of a photodetector, and then a suitable demodulator is employed to detect the original phase modulated signal. Various demodulation techniques can be utilized including FM discrimination [4], stabilized homodyne [3], synthetic heterodyne [5], as well as several others [6]. Actual choice of the demodulator is driven by the specific sensor application and is discussed in detail in Section VIII.

The extreme sensitivities possible with fiber interferometer

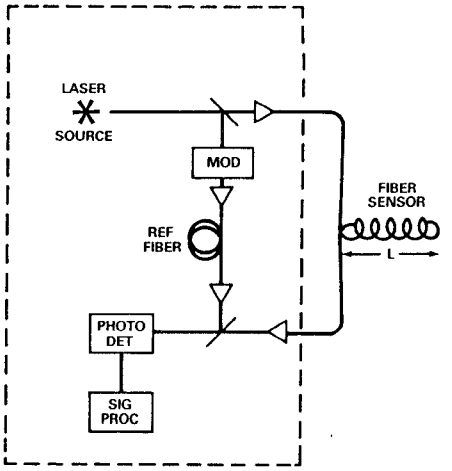

Fig. 1. Basic fiber optic interferometer.

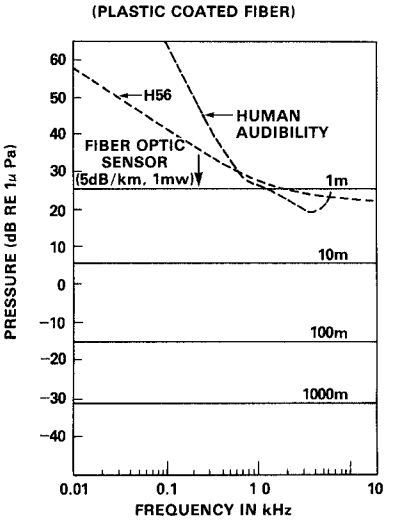

Fig. 2. Minimum detectable pressure for a shot noise-limited fiber optic acoustic sensor for various lengths of coated optical fiber (after [4]).

sensors are illustrated in Fig. 2 for the case in which the signal-to-noise is determined by the shot or quantum limit. For comparison the threshold detectability of state of the art in conventional piezoelectric sensors (H56 hydrophone) is shown as well as the threshold detectability of the human ear. As can be seen, these threshold detectabilities can be exceeded with lengths of optical fiber as short as 1 m.

One of the principal advantages possessed by fiber acoustic sensors is their geometric versatility. Some examples are shown in Fig. 3. As shown in the upper left, planar sensor elements can be fabricated which are light and flexible. Linear arrays can be made as shown in the lower left and long, single fiber elements can be made much longer than an acoustic wavelength resulting in a highly directional receiver. Alternatively, individual fiber sensors with desired properties can be placed in a line resulting in a lightweight, small linear array. As shown on the right, simple gradient sensors can be fabricated by placing the "reference" fiber (in this case a loop) adjacent to the "sensing" fiber. If the pressure sensitivities of the two loops are matched, the pair does not respond to the pressure, but to the spatial pressure gradient. Such a gradient sensor can be utilized to

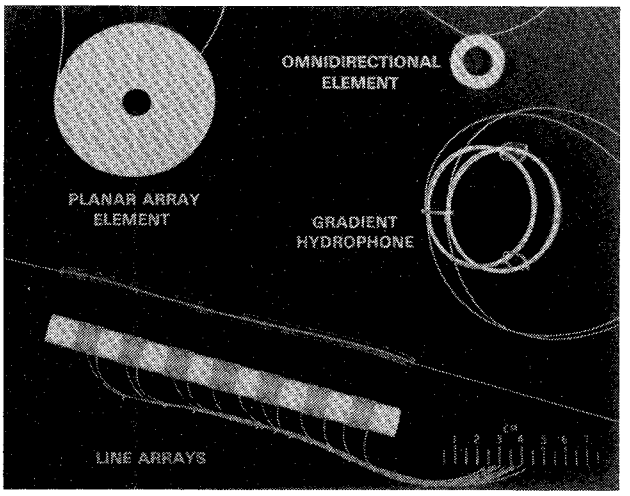

Fig. 3. Various fiber optic sensor wet ends.

detect the direction of an incident acoustic wave. As can be seen, gradient sensors can be readily made small and rugged. Most of these fiber sensors can be spatially shaded to achieve predetection signal/noise processing advantages. This is readily accomplished by varying the density of fiber windings. Finally, as illustrated in the upper right, sensitive omnidirectional elements can be made by simply keeping the size of the sensing element small compared to an acoustic wavelength.

Acoustic Sensitivity at Low Frequencies

Acoustic modulation of the phase of light propagating in a fiber is usually considered in three distinct frequency regimes which correspond to different interaction regimes between the fiber and acoustic signal. To define these regions it is useful to consider a particular sensor arrangement, for example, a loop of diameter D formed from fiber having a diameter d. At low frequencies, where the acoustic wavelength Λ is much larger than D, the acoustic wave exerts a varying hydrostatic pressure on the fiber. At intermediate frequencies, where Λ is comparable to D but still much smaller than d, pressure gradients along the sound propagation direction become important. And finally, at ultrasonic frequencies where Λ is comparable to or smaller than d, the elastic strain distribution across the fiber cross section becomes anisotropic and the optical mode distribution must be taken into account.

The pressure sensitivity of the optical phase in a fiber is defined as $\Delta\phi/\phi\Delta P$, where $\Delta\phi$ is the shift in the phase ϕ due to a pressure change ΔP. If a given pressure change ΔP results in a fiber core axial strain ϵ_z and radial strain ϵ_r, it can be shown [1] that

$$\frac{\Delta\phi}{\phi} = \epsilon_z - \frac{n^2}{2}\left[(P_{11} + P_{12})\,\epsilon_r + P_{12}\epsilon_z\right]. \tag{1}$$

Here, P_{11} and P_{12} are the elastooptic or Pockels coefficients of the core, and n is the refractive index of the core. The first term in (1) is the part of $\Delta\phi/\phi\Delta P$ which is due to the fiber length change, while the second and third terms are the parts due to the refractive index modulation of the core, which is related to the photoelastic effect [8].

A typical optical fiber is composed of a core, cladding, and a substrate, all fabricated from glasses having similar properties. The sensor fiber is usually coated with a soft rubber and then with a hard plastic. To calculate the sensitivity as given in (1), the strains in the core ϵ_z and ϵ_r must be related to properties of the various layers of the fiber. The pressure sensitivity of a fiber with one layer [7], [9] or two layers [8] has already been reported. In the following we take into account the exact geometry of a typical four-layer fiber.

At low frequencies (i.e., $\Lambda >>$ the largest dimensions of the sensor), the acoustic wave exerts a hydrostatic pressure on the fiber sensor. For sensor sizes of the order of inches, this is the case for frequencies up to several kilohertz. The polar stresses σ_r, σ_θ, and σ_z in the fiber are related to the strains ϵ_r, ϵ_θ, and ϵ_z as follows [9]:

$$\begin{bmatrix}\sigma_r^i\\ \sigma_\theta^i\\ \sigma_z^i\end{bmatrix} = \begin{bmatrix}(\lambda^i + 2\mu^i) & \lambda^i & \lambda^i\\ \lambda^i & (\lambda^i + 2\mu^i) & \lambda^i\\ \lambda^i & \lambda^i & (\lambda^i + 2\mu^i)\end{bmatrix}\begin{bmatrix}\epsilon_r^i\\ \epsilon_\theta^i\\ \epsilon_z^i\end{bmatrix} \tag{2}$$

where i is the layer index (0 for the core, 1 for the cladding, etc.) and λ^i and μ^i are the Lame parameters [10] which are related to Young's modulus E^i and Poisson's ratio ν^i as follows:

$$\lambda^i = \frac{\nu^i E^i}{(1+\nu^i)(1-2\nu^i)}, \qquad \mu^i = \frac{E^i}{2(1+\nu^i)}. \tag{3}$$

For a cylinder the strains can be obtained from the Lame solutions [11]

$$\epsilon_r^i = U_o^i + \frac{U_1^i}{r^2}\,\epsilon_o^i = U_o^i - \frac{U_1^i}{r^2}\,\epsilon_z^i = W_o^i \tag{4}$$

where U_o^i, U_1^i, and W_o^i are constants to be determined. Since the strains must be finite at the center of the core, $U_i^o = 0$.

For a fiber with m layers the constants U_o^i, U_1^i, and W_o^i in (4) are determined from the boundary conditions

$$\sigma_r^i|_{r=r_i} = \sigma_r^{i+1}|_{r=r_i}\ (i - 0, 1, \cdots, m-1), \tag{5}$$

$$u_r^i|_{r=r_1} = u_r^{i+1}|_{r=r_1}\ (i = 0, 1, \cdots, m-1), \tag{6}$$

$$\sigma_r^m|_{r=r_m} = -P, \tag{7}$$

$$\sum_{i=0}^{m} \sigma_z^i A_i = -PA_m, \tag{8}$$

$$\epsilon_z^o = \epsilon_z^1 = \cdots = \epsilon_z^m \tag{9}$$

where $u_r^i (= \int \epsilon_r^i\, dr)$ is the radial displacement in the ith layer, and r_i and A_i are the radius and the cross section area of the ith layer, respectively. Equations (5) and (6) describe the radial stress and displacement continuity across the boundaries of the layers. Equations (7) and (8) assume that the applied pressure is hydrostatic. Equation (9) is the plane strain approximation which ignores end effects. For long thin cylinders such as fibers it introduces an error of less than 1 percent [7].

Using the boundary conditions described by (5)-(9), the constants U_o^i, U_1^i, and W_o^i are determined and ϵ_r^o and ϵ_z^o are calculated from (4). Then from (1) the sensitivity $\Delta\phi/\Delta\phi P$ can be found.

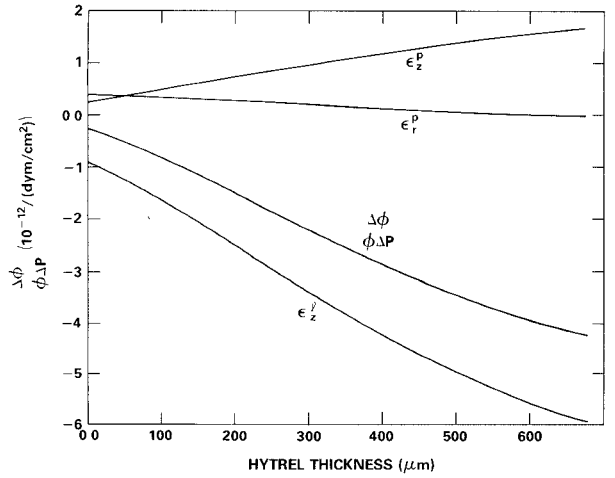

Fig. 4. Pressure sensitivity $\Delta\phi/\phi\Delta P$ of the ITT fiber as a function of Hytrel thickness. ϵ_z^l shows the phase change due to the length change; ϵ_r^P and ϵ_z^P show the refractive index modulation term (after [13]).

Fig. 4 shows the pressure sensitivity of a typical commercially available (ITT) single-mode fiber as a function of the plastic coating (trade name Hytrel) thickness. This thickness may vary from fiber to fiber. The fiber is nominally composed of a fused silica core with traces of GeO_2, a cladding of 5 percent B_2O_3 + 95 percent SiO_2, and a fused silica substrate in a *w*-shaped index profile. The fiber jacket consists of a silicone and a Hytrel layer. The acoustic response of this fiber has been studied both experimentally and analytically in some detail [4], [8]. Table I lists all the parameters used to calculate the sensitivity $\Delta\phi/\phi\Delta P$ of this fiber. From Fig. 4 it is seen that the largest contribution ϵ_z^l is the part of $\Delta\phi/\phi\Delta P$ due to the fiber length change [first term in (1)]. The ϵ_r^P and ϵ_z^P terms [the last two terms in (1)] are due to the photoelastic effect, and they give smaller contributions of opposite polarity. As the Hytrel thickness increases (Fig. 4), the magnitude of the pressure sensitivity increases rapidly due primarily to the ϵ_z^l change.

Commonly used coating materials for optical fibers include rubbers, thermoset plastics, and UV cured elastomers [12]. The coating which is applied directly to the waveguide is typically a soft material, such as a rubber, introduced for minimizing microbend loss. The outer coating is hard and is introduced for preserving glass strength, protecting the fiber from adverse environments, and for facilitating fiber handling. The soft inner coating plays little role in determining the acoustic sensitivity. Accordingly, optimization of the fiber acoustic response involves selecting proper outer jacket materials.

Fig. 5 shows the calculated fiber pressure sensitivity of such a fiber for various outer jacket moduli as a function of coating thickness. Here the Young's modulus of the coating is varied, but the bulk modulus is fixed at a value of 4×10^{10} dyn/cm^2. As can be seen from this figure, as the coating becomes very thick the fiber sensitivity approaches a limit which is independent of the coating Young's modulus. In the case of a thick coating, hydrostatic pressure results in an isotropic strain in the fiber waveguide whose magnitude depends only upon the coating compressibility (inverse bulk modulus). Thus, for the thick coating case (approximately 5 mm) the pressure sensitivity is governed entirely by the coating bulk modulus, independent of the other elastic moduli.

TABLE I
STANDARD ITT SINGLE-MODE FIBER (WITHOUT OUTER COATING)

	Core	Clad	Substrate	First Coating (Soft)
Composition	SiO_2 + traces of GeO_2 (0.1%)	95% SiO_2 5% B_2O_2	SiO_2	Silicone
Diameter (μm)	4	26	84	250
Young's Modulus (10^{10} dyne/cm)	72	65	72	0.0035
Poisson's Ratio	0.17	0.149	0.17	0.49947
P_{11}	0.126			
P_{12}	0.27			
n	1.458			

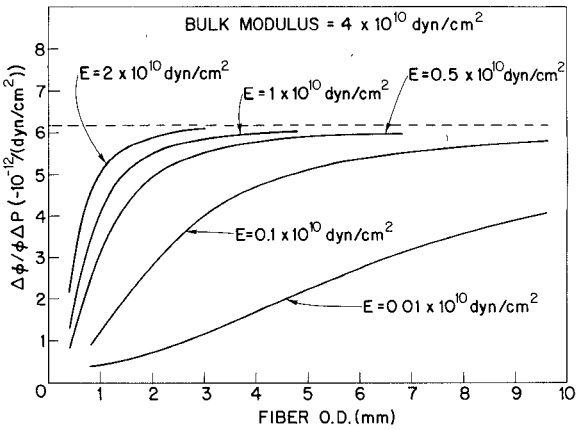

Fig. 5. Calculated pressure sensitivity versus fiber OD for different Young's moduli E and constant bulk modulus (4×10^{10} dyn/cm^2) of outer coating. Fiber parameters are given in Table I.

For fibers with typical coating thicknesses, the sensitivity becomes a more complicated function of the elastic moduli [12]. In this case the waveguide experiences anistropic strains and knowledge of two independent elastic moduli is required to predict the acoustic sensitivity. Fig. 6 shows the pressure sensitivity of a 0.7 mm OD fiber, whose parameters are given in Table I, as a function of bulk modulus for various Young's moduli of the outer coating. As can be seen from this figure, for high Young's moduli the fiber sensitivity is a strong function of the bulk modulus. This dependence becomes weaker as the Young's modulus decreases. This can be understood in the following way. For a composite fiber geometry, the axial stress carried by a particular layer is governed by the product of the cross-sectional area and the Young's modulus of that layer. Thus, for high Young's moduli materials very little

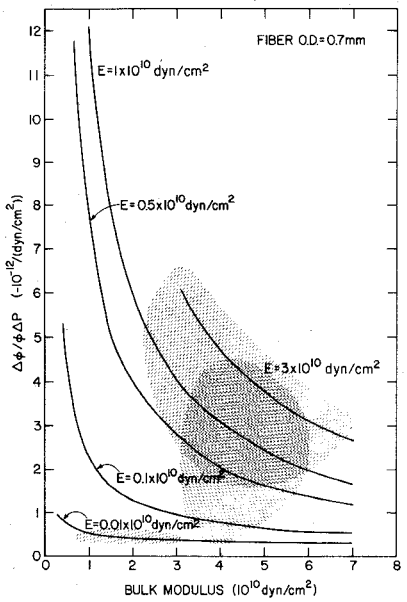

Fig. 6. Calculated pressure sensitivity versus bulk modulus for various Young's moduli of the outer coating of a 0.7 mm OD fiber given in Table I. Shaded areas: plastics (upper), UV curable coatings (middle), rubber (lower).

coating thickness is required to reach the "thick" coating case in which the sensitivity is governed essentially by the bulk modulus of that layer. For low Young's moduli material, however, the degree to which the coating is contributing to the axial strain is diminished and we begin moving toward the limit in which the glass waveguide plays the major role in the sensitivity. Accordingly, for typical coating thicknesses, high acoustic sensitivity requires a high Young's modulus–low bulk modulus material.

Fig. 7 shows the frequency response of the acoustic sensitivity of fibers coated with various elastomers in the frequency range of 10^2-10^4 Hz. As can be seen from this figure, the frequency dependence of the sensitivity of fibers with hard coatings is relatively small. Nylon gives the weakest frequency dependence, and the soft UV cured elastomer the strongest. The maximum sensitivity is obtained with Teflon TFE, while the minimum is achieved with the soft UV coating. With this latter coating, the sensitivity decreases rapidly as the frequency is lowered below 2 kHz. This and similar coatings would not be compatible with broad-band acoustic performance. However, such a coating can be utilized as a low-frequency acoustic filter allowing the detection of high-frequency acoustic signals only.

Acoustic Desensitization

Minimizing the pressure sensitivity of optical fibers may also be important for many of the fiber sensors including the fiber used in the reference arm of the acoustic sensor. It is generally required that the acoustic sensitivity be localized in the sensing fiber and that the reference and lead fibers be insensitive to the acoustic field.

The pressure sensitivity of an optical fiber $\Delta\phi/\phi\Delta P$ is due to the effect of the fiber length change [first term in (1)] and the effect of the refractive index modulation of the core, which is related to the photoelastic effect [second and third terms in

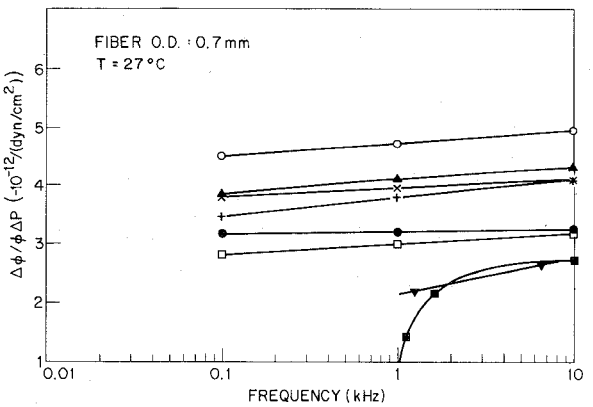

Fig. 7. Frequency dependence of pressure sensitivity of fibers with a 0.7 mm OD coated with various elastometers at 27°C. ○ Teflon TFE I, ▲ Teflon TFE II, × polypropylene 7823, + high density polypropylene, ● nylon, □ Hytrel 7241, ▼ hard UV curable acrylate, and ■ soft UV curable acrylate.

(1)]. These effects are generally of opposite polarity [7]. The acoustic sensitivity of typical optical fibers coated with plastics can be significantly enhanced over that of the bare fiber due to the large contribution of the fiber length change. On the other hand, substantially reduced sensitivity can be achieved if the fiber is coated with high bulk modulus materials. These materials can be glasses [13] or metals [14].

Fig. 8 shows the pressure sensitivity of glass and metal coated fibers as a function of coating thickness. For a nickel jacket of approximately 13 μm, an aluminum jacket of approximately 95 μm, or a calcium aluminate glass thickness of approximately 70 μm, the fiber has zero pressure sensitivity. Nickel requires the smallest jacket thickness. However, the sensitivity versus thickness curve is rather steep requiring a critical tolerance on thickness control.

Acoustic Response at Intermediate Frequencies

Consider again a sensing element with a characteristic dimension D, made from fiber having a diameter d. At intermediate frequencies where the acoustic wavelength Λ is comparable to D, pressure gradients across the sensor become important. In this case the acoustic response characteristics depend upon the geometry of the sensor element. Useful configurations include fibers wound helically on compliant mandrels, fiber loops, a straight fiber embedded in a compliant rod, flat helically wound elements, etc.

As an illustrative example, consider the response of a fiber coil [15]. To determine the dynamic response of the coil it is necessary to derive an expression for the acoustic force, due to the incident sound, on an element of the coil. An expression for the acoustic force is obtained by integrating the pressure of the incoming planewave over the surface of the coil element. Only vibrations in the plane of the coil contribute to the net optical phase shift. The pressure field of the incident sound can be expressed as follows:

$$\begin{aligned} p &= p_o \exp(ik \cdot r), \\ &= p_o \exp[(ik \cdot (R + r)], \\ &= p_c \exp(ik \cdot r) \end{aligned} \tag{10}$$

where R is the position vector of the center of the coil element,

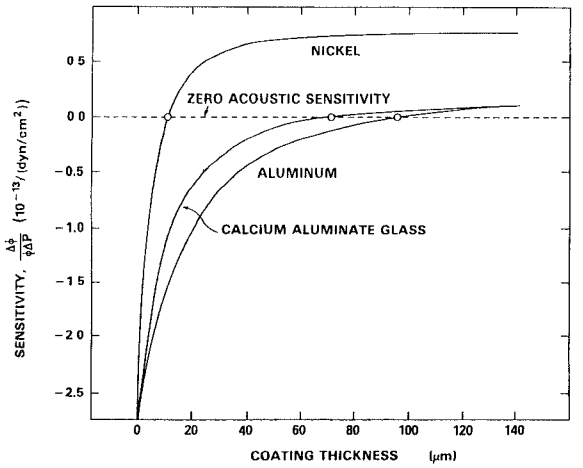

Fig. 8. Pressure sensitivity $\Delta\phi/\phi\Delta P$ of a silica fiber coated with various high modulus materials versus coating thickness.

p_c is the incident pressure at R, and $k = 2\pi/\Lambda$. The in-plane component of the acoustic force on the coil element is

$$F = \left[\left(\int_{\Delta S} pds\right)\cdot n\right] n$$

where ΔS is the area of the element and n is a unit vector parallel to R. When the above integral is evaluated, taking into account the curvature of the element, the final expression for the acoustic force is

$$\Delta F = (-\pi r_c^2 p_c \Delta\alpha) n + i(-\pi r_c^2 p_c kR \sin\theta \sin\Delta\phi)\, n \qquad (11)$$

where $\Delta\alpha$ is the angle subtended by the element at the center of the coil and r_c is the radius of the fiber.

In addition to the acoustic force there are axial elastic stresses on each coil element, determined by the instantaneous axial strain e_z and the acoustic pressure p_c. The total axial force across a cross section of the coil is the sum of contributions from the axial stresses in the fibers and the force due to the hydrostatic pressure in the fluid between the fibers. When the wavelength of the incident sound is long compared to the cross section of the coil, the instantaneous hydrostatic pressure in the fluid can be assumed to be approximately constant across the cross section of the coil, and equal to the acoustic pressure p_c. Then the contribution T_w of the fluid pressure to the axial tension is $T_w = -(1-f)\pi r_c^2 p_c$, where $(1-f)$ is the fraction of the coil cross section occupied by the fluid. The total tension in the fibers is $T_f = f\pi r_c^2 \hat{S}_{zz}$, where $\hat{S}_{zz}$ is the average axial stress in the fiber. $\hat{S}_{zz}$ can be expressed in terms of the axial strain e_z and the instantaneous pressure p on the fiber, where p is taken to be equal to the acoustic pressure p_c. The final expression for the instantaneous tensile force T on a cross section of the coil is

$$T = f\pi r_c^2 (\hat{E} e_z - 2\hat{\sigma} p_c) - (1-f)\pi r_c^2 p_c \qquad (12)$$

where $\hat{E}$ and $\hat{\sigma}$ are the effective fiber's Young's modulus and Poisson ratio.

The incident sound wave will excite various modes of vibration of the coil. When the wavelength of the sound is long $\Lambda \gg r_c$, the vibrations of the coil will be similar to the modes of vibration of a thin circular ring. Flexural vibrations will not give a measurable optical phase shift and the dominant contribution is from the breathing mode. The driving force ΔF_o for this mode is is obtained by integrating around the coil the force ΔF and the part of $-T\Delta\alpha$ which is directly determined by the acoustic pressure p_c.

$$F_o = -\pi r_c^2 \int_0^{2\pi} P_c\, d\alpha - i(\pi r_c^2 kR \sin\theta)\int_0^{2\pi} p_c \sin\alpha\, d\alpha$$

$$+ \pi r_c^2 (2\hat{\sigma} f + 1 - f)\int_0^{2\pi} p_c\, d\alpha.$$

Substituting the expression for p_o and evaluating the integrals gives

$$F_o = -2\pi A p_o [f(1-2\hat{\sigma}) J_o(\eta) - \eta J_1(\eta)] \qquad (13)$$

where A is the cross-section area of the coil, p_o is the pressure amplitude of the incident sound, $J_o(\eta)$ and $J_1(\eta)$ are Bessel functions, and $\eta = kR\sin\theta$. The $J_1(\eta)$ term follows from the pressure-gradient, while the $J_o(\eta)$ term originates from the surface pressure term and the $T\Delta\alpha$ force.

The equation of motion can be expressed as a balance between the driving force F_o and the elastic force, the inertial term, and the reaction force of acoustic radiation from the vibrating coil. For the breathing mode, the radial displacement u and the axial strain are

$$u = u_o e^{-\omega t},\ e_z = u_o e^{-i\omega t}/R. \qquad (14)$$

The elastic force on this element is $-fAEe_z\Delta\alpha$. Damping forces can be formally included by making the effective elastic modulus complex $\hat{E} = \hat{E}' + i\hat{E}''$. The $\hat{E}''$ includes the effects of internal friction in the fibers and viscous damping in the water between the fibers. The inertial term for a coil element $\Delta\alpha$ is $\rho_c AR\Delta\phi\ddot{u}$, where $\ddot{u}$ is the acceleration and ρ_c is the effective density, which is an average between the density of the fibers and the density of the fluid between them.

The vibrating coil will radiate sound and this acoustic radiation will exert a reaction force on the coil element which is approximately given by

$$F_r = A\rho_\omega^2 u_o e^{-i\omega t} R\Delta\alpha \qquad (15)$$

where ρ_ω is the density of water. The equation of motion for an element of $\Delta\alpha$ coil can now be expressed as

$$-\omega^2 u_o \rho_c AR\Delta\alpha = F_o\Delta\alpha/2\pi$$

$$- fA\hat{E}u_o\Delta\alpha/R + \omega^2 u_o \rho_\omega AR\Delta\alpha$$

where the $e^{-i\omega t}$ factor is omitted. Rearranging terms yields the following solution for the amplitude of vibration:

$$u_o = \frac{[f(1-2\hat{\sigma})J_o(\eta) - \eta J_1(\eta)]\, P_o}{[\omega^2(\rho_c + \rho_w)R - f\hat{E}'/R] - if\hat{E}''/R}. \qquad (16)$$

The above expression for u_o can be substituted into (14) to obtain the axial strain. The radial strain can be written in terms of the axial strain and applied pressure p as

$$e_r = qe_z + \beta p \qquad (17)$$

where the coefficients q and β can be determined by applica-

tion of (2)-(9). Finally, the normalized optical phase shift is determined from (1)

$$\Delta\phi/k_o L p_o = \text{Re} + \text{Im} \tag{18}$$

where

$$\text{Re} = \{D(|u_o|/R)\cos u_p - n^2(p_{11} - p_{44})\beta J_o(\eta)\}\, n,$$

$$\text{Im} = \{D(|u_o|/R)\sin u_p\}\, n$$

with

$$D = n^2(p_{11} - p_{44})\, q + 1/2\, n^2(p_{11} - 2p_{44}) - 1$$

and $|u_o|$, u_p are the magnitude and phase, respectively, of the vibration amplitude u_o.

In Figs. 9 and 10 are shown the measured acoustic response of a loop of Hytrel coated fiber compared to theory as calculated from (18). The effect of the fiber loop resonance is apparent in Fig. 9.

The directional response shown in Fig. 10 clearly indicates the effect due to the addition of pressure gradient forces.

High Frequency Ultrasonic Response

Consider an isotropic optical fiber of radius a and infinite length aligned along the z axis. An acoustic wave is incident along the x direction. The strains associated with the acoustic wave change the phase of light propagating through the fiber. At very low acoustic frequencies these strains are uniform across the optical fiber cross section. At higher frequencies, however, the strains are no longer uniform and one must take into account the polarization state of the optical beam. In this case the acoustic wave causes the optical fiber to act as a linear retarder. The electric field components exiting a fiber can be described by the Jones matrix [16].

$$\begin{bmatrix} E_X \\ E_Y \end{bmatrix} = \begin{bmatrix} \cos\alpha(r,\theta) & -\sin\alpha(r,\theta) \\ \sin\alpha(r,\theta) & \cos\alpha(r,\theta) \end{bmatrix} \begin{bmatrix} e^{i\Delta\beta_1(r,\theta)} & 0 \\ 0 & e^{-i\Delta\beta_2(r,\theta)} \end{bmatrix} \cdot \begin{bmatrix} \cos\alpha(r,\theta) & \sin\alpha(r,\theta) \\ -\sin\alpha(r,\theta) & \cos\alpha(r,\theta) \end{bmatrix} \begin{bmatrix} E_{Xo} \\ E_{Yo} \end{bmatrix}. \tag{19}$$

Here the $\Delta\beta_n(r,\theta)$ are the induced phase shifts along each of the acoustically induced principal strain axes, α is the angle between the x axis and the principal strain axes, r and θ are polar coordinates locating the point of interest in the fiber, and E_{xo} and E_{yo} are the input electric fields.

The phase shifts $\Delta\beta_n$ and the induced birefringence $\Delta\beta$ each per unit length are related to the principal strains e_1 and e_2 in the following manner [10]:

$$\Delta\beta_1 = k_o n^3(P_{11}e_1 + P_{12}e_2)/2 \tag{20a}$$

$$\Delta\beta_2 = k_o n^3(P_{12}e_1 + P_{11}e_2)/2 \tag{20b}$$

$$\Delta\beta = (\Delta\beta_1 - \Delta\beta_2) = -k_o n^3 P_{44}(e_1 - e_2). \tag{20c}$$

Here the P_{ij} are the Pockels coefficients, k_o is the optical wave number in vacuum, and n is the refractive index. In general, the principal strains as well as the principal axis angle will vary with position across the fiber cross section. Usually, the acoustically induced strains are sufficiently small so as to act only as a perturbation to the fiber waveguide. This condition can be stated as

$$\Delta\beta_1, \Delta\beta_2 . \ll k\Delta n \tag{21}$$

where Δn is the refractive index difference between the fiber core and cladding.

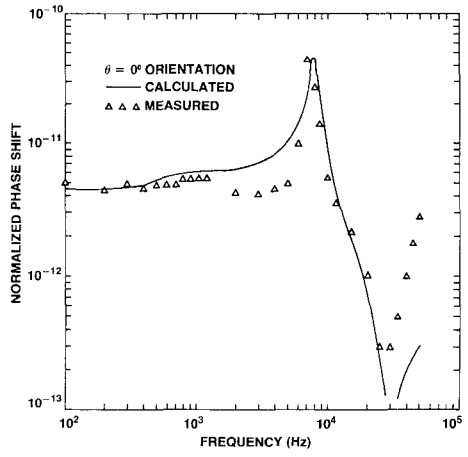

Fig. 9. Frequency response of a 2.5 cm diameter fiber optic coil at θ = 0° orientation. The measured and calculated optical phase shifts (per unit length 1 cm and unit incident sound pressure of 1 dyn/cm^2) are plotted for the frequency range of 100 Hz to 50 kHz (after [15]).

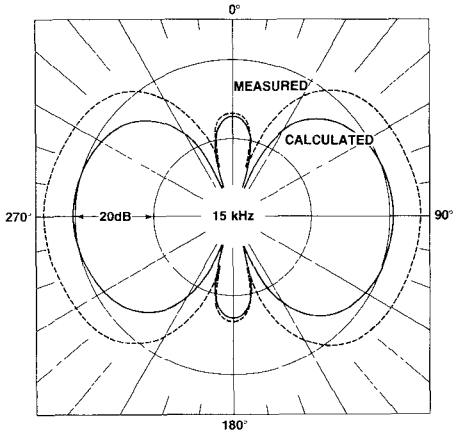

Fig. 10. Beam pattern of the fiber optic coil hydrophone at 15 kHz (after [15]).

The ultrasonically induced principal strains and subsequently the ultrasonically induced phase shifts and birefringence can be calculated by solving the displacement wave equation [17], [18]

$$\bar{u} = -\bar{\nabla}\Phi + \bar{\nabla}x\psi \tag{22}$$

where $\bar{u}$ is the displacement vector, Φ the scalar, and $\bar{\psi}$ the vector potential. For ultrasonic waves of normal incidence the induced principal strains are

$$\epsilon_1 = \frac{\epsilon_{rr} + \epsilon_{\theta\theta}}{2} + \frac{1}{2}[(\epsilon_{rr} - \epsilon_{\theta\theta})^2 + 4\epsilon_{r\theta}^2]^{1/2} \tag{23}$$

$$\epsilon_2 = \frac{\epsilon_{rr} + \epsilon_{\theta\theta}}{2} - \frac{1}{2}[\epsilon_{rr} - \epsilon_{\theta\theta} + 4\epsilon_{r\theta}^2]^{1/2} \tag{24}$$

where ϵ_{rr}, $\epsilon_{\theta\theta}$, and $\epsilon_{r\theta}$ are strains in cylindrical coordinates. The induced principal strains can be calculated from (22)-

(24) by expanding Φ and ψ in terms of cylindrical basis functions and applying four boundary conditions which hold at the surface of the fiber. The displacement and normal stress must be continuous and the tangential stress must be zero at the boundary.

The results of such a calculation for a single-mode fiber are shown in Fig. 11 as a function of ka for an acoustic pressure of 10^4 pa. At low frequencies (ka approximately 0) the acoustically induced phase shift is independent of polarization direction. In this limit the value obtained here is exactly that calculated by a constrained radial model for which the optical fiber experiences a uniform radial pressure, but is constrained not to expand in the axial direction.

The magnitude of the phase shift for the perpendicular polarization increases until the first radial resonance (ka approximately 6) is reached. In contrast, the phase shift for the parallel polarization decreases rapidly as one first begins to increase ka, becoming zero for ka approximately 1.5. At this point, $e_2/e_1 = -P_{11}/P_{12}$. Since $e_2/e_1 < 1$ and $P_{12} > P_{11}$ for silica glass this condition is not obtained for the perpendicular polarization.

The acoustically induced birefringence $(\Delta\beta_1 - \Delta\beta_2)$ is shown in Fig. 12. This induced birefrigence is small at low ka (less than one part in 10^{-4} below ka values of 0.1). However, as seen in Fig. 12, this effect rises rapidly as ka increases, and can itself be used as a acoustooptic transduction mechanism at megahertz frequencies. A sensor based on acoustically induced birefringence can be fabricated with a single piece of fiber in which the two eigenmodes are excited equally at the beginning of the region of interaction between optical beam in the fiber and the acoustic wave. This is accomplished by aligning the input linear polarizer and quarter wave plate such that circularly polarized light arrives at this point. When the output optical beam is properly analyzed in a selected plane of the polariscope, acoustically induced amplitude modulation can be detected with a modulation index $\Delta\beta$.

Sensor Packaging

Since the first reports of laboratory fiber interferometric acoustic sensors [1], [2], considerable progress has been made in the packaging of such devices. A photograph of the original laboratory device is shown in Fig. 13. These early experimental arrangements [4] employed large HeNe gas lasers and bulk optical components for beam splitters. Besides being only laboratory based sensors, the noise levels of these bulk interferometers were high due to laser-to-fiber coupling noise and to the large ambient acoustic noise of the air paths between optical components.

A considerable improvement in S/N can be realized by employing an all-fiber interferometer as shown on the right in Fig. 13. Here the bulk optic beam splitters have been replaced by evanescent fiber bottler couplers [19]. Noise levels for these all-fiber interferometers are considerably reduced and very low acoustic signals have been detected [20] (approximately 10^{-3} dyn/cm^2 = 100 pa = 10^{-9} atm) down to frequencies as low as a few hundred hertz.

One of the first attempts at packaging a fiber optic acoustic sensor for field use is shown in Fig. 14. This hydrophone em-

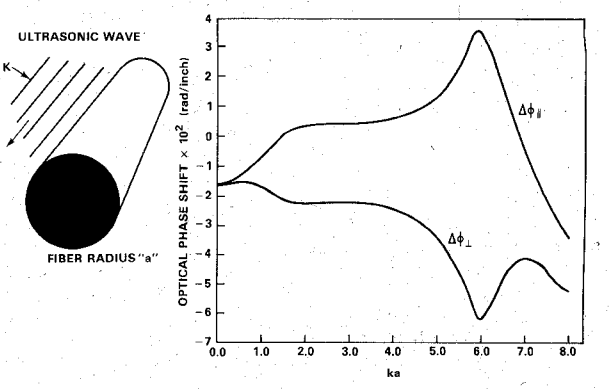

Fig. 11. Ultrasonically induced phase shift per unit length (2.54 cm) and pressure (10^4pa) for polarization parallel and perpendicular to the incident ultrasonic wave. The single-mode fiber radius is a (40 μm) and k is the ultrasonic wave number.

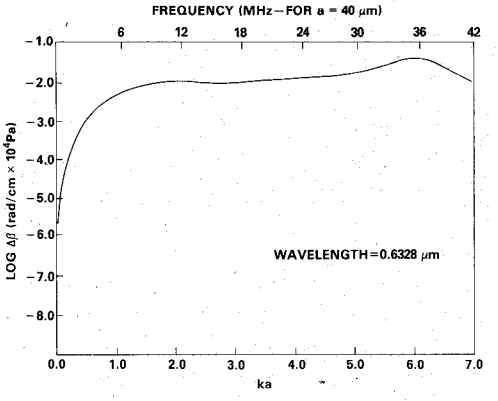

Fig. 12. Ultrasonically induced birefringence $\Delta\beta$ per unit length (1 cm) and pressure (10^4pa) versus ka. The single-mode fiber radius is a (40 μm) and k is the ultrasonic wave number.

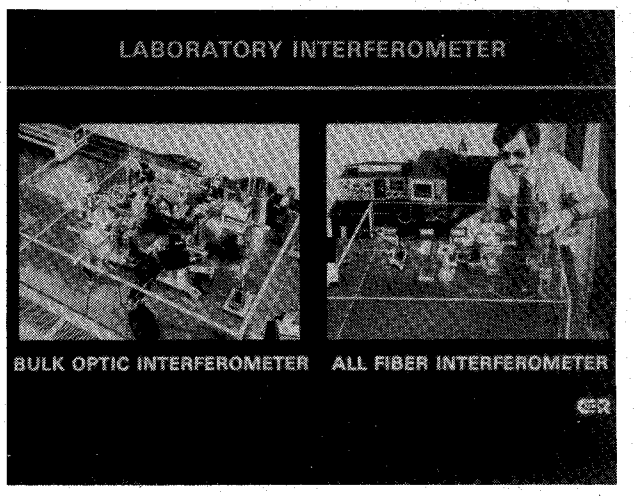

Fig. 13. Laboratory interferometric acoustic sensors. Left: Bulk optic interferometer. Right: All fiber interferometer employing evanescent fiber to fiber "bottle" couplers.

ployed a phase stabilized demodulation scheme [3] to maintain the sensing and reference fiber signals in quadrature. This fiber acoustic sensor was completely self-contained and included the sensing and compensator coils, a stable low noise, single-mode diode laser, two silicon photodetectors (the pair discriminates against optical intensity noise), and the demodulator electronics (not shown) which was placed in the space be-

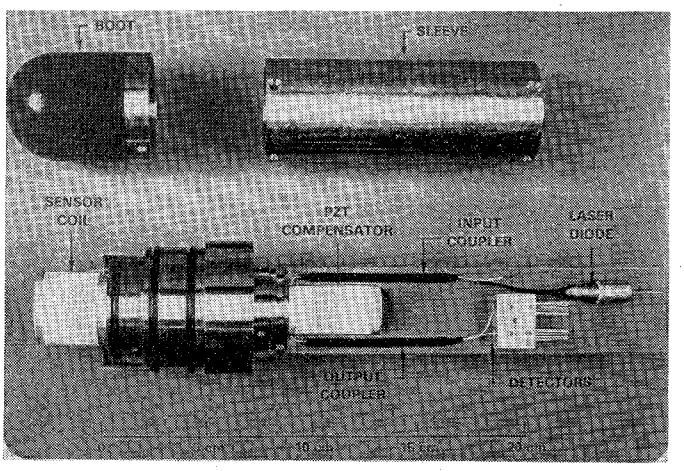

Fig. 14. Hydrophone demonstrating ability to package interferometric, all fiber acoustic sensor for use in stressing environments.

tween the compensator and detector pair. The massive metal flange behind the sensor coil has been included to permit coupling of the sensor to a high pressure acoustic testing facility and normally would not exist in most hydrophone designs. This hydrophone successfully demonstrated the feasibility of taking laboratory acoustic sensors into actual field deployment.

III. Fiber Optic Magnetic Sensors

Introduction

This section of the paper will consider recent developments in the area of fiber optic sensors designed for the measurement of small magnetic fields. Two basic approaches exist for the measurement of magnetic fields with conventional single-mode silica and doped silica optical fibers, namely, the Faraday rotation approach and the magnetostrictive jacket or stretcher approach. In the former approach an external magnetic field H is applied longitudinally to a fiber to produce a rotation in the direction of linear polarization. Smith [21] demonstrated that this technique can be utilized to measure high electric currents in the 0-1000 A range without the dangers of short-circuiting cables. However, the Verdet constant of most doped silica fibers is sufficiently small ($\approx 1.5 \times 10^{-2}$ min $\cdot$ A^{-1}) that only large currents and magnetic fields can be detected by the Faraday approach. Yariv and Winsor [22] considered the doping of paramagnetic ions into optical fibers to raise the Verdet constants to much higher levels than those observed in the base glass itself. Rare earth ions can be incorporated into silica to greatly enhance the Faraday effect, but constraints on solubility of the ions in the glass and the optical absorption introduced by the ions limit the enhancement which can be achieved in practice. However, theoretical sensitivities of approximately 10^{-4} G/m of fiber optic path length seem possible in rare earth doped optical fibers if they can be fabricated with acceptable polarization preserving properties. The Faraday approach requires both special materials and sophisticated fiber drawing techniques to provide highly sensitive detection of magnetic fields.

The alternate approach employing magnetostrictive materials not only is more straightforward, but also is potentially capable of much greater sensitivity in magnetic field measurement. Therefore, the balance of this section on fiber optic magnetic field sensors will concentrate on this technique. The principles of device operation will be given along with descriptions of basic sensor configurations, typical performance data on some recent devices, and a discussion of future possibilities and applications. Parameters of interest in characterizing magnetic field sensors include minimum detectable H field, linearity versus applied H field, directivity, frequency response, and noise constraints on performance. Each of these will also be considered for some specific devices.

Basic Approach and Principles of Magnetic Sensors

The fundamental principle of sensor operation is associated with the measurement of the longitudinal strain produced in an optical fiber bonded to or jacketed by a magnetostrictive material. Magnetostriction is described as a change in dimension of a ferromagnetic material when it is placed along the axis of an applied magnetic field [23]. For purposes of this treatment, only the longitudinal change is important but volume and transverse changes also occur. Yariv and Winsor [22] first proposed the use of nickel magnetostrictive jackets on single-mode fibers incorporated into a fiber interferometer such as those discussed earlier in this paper. The approach is totally analogous to the acoustic sensor except that a metallic jacket rather than a polymer jacket is utilized to stretch the waveguide. The measurement of small changes in optical path length is accomplished with a conventional Mach-Zehnder all-fiber interferometer such as described earlier. Dandridge *et al.* [24] reported the first experimental results on fiber magnetic field sensors and found sensitivities as high as 8×10^{-8} G/m of fiber in bulk nickel-clad fiber devices operating at 1-10 kHz. Somewhat lower sensitivities were found experimentally in thin nickel film coated fibers. Jarzynski *et al.* [25] calculated the respective magnetic responses anticipated for various metallic alloys and calculated the reduced elongation of thin metallic coatings versus thickness which arises from the mechanical loading by the rigid glass fiber. This loading effect requires metallic coatings of approximately 10 μm for nickel and nickel alloys on 100 μm diameter silica fibers to obtain magnetostrictions approaching that of bulk material. The use of bulk stretchers such as the nickel toroid recently reported by Cole *et al.* [26] provides an alternate structure which does not suffer from fiber mechanical loading. Magnetostrictive materials have been incorporated into fiber polarization sensors by Rashleigh [27] to produce still an alternate approach to high sensitivity magnetic field measurements.

The key problem to be solved at the present time is the identification of high magnetostriction materials and the incorporation of such materials into a fiber sensor by appropriate bonding or coating. Magnetostrictive materials of interest fall into the categories of selected crystalline metals and metallic glasses. Magnetostrictive metals include Fe, Co, and Ni and various alloys and compounds of the three elements. The magnetostrictive coefficient $\bar{\lambda}_s$ is given as a fractional dimensional change Δl divided by the total length l. Some typical magnetostrictive constants for cubic crystals are provided in Table II. For a polycrystalline jacket fabricated from these materials, $\bar{\lambda}_s$ is given by the following expression:

$$\bar{\lambda}_s = \frac{2\lambda_{100} + 3\lambda_{111}}{5}. \tag{25}$$

Using (25) the $\bar{\lambda}_s$ for nickel is calculated to be 32.8×10^{-6}.

TABLE II
MAGNETOSTRICTIVE CONSTANTS OF SOME CUBIC CRYSTALS*

Material	λ_{100} (x 10^{-6})	λ_{111}(x 10^{-6})
-Fe	20	-20
40% Ni-Fe	-7	30
60% Ni-Fe	27	22
73% Ni-Fe (annealed)	14	7
73% Ni-Fe (quenched)	15	14
80% Ni-Fe	9	0
Ni	-46	-24
3% Si-Fe	27	-5
7% Si-Fe	-5	3
$Ni_{0.8}Fe_{2.2}O_4$	-36	-4
$Co_{0.8}Fe_{2.2}O_4$	-590	120

* Data from Ref. 3

For iron-nickel alloys, longitudinal magnetostriction can either be positive (expanding dimension) or negative (contracting dimensions) with 30 percent nickel yielding approximately zero dimensional change, 45 percent nickel exhibiting the highest positive magnetostriction, and pure nickel showing the largest contraction. For reasons of fabrication simplicity, corrosion resistance, and availability, pure nickel is a convenient material to use in fiber magnetostriction devices. However, its properties are greatly influenced by the presence of impurities, processing, and final heat treatment. Iron-cobalt alloys also offer large values of magnetostriction with 60–70 percent Co providing the maximum response for most applied fields.

For a magnetostrictive fiber sensor, the term of interest is the first derivative of the function which relates the change in the magnetostriction to the applied time-varying magnetic field H_1 and the applied constant magnetic field H_0. The static magnetostriction is given by

$$\bar{\lambda}_S = \frac{K}{2}\frac{H_1}{\sqrt{H_o}}$$

where k is a constant. By analysis of the $\Delta l/l$ versus magnetic field strength curves for various metals and metal alloys, it is possible to identify regions of steep slopes in which a small change ΔH can produce a maximum dimensional change $\Delta l/l$. The variation of magnetostrictive response with specified applied external magnetic fields requires a constant magnetic bias field H_o to be applied to place the device in the region of maximum sensitivity. In practice, the use of dynamic magnetic fields produces behavior in which hysteresis subloops are traced and loss mechanisms such as eddy currents can be encountered. Thus, it is important to characterize the frequency response of the devices to assess deviations from the behavior predicted by static magnetostriction measurements.

Experimental Setup for Magnetic Measurements

The changes in optical pathlength generated by contraction or expansion of magnetostrictive materials bonded to optical fibers were detected by an all fiber interferometer capable of detecting phase shifts as small as 10^{-6} rad. The optical pathlength of the signal arm was modulated at a frequency ω_m by placing the magnetostrictive sensor in an oscillating magnetic field H_1. A steady-state bias field H_o has also applied in order to place the sensor in the maximum sensitivity range of operation. Detection was accomplished using phase tracking techniques which maintain the interferometer at maximum sensitivity by nulling low frequency fluctuations such as those which arise from temperature fluctuations and air currents [28].

The magnetic sensors themselves typically are configured in one of three basic configurations: 1) the bulk magnetostrictive cylinder or mandrel with fiber bonded to its circumference, 2) a metal coating or jacket applied uniformly to the surface of the fiber, and 3) the cylindrical fiber bonded to a metallic strip, as illustrated in Fig. 15.

Nickel fiber coatings have been produced both by vacuum evaporation and electroplating with the latter approach more desirable for the production of the thick 10 μm coatings required for acceptable sensitivity. However, the coated sensors have all been prepared substantially after fiber fabrication and an in-line coating process has yet to be developed. In order to eliminate residual strains in the films produced during the deposition process, it is essential to anneal the sensor prior to operation. The most successful approach to date in our laboratory has utilized metallic glass strips and tapes of high magnetostriction to which fibers are bonded in either a straight-line or cylindrical configuration. Commercially available metallic glasses produced by the Allied Chemical Corporation such as alloys 2605 SC and 2605 CO based on the FeBSi system have been notably successful in producing high sensitivity fiber magnetic sensors. The amorphous alloys are produced by rapidly quenching a molten stream of material on a cold spinning flywheel to produce a tape of approximately 3 cm width and 500 μm thickness. The single-mode fiber is bonded to the metallic glass strip by a thin layer of epoxy.

Magnetic fields are generated in the laboratory by various configurations including Helmholtz coils, magnetic circuits, solenoids, and current carrying cylinders about which the fiber is wrapped. Separate sets of coils were used to generate the time varying and constant bias fields. Fig. 16(a) and (b) illustrate two of the basic magnetic sensor designs for the metallic glass sensors. In the arrangement shown in Fig. 16(a), a direct current is passed through the inner set of Helmholtz coils to produce a large bias field of a few gauss to tenths of gauss. The field to be detected is generated by a small alternating current passed through the outer coils. An alternate bias configuration is shown in Fig. 16(b) in which a metallic glass strip is placed around a copper cylinder through which both direct and alternating currents are passed. The optical fiber is wrapped around the metallic glass a number of turns and bonded by epoxy as with the stripguide. The direction of the fiber relative to the axis of the metallic glass strip is identical in both configurations shown in Fig. 16. The magnetostrictive

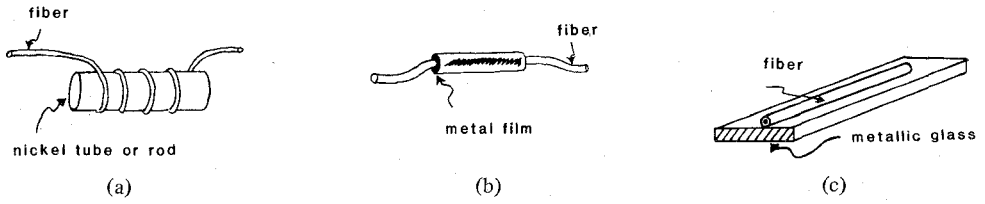

Fig. 15. Basic configurations of magnetic fiber sensors: (a) Mandrel sensor, (b) coated sensor, and (c) stripline sensor.

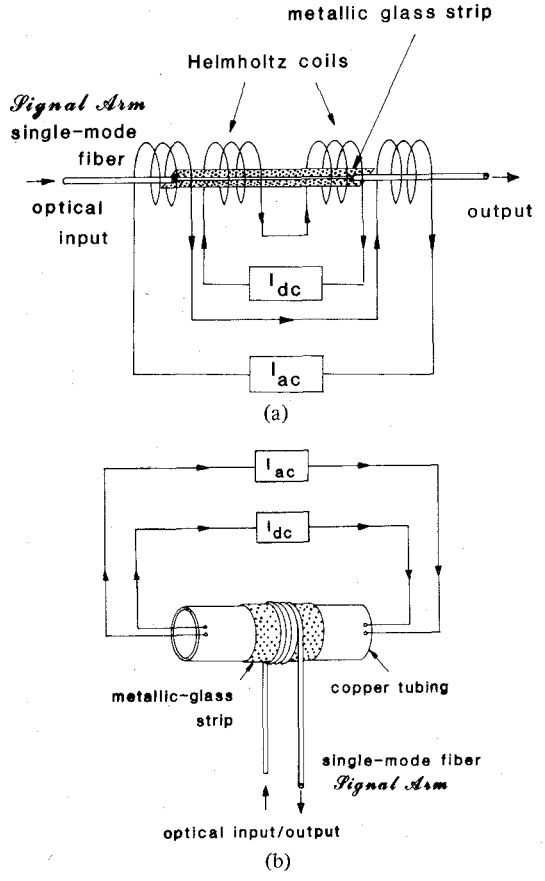

Fig. 16. (a) Schematic diagram of metallic glass stripline sensor using two pairs of Helmholtz coils to generate time varying and constant bias magnetic fields. (b) Schematic of cylindrical metallic glass sensor in which alternating and direct current passed through a copper cylinder is utilized to generate magnetic fields.

response of metallic glasses in longitudinal and transverse directions will vary considerably. The metallic glass response can also be improved by field anneals of the tapes prior to sensor fabrication.

Magnetic Sensor Response

The initial magnetic fiber sensors investigated by Dandridge *et al.* [24] utilized nickel claddings of both bulk and thin-film form. Interferometer output versus applied magnetic field were demonstrated to remain linear over six orders of magnitude and minimum detectable magnetic fields of about 10^{-6} G/m of optical path length were typical in the frequency range from 100–5 kHz. Sharp frequency-dependent oscillations in sensitivity were observed above 5 kHz and appeared to be associated with mechanical resonances in the sensors.

More recent work [29] in our laboratory has focused on the investigation of metallic glass based sensors since these materials offer both high magnetostrictive constants as well as the prospect of zero bias field operation. Fig. 17 shows the measured interferometer response of a strip metallic glass sensor of 7 cm length measured in the experimental configuration of Fig. 16(a). Note that the dc bias field is zero from this particular set of data on a 2605 CO material. Linearity of the sensor response is again excellent. Similar data have been obtained on a variety of other metallic glass stripline sensors. The region of magnetic sensitivity is controlled by the length of the sensor and the dynamic range of the instrumentation. These data were taken at a frequency of 1 kHz for the time-varying field and at room temperature. Measurements were conducted in a shielded chamber to minimize air current perturbations, but at ambient atmospheric pressure.

Another parameter of interest for device assessment is the frequency response of the sensor as a function of applied magnetic field H_1. The magnetostrictive constant itself can exhibit some variation with frequency in magnetic materials, but appears to remain relatively stable in the region from 100–1000 Hz investigated in our experiments. The high frequency limitation of magnetic sensor response appears to be associated with eddy current losses induced in the metals. The low frequency cutoff is controlled by the nature of the detection schemes used on the interferometer, optical noise in the laser, and environmental noise such as that produced by random thermal fluctuations and pressure perturbations. The data presented in Fig. 18 were primarily for the assessment of peak magnetostrictive performance of respective materials. The circuitry was designed to provide a basis for such comparisons at frequencies centered near 1 kHz.

The effects of applied magnetic bias field are dramatically illustrated in Fig. 19 which shows the measured interferometer output of a 2605 SC metallic glass sensor for a fixed ac 1 kHz signal excitation as a function of the bias field. The response of all materials measured to date including nickel, metal alloys, and metallic glass were observed to change dramatically following heat treatments to anneal residual strains. The sharpness of the magnetostriction versus bias field curve appears particularly sensitive to such heat treatments as well as to the presence of impurities in the materials. Experiments are continuing with bulk, thin film, and stripline sensors to optimize annealing conditions as evidenced by peak magnetostriction and bias field dependence characteristic curves.

The key question to be answered from a practical standpoint is the relative sensitivity of fiber magnetic sensors for the measurement of small magnetic fields. If it is assumed that an optical path length change of 10^{-6} rad can be detected in a standard fiber interferometer, the experimental data acquired in

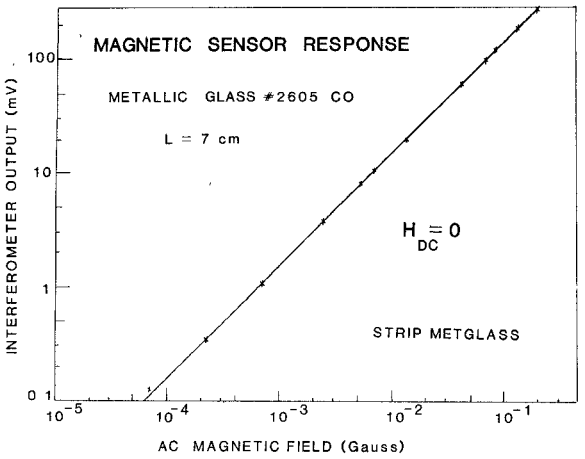

Fig. 17. Typical response of a stripline metallic glass sensor configured in a dual arm fiber interferometer versus applied magnetic field. Bias field = 0, T = 23°C (after [29]).

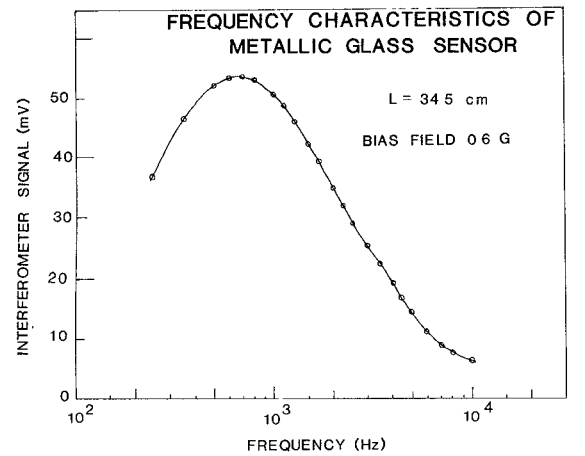

Fig. 18. Frequency response of a metallic glass sensor in the cylindrical current mode configuration. The metallic glass was type 2605 SC. T = 23°C.

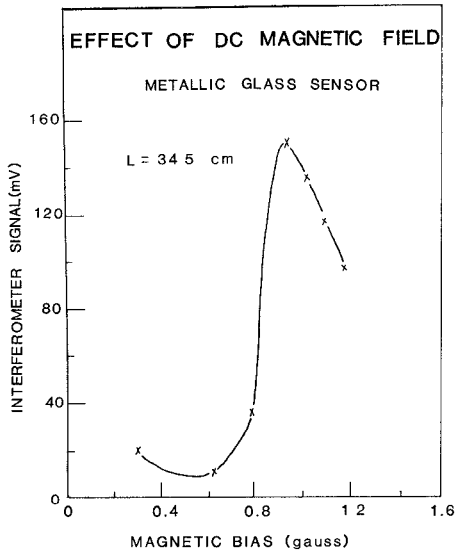

Fig. 19. Effect of constant bias field on the response of a metallic glass sensor (2605 SC) in the cylindrical configuration. The data were taken at 1 kHz for constant time varying signal H_I of 0.01 G. T = 23°C.

the laboratory can be utilized to extrapolate to a minimum detectable field per unit length of optical fiber used to make the measurement. This also assumes that the magnetostrictive response versus applied magnetic field remains linear over the region of interest. Table III provides a summary of the relative sensitivities of various types of sensors measured in our laboratory under a variety of bias field conditions. The data are included for bulk nickel jacketed fibers, electroplated nickel films on fibers, vacuum evaporated nickel films on fibers, metallic glass strips bonded to fibers, and evaporated metallic glass films on fibers. Measurements are also provided on metallic glass strips measured perpendicular to the as-spun axis which corresponds to the hard direction of magnetization. For all of the cases reported here, the constant bias field and the time-varying alternating field were applied in the same direction. The sensitivities for the metallic glasses are several orders of magnitude better than those observed for bulk nickel. The metallic glass 2605 SC has exhibited a minimum detectable field of 5.0×10^{-9} G for a 1 m projected sensor length. These data were obtained on the as-received material which has not been subjected to a field anneal to further enhance its properties. Table III also reports for the first time the results on electroplated nickel films deposited directly onto a fiber. Electroplating enables one to produce a sufficiently thick film to minimize mechanical loading by the fiber. The electroplated fibers were annealed at 1000°C in hydrogen prior to measurement. The important result here is that the sensitivity observed initially in bulk nickel clad fibers has been matched and slightly exceeded in the electroplated nickel film type of sensors. This technique offers the prospect of the preparation of long continuous production of metal coated sensors with enhanced sensitivity.

The ultimate sensitivity of the fiber magnetic field sensors may be limited by a variety of instrumental, environmental, and fundamental material constraints. Temperature and pressure fluctuations [30] must be considered and their effects assessed. Compensation and subtraction techniques coupled with unique fiber designs incorporating thermalized glasses and pressure-insensitive coatings may offer some hope of reduced environmental sensitivity. If magnetic sensitivities can be further enhanced by materials processing and field anneals, it may be possible to operate the interferometer at reduced sensitivity, further minimizing the effects of random perturbations. Magnetic noise sources such as Barkhausen noise associated with domain wall motion in the magnetic materials may eventually be a limiting factor at very low applied fields, but its effects or presence have yet to be observed in the measurements on fiber sensors.

Potential Applications of Fiber Magnetic Sensors

The development of a compact, high sensitivity, room temperature magnetic field sensor would represent a significant advance in present day magnetometer technology. The most sensitive devices for measurements of small magnetic fields at present are superconducting quantum interference devices (SQUID's) which are capable of detecting fields as small as 10^{-11}-10^{-12} G in the laboratory, but often are substantially

TABLE III
SENSITIVITIES OF MAGNETIC FIBER OPTIC SENSORS AT 1 kHz

TYPE OF SENSOR	BIAS CONDITION (H_{DC} in Gauss)	MINIMUM DETECTABLE FIELD (Gauss/Meter of Fiber)
Bulk Nickel Jacket	3.0	8.0×10^{-7}
Electroplated Nickel Film ($t = 15$ (μm)	0	6.0×10^{-7}
Evaporated Nickel Film ($t = 1.5$ (μm)	0	1.0×10^{-4}
Metallic Glass Strip (#2605 CO)	0	2.3×10^{-8}
Metallic Glass Cylinder (#2605 SC)	0.94	5.0×10^{-9}
Evaporated Metallic Glass Film ($t = 0.6$ (μm)	0	3.0×10^{-5}
Metallic Glass Strip (#2605 CO-Hard Dir)	28.0	1.0×10^{-7}

less sensitive in the field. SQUID's require cryogenic instrumentation for their operation which severely limits the conditions under which they can be utilized. The fiber optic sensors with 10^{-8}-10^{-9} G/m sensitivities would appear to approach SQUID's in lengths of 100-1000 m at 1 kHz. Even if the fiber magnetometer requires thermal stabilization to increase signal-to-noise in the device, it is more straightforward to stabilize at room temperature than at cryogenic temperatures. Even if the fiber sensors fail to match SQUID performance, there are a large number of magnetic applications which fall into the 10^{-5}-10^{-10} G region not easily attained by many present day magnetometers.

For the detection of a metallic object or magnetic dipole at some distance $\vec{r}$, the measurement of the spatial magnetic field gradient is of interest rather than the absolute magnitude of the field itself. Such a device is referred to as a "gradient field" magnetometer. A dual arm fiber interferometer is an attractive configuration for the design of a gradient magnetometer. By employing metal jacketed fibers in both arms of the interferometer and balancing the device to produce a null response to rotation in earth's field and to time-varying, spatially coherent signals, it should be possible to construct a high sensitivity gradient type device. Balancing of the two arms can be achieved by both length adjustment as well as tuning of the bias field.

Other potential classes of applications of magnetic field sensors include magnetic antennas for detection of electromagnetic signals and the design of a magnetooptic compass to provide magnetic heading. In some cases the fibers will be deployed with other types of fiber sensors which will provide both complementary data as well as information which can be utilized to compensate or correct the magnetic data themselves. Results to date in the area of magnetic fiber sensors show great promise, but much remains to be achieved if they are to eventually be deployed as reliable, stable, high sensitivity magnetic field devices. However, the success of the fiber optic sensor approach in other areas more advanced than the magnetics such as discussed earlier in this paper for the acoustic sensors gives us confidence that our goals will be realized.

IV. FIBER OPTIC GYROS

Introduction

Passive fiber optic ring interferometers have shown promise for use as inertial rotation sensors [31]. The theoretically predicted sensitivities, based upon photon noise [32], are very high, but to date state of the art experimental gyroscopes have not met these theoretical predictions. However, rapid progress has been made recently in fiber optic gyroscope development, and sensitivities approaching the 1 deg/h range have been demonstrated [33]-[35]. Such sensitivities are already sufficient to make the fiber optic gyroscope attractive for several low performance applications. In this section the status of fiber optic gyroscope development is reviewed with particular emphasis placed on the problems and noise sources that limit performance. Several of the more promising gyroscope configurations are discussed with their results, advantages, and limitations.

Principle of Operation

The basic configuration of a fiber optic gyroscope is shown in Fig. 20. The single-mode fiber is arranged in a loop to form a Sagnac interferometer. Rotation of the gyroscope about an axis parallel to the axis of the fiber coil results in a nonreciprocal phase difference $2\phi = 8\pi$ NA $\Omega/\lambda c$ being introduced between the two counterpropagating light beams. Here, NA is the total area enclosed by the fiber coil, λ and c are the free space light wavelength and velocity, respectively, and Ω is the rotation rate. When these two beams are recombined in the fiber directional coupler and mixed in the detector, this phase shift of 2ϕ leads to a rotation-dependent intensity of $I = \frac{1}{2} I_o (1 + \cos 2\phi)$. In this configuration the gyroscope sensitivity $(1/I_o)\ (dI/d(2\phi)) = \frac{1}{2} \sin 2\phi$ is small for small rotations. To maximize the small signal sensitivity, the phase modulator in the fiber loop introduces an "effectively nonreciprocal" $\pi/2$ phase shift between the two counter propagating beams. Now the detector intensity $I = \frac{1}{2} I_o(1 - \sin 2\phi)$ changes linearly for small rotation rates and the gyroscope sensitivity is at its maximum value of 0.5. Various ways of introducing this nonreciprocal $\pi/2$ phase shift will be discussed.

Gyroscope Sensitivity

Theoretical predictions of fiber gyroscope sensitivity have been based on the expectation of shot noise limited performance of the detector [32]. As discussed below, several other noise sources have limited gyroscope performance to date, but in light of recent progress in the development of very low loss fibers, it is informative to review the sensitivity limit as determined by quantum noise. The uncertainty or noise with which optical energy can be measured is proportional to the square root of the average number of photons [36]. A Sagnac phase shift can be detected only if the corresponding intensity change is larger than this quantum noise. That is, when the interferometer is operating at maximum sensitivity, the minimum detectable Sagnac phase shift is $2\phi = \Delta I/I_o = 1/\sqrt{n_{ph}}$, where n_{ph} is the average number of photons. This then allows the

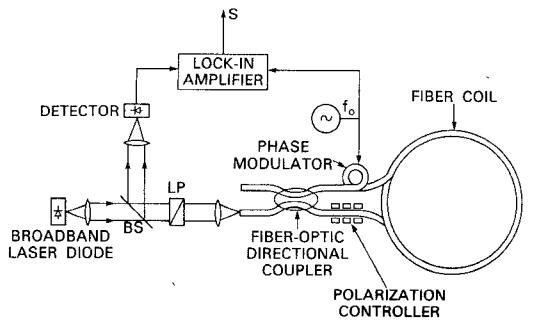

Fig. 20. Schematic configuration of a fiber optic gyroscope.

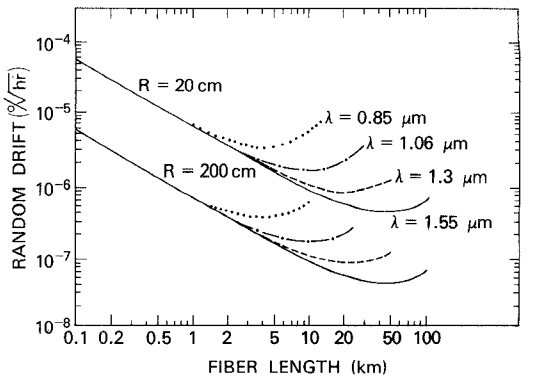

Fig. 21. Theoretical performance limit of fiber optic gyroscopes as a function of fiber length for state of the art fiber attenuations. The input power is 1 mW.

gyroscope random drift θ_{drift} to be written as [37]

$$\theta_{\text{drift}} = \frac{25\lambda c}{\pi LR}(10^{-\alpha L/10})^{-1/2}\left(\frac{P\lambda}{hc}\right)^{-1/2} \text{rad/h}^{-1/2}. \quad (26)$$

Here, L and R are the fiber length and radius of the fiber coil, respectively, α is the attenuation of the fiber in dB/km, h is Planck's constant, and P is the power injected into the fiber coil. Other losses such as coupling loss and insertion loss of the fiber directional coupler have been ignored. In (26) the fiber attenuation has been explicitly taken into account as this allows the optimum fiber length for maximum gyroscope sensitivity to be evaluated as a function of fiber attenuation. The optimum fiber length corresponds to $\alpha L = 8.69$ dB.

The theoretical sensitivity of fiber gyroscopes, as given by (26), has been plotted in Fig. 21 for state of the art fiber attenuations as listed in Table IV. The input power is normalized to 1 mW. It is clear that the theoretical sensitivities of fiber gyroscopes, as limited by quantum noise, are very high, but present experimental gyroscopes have sensitivities substantially lower than these predictions.

TABLE IV
FIBER ATTENUATIONS USED TO EVALUATE THE RANDOM DRIFT OF FIBER GYROSCOPES

λ (μm)	0.85	1.06	1.3	1.55
α (dB/km)	2.0	0.83	0.37	0.18

Fiber Gyroscope Noise Sources

Several noise sources that limit gyroscope sensitivity have been identified recently. The consequence of these and a means of overcoming them will be discussed here. Obviously, as demstrated performance still has not met theoretical predictions, unidentified noise sources still remain.

1) Reciprocal Operation: In order to ensure unambiguous detection of the small nonreciprocal Sagnac phase shift 2ϕ, all other nonreciprocal effects must be excluded. For reciprocal propagation through the fiber ring, the two counterpropagating beams must traverse the same optical path so that they are identically affected by perturbations of their common path. Under this condition their relative phase shift, even after long fiber lengths, remains insensitive to environmental perturbations, allowing a stable evaluation of the Sagnac phase shift. Nonreciprocal effects that can introduce noise and instabilities are the Faraday magnetooptical effect, fiber birefringences, and time-dependent temperature and pressure gradients. Nonreciprocal Faraday-effect phase shifts will be small unless strong magnetic fields are applied axially to the fiber and these phase shifts can be avoided with appropriate shielding.

Fiber birefringences are the major cause of nonreciprocal instabilities [38]-[40]. Single-mode fibers are birefringent and can propagate two modes of orthogonal polarization with slightly different phase velocities. Perturbations couple the two polarization modes and transfer power between them. Because of their different phase velocities, the orthogonal polarization components of each of the counterpropagating beams arrive at the output with phases that depend on the positions of the perturbations along the fiber coil. These phase differences are very sensitive to environmental conditions and introduce instabilities, but the nonreciprocities can be reduced by selecting one particular polarization state at both ends of the optical path [38]. The portions of the counterpropagating beams that have not traversed the common path are rejected. However, by itself this polarization selection is not sufficient to ensure stable reciprocal operation. In measuring very small phase shifts, high stability is required in the optical components that compose the ring interferometer. Instabilities in, for example, the fiber directional coupler manifest themselves as an offset and drift of the zero point of the output signal. Stable, reciprocal operation can be guaranteed only if the interferometer is operated through a common-point, single-mode, single-polarization filter [40]. This means that only light exiting from fiber port 1 in Fig. 20 will have propagated reciprocally through the fiber coil, and at the same time, have a stable zero point. Light exiting through fiber port 2 may have propagated reciprocally through the fiber coil if the appropriate polarization state is selected, but depending on the stability of the fiber coupler it will exhibit varying amounts of zero offset or drift. In order to use this interferometric output, stabilities exceeding those demonstrated by fiber couplers would be required [41].

It is important to realize that the common-point, single-mode, single-polarization filter ensures stable reciprocal operation with regard to *phase*, but the *amplitude* of the output signal can vary substantially. If polarization coupling in the fiber coil causes the output polarization state to be orthogonal to the single-polarization filter, the output signal will fade completely. To prevent this, a polarization controller [42], [43] is usually

placed at one end of the fiber coil, as shown in Fig. 20, to actively control the intensity of the output signal [44]. Passive control of this intensity and the degree of polarization required will be discussed in the following pages.

The third mechanism by which nonreciprocities can be introduced is time-dependent temperature and pressure gradients along the fiber [45]. Nonreciprocity arises because the two counterpropagating beams transverse the same region of fiber at different times, the optical path length of which has changed during the time interval due to changing environmental conditions. For this to occur, the environmental conditions must vary at frequencies corresponding to the transit time through the fiber coil. Analysis shows that stringent control of the environment in which the gyroscope operates may be required for higher sensitivity gyroscope applications [45].

2) Phase Bias: It is a consequence of reciprocal operation of a Sagnac interferometer that the two counterpropagating beams arrive back at the input with equal phases. Hence, they interfere constructively and the amount of intensity radiating from the input port is a maximal, in the absence of nonreciprocal effects such as rotations. As mentioned earlier, this corresponds to the gyroscope having zero sensitivity for very small rotations, when for a high sensitivity device, this is the regime in which maximum sensitivity is required. To convert the sensitivity to its maximum value for small rotations, a nonreciprocal, highly stable $\pi/2$ phase shift must be introduced between the counterpropagating beams. Several approaches have been adopted to introduce this phase bias, with varying amounts of success. The use of a mechanical dither [46] to intentionally introduce a nonreciprocal Sagnac phase shift potentially introduces instabilities in the fiber coil while a static Faraday-effect nonreciprocal phase shift [47] suffers from polarization and drift instabilities.

More promising schemes involve a *reciprocal* phase shift that is made to be "effectively nonreciprocal" by varying the amplitude of the phase shift during the transit time through the fiber coil. On the average, reciprocity in the interferometer is maintained. The conceptually more simple, but technically more difficult scheme, is to pulse a $\pi/2$ phase shift on and off at a repetition rate that corresponds to the transit time through the coil, typically approximately 200 kHz for a 1 km long fiber coil. As rapid switching times are usually required, the phase modulator must be capable of operating at frequencies of at least tens of megahertz. To date, this can only be achieved in integrated optical devices that by themselves introduce many other problems such as inefficient coupling, polarization dependence, extreme temperature dependence, index-matching of the fiber/chip interface to prevent reflections, etc. [48]-[50]. Nevertheless, if high-speed modulation is required, for example, for high data rates, then an integrated optics device appears to be the only choice available presently. Integrated optics have the potential of integrating all the beam splitting and signal processing devices on a single chip, enabling a compact, rugged, high data rate gyroscope.

The other less complex and, to date, more successful scheme involves sinusoidally varying a reciprocal phase shift at much lower frequencies [34], [35], [40]. Lower frequencies allow electromechanical devices such as piezoelectrical materials to be used to stretch the fiber so as to elastooptically introduce the time-varying phase shift. In this way the phase shift can be applied directly to the light in the fiber, removing interfacing and reflection problems [51]. If the phase modulator is positioned at one end of the fiber coil, as shown in Fig. 20, and it introduces a phase modulation at a frequency f_o of $\psi \cos 2\pi f_o t$, then this *reciprocal* phase modulation effectively modulates the *nonreciprocal* Sagnac phase shift and the output intensity becomes [40]

$$I = I_o \cos^2 (\phi - \psi \sin \alpha \sin 2\pi f_o t_o) \tag{27}$$

where $2\alpha = 2\pi f_o T$, T is the transit time through the fiber coil and $t_o = t + T/2$ is a shifted time scale. Expanding (27) into its frequency components gives

$$I = \tfrac{1}{2} I_o [1 + J_o(\eta) \cos 2\phi] + I_o J_1(\eta) \sin 2\phi \sin 2\pi f_o t_o + I_o J_2(\eta) \cos 2\phi \sin 4\pi f_o t_o + \cdots \tag{28}$$

where J_i is the ith order Bessel function and $\eta = 2\psi \sin \alpha$ is the modulation index. Phase sensitive detection at f_o results in

$$I = I_o J_1(\eta) \sin 2\phi. \tag{29}$$

The amplitude ψ of the phase modulation is chosen so as to make η approximately 1.8, and hence maximize the sensitivity $(1/I_o)(dI/d(2\phi)) = J_1(\eta)$ to approximately 0.58 for small rotation rates.

Stability of these phase modulation techniques is of concern as they affect the scale factor of the gyroscope. For a relatively low performance device detecting, for example, 1 deg/h with 1 km of fiber wound with a 10 cm diameter and operating at $\lambda = 0.85$ μm, $2\phi = 1.2 \times 10^{-5}$ rad. This means that the power through the gyroscope I_o and the modulation index η must be stable to at least 1 part in 10^{-5}. One potential problem with these phase modulation techniques is their polarization dependence. If the phase modulation also introduces a polarization modulation, an offset of the zero point will result.

Several alternative schemes that overcome the need for this phase bias have been proposed and demonstrated. Early misalignment schemes [31], [52] do not satisfy the reciprocity requirements; the 3×3 gyroscope [53] and the dual-input gyroscope [54] do not have common point single-mode, single-polarization filters, placing stringent stability requirements on the directional couplers. A modification of the dual-input gyroscope [55] has the additional problem of not satisfying reciprocity requirements. A dual frequency gyroscope configuration that solves the phase bias problem differently will be discussed below.

3) Polarization Degree and Amplitude Stability: The reciprocity requirement has been quantified by considering the degree of polarization required to ensure drift stability [56]. Extending the polarization analysis [38], [40] of the ring interferometer to allow for an imperfect polarizer with a power extinction ratio of ρ^2, shows that the output intensity is given by [56]

$$I = 4|g_{xx}|^2 \cos^2 \phi + 4|\rho||g_{xx}| \cos\phi [|g_{xy}| \cos(\phi + \xi_1) + |g_{yx}| \cos(\phi - \xi_2)] \tag{30}$$

where g_{ij} are the complex elements of the Jones transmission matrix for propagation in one direction through the ring interferometer. It is assumed that the input polarization filter is aligned with the x-direction, and so g_{xx} describes, in amplitude and phase, the transmission of the x-polarization through the interferometer. Likewise, g_{xy} relates the y-polarized output to the x-polarized input and is a measure of the polarization cross-coupling in the entire interferometer, including the directional coupler and phase modulator. The phases $\xi_1 = \arg(\rho g_{xy}/g_{xx})$ and $\xi_2 = \arg(\rho g_{yx}/g_{xx})$ depend on the nature of the polarization cross-coupling and are likely to be environmentally sensitive. Terms of higher order in $|\rho|$ are ignored in (30), and if the polarization filter is ideal, $\rho = 0$ and only the first term remains.

Applying the sinusoidal phase modulation described above and retaining only the signal at frequency f_o reduces (30) to

$$I = 4|g_{xx}|^2 J_1(\eta)\sin 2\phi + 4|\rho||g_{xx}|J_1(\eta)\sin 2\phi[|g_{xy}|\cos\xi_1 + |g_{yx}|\cos\xi_2]. \tag{31}$$

Equation (31) includes an inconsequential assumption that small rotations only are being considered as this is the regime of interest. It can be assumed that $|g_{xy}| = |g_{yx}|$ if differential polarization losses are ignored, and as the phases ξ_1 and ξ_2 are likely to vary rapidly and unpredictably, their worst case values are inserted in (31) giving

$$I = 4|g_{xx}|^2 J_1(\eta)\left[1 + \frac{2|\rho||g_{xy}|}{|g_{xx}|}\right]\sin 2\phi. \tag{32}$$

To satisfy the gyroscope sensitivity quoted above, the quantity $2|\rho||g_{xy}|/|g_{xx}| < 10^{-5}$. The significance of this condition is that the stability of the gyroscope output depends on the amplitude extinction ratio $|\rho|$ of the polarization filter and the amplitude ratio of the polarization cross-coupling in the interferometer. If the polarization filter has a power extinction ratio of 60 dB, the power in the cross-polarization state in the interferometer must remain below 40 dB if the above condition is to be satisfied. Such good polarization control can be achieved with an active polarization stabilization scheme [44] that has demonstrated $|g_{xy}|/|g_{xx}| < 10^{-2} \cdots 10^{-3}$.

As an alternative to active polarization stabilization, great hopes have been placed on the availability of polarization holding fibers and schemes [57]-[59] to ensure that $|g_{xy}|/|g_{xx}|$ remains small, even in the presence of environmental perturbations. These fibers are designed to have large internal birefringences, far exceeding external perturbing birefringences, so that power injected into one of the polarization eigenmodes of the fiber will not be coupled into the other polarization mode by the external perturbations. State of the art high-birefringent fibers cannot maintain $|g_{xy}|^2/|g_{xx}|^2$ below approximately 0.1 over a kilometer length [60], but recent results [61] indicate that the power extinction ratio can be kept below 30 dB over a kilometer of fiber.

The stability of the polarization characteristics of the fiber directional coupler is an unknown quantity. Some work has been reported on the stability of fiber couplers [41], but their polarization stability has not been reported. To date, the fiber couplers employed in gyroscopes have been constructed with normal, low-birefringent fibers [33], [34]. There have been no reports of work on whether fiber couplers can be constructed with highly birefringent fibers. Additionally, it is not known if such couplers could maintain a specified polarization state to a very high degree.

One further comment is necessary concerning the degree of reciprocity required. It has been assumed throughout that the optical fiber is truly single mode. Propagation of even small amounts of the next higher order mode will introduce instabilities.

In the preceding discussion, emphasis has been placed on the need for a stable, well-defined polarization state to ensure reciprocity. The polarization filter guarantees reciprocity, but associated with it is the possibility of amplitude fluctuations. Active and passive schemes to overcome these fluctuations to a very high degree have been discussed. Recently, an alternative scheme has been reported that appears to be diametrically opposed to this discussion in that completely depolarized light propagates within the interferometer [33]. The schematic configuration of this gyroscope is shown in Fig. 22. The common point, single-mode, single-polarization filter ensures reciprocity in accordance with that discussed here, and the depolarizer, placed in the interferometer ring, overcomes the associated amplitude fluctuations. Under normal operation of the gyroscope (without the depolarizer), the two counterpropagating beams arrive at the output with time-dependent polarization states, varying amounts of which are passed by the polarization filter. The depolarizer, together with the super luminescent diode ensure that the two counterpropagating beams arrive at the output depolarized; that is, the intensity is evenly distributed over all polarization states. Environmental perturbations of the fiber coil change individual polarization states, but do not disturb the uniform distribution at the output and a constant fraction is passed by the polarization filter.

4) Backscatter and Reflections: The light that is Rayleigh backscattered in an optical fiber is another major source of noise in fiber gyroscopes that can limit gyroscope sensitivities to the tens of deg/h range [32], [62], [63]. At either end of the fiber coil, the backscattered light is superimposed on the transmitted light. Environmental variations cause the phase of this backscattered light to fluctuate at frequencies up to approximately hundreds of hertz [63]. If this backscattered light is at least partially coherent with the transmitted light, it can coherently interfere, and as a consequence, the phase difference between the two resulting output beams will exhibit fluctuations superimposed on the Sagnac phase. Any reflections within the interferometer from, for example, fused joints, fiber/chip interfaces, etc., have the same effect.

The magnitude of this backscatter-induced phase noise depends strongly on the coherence length of the laser source. For long coherence length lasers, the mutual coherence between the transmitted and the backscattered beams can be broken by adding a random phase modulation to one end of the fiber coil [63], analogous to the phase modulator used to introduce the $\pi/2$ phase shift in Fig. 20. Alternatively, a very large phase modulation can be applied to the fiber midway along the fiber coil [64]. These phase modulations tend to randomize the

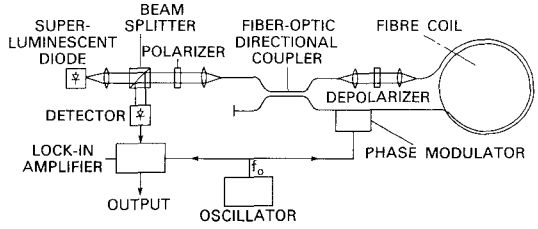

Fig. 22. Schematic configuration of the "depolarized" fiber optic gyroscope. The superluminescent diode and the depolarizer ensure the light in the fiber ring is depolarized (after [33]).

fluctuations in the phase of the backscattered beams such that, over an appropriate time internal, they average to zero.

A more convenient means of reducing this phase noise is to employ a short coherence length laser or super luminescent diode [33], [63]. This substantially reduces the fraction of the backscattered light that can interface with the transmitted light. This technique does not affect the power backscattered, but most of the backscattered light adds incoherently to the transmitted light, providing a constant background light [32]. A third and similar approach is to pulse the laser with a duration that is much less than the transit time through the fiber coil. Consequently, only a small fraction of the total backscattered power will arrive at the output coincidentally with the transmitted pulse and the remainder can be simply removed by gating.

Finally, as the trend toward the longer 1.3 and 1.5 μm wavelengths continues, the lower transmission losses come with the bonus of substantially reduced backscattered power.

5) Laser Fluctuations: As in any optical device, the noise associated with the laser source limits the performance of the device. Limitations of laser diodes are discussed in detail in Section VIII, so only those problems peculiar to the gyroscope are discussed here. As mentioned previously, a consequence of reciprocity in a Sagnac interferometer is that all the optical power returns through the input port if the interferometer is at rest. This means that apart from the 6 dB lost in the first beamsplitter (Fig. 20) and losses in the device, most of the laser power returns to the laser. Such large amounts of feedback can introduce substantial noise and other effects in laser diodes. To date, this has not been a major problem in experimental gyroscopes as the amount of power returned to the laser is usually small (microwatts and less). However, as lower loss devices are developed, a Faraday isolator may be necessary to prevent this feedback-induced noise.

In order to overcome the backscatter-induced phase noise, broadband lasers that have the output facet antireflection coated have been used. However, these devices are very susceptible to reflections and feedback, and tend to lose their broadband characteristics with relatively small amounts of feedback.

6) Dynamic Range and Data Rate: Applications-oriented problems are the dynamic range and data rate at which the gyroscope can operate. Gyroscope configurations discussed thus far operate with a single frequency and the output signal varies sinusoidally with induced Sagnac phase shift. As such, the output is linear only for Sagnac phase shifts up to approximately 1 rad when applications require dynamic ranges of 10^6. The dual frequency gyroscope, to be discussed below, has the advantage of large dynamic range and a digital readout. Apart from this, gyroscope development is lacking of suitable schemes for achieving large dynamic range. One possibility of increasing the dynamic range of the configuration discussed above is highlighted in (28). Both the sine and cosine of the Sagnac phase shift are available if both the first and second harmonic signals are used. Processing in the form

$$S = \arctan\left[\frac{a J_1(\eta) \sin 2\phi}{b J_2(\eta) \cos 2\phi}\right] \propto 2\phi \tag{33}$$

where a and b are constant multipliers, results in a signal that varies linearly with 2ϕ. It is questionable whether the required processing can be performed with sufficient accuracy and linearity.

Experimental gyroscope results that have been reported to date have been obtained with relatively long integration times, of the order of $0.3 \cdots 10$ s. These devices would not be capable of the high data rates required in low performance applications.

7) Alternative Configurations: Different gyroscope configurations have been demonstrated over the past few years, but many do not satisfy the reciprocity requirements cited previously and are unlikely to achieve the sensitivites required. One promising class of gyroscopes is the dual frequency gyroscope class and, in particular, the so-called phase-nulling gyroscope shown in Fig. 23. Basically, one beam passes through a frequency modulator before propagating through the fiber coil, while the counterpropagating beam passes first through the fiber coil and then through the frequency modulator. Then through a feedback system the voltage controlled oscillator (VCO) changes the frequency shift so as to null out the Sagnac phase shift. This frequency change is related to the rotation Ω through

$$\Delta f = \frac{2R\Omega}{\lambda n} \tag{34}$$

when R is the radius of the fiber coil and n is the effective index of the fiber mode. To date, this gyroscope has been constructed with discrete optical components [65] without incorporating some of the essential reciprocity requirements discussed above. However, there is no fundamental reason preventing their incorporation. The advantages of this configuration are its large dynamic range and digital output signal.

Dual frequency gyroscopes do have one disadvantage however. The two counterpropagating beams have different frequencies, and the fiber dispersion leads to an optical path length difference and a resultant breakdown of reciprocity. The dispersion-induced phase difference between the two counterpropagating beams can be expressed by

$$\Delta\phi = -\frac{2\pi L}{f}\frac{dn}{d\lambda}\Delta f \tag{35}$$

where f is the optical frequency. For a fiber length of 1 km, a frequency difference of 40 MHz, and operating at $\lambda = 0.83$ μm where the dispersion of fused silica $dn/d\lambda$ is approximately $0.02/\mu$m, this phase difference $\Delta\phi$ is approximately 3.3 rad. This is several orders of magnitude larger than the induced

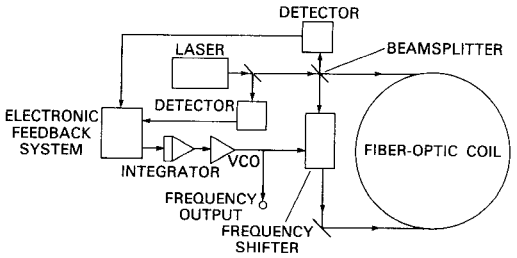

Fig. 23. Schematic configuration of the phase nulling optical gyroscope (after [65]).

Sagnac phase, and unfortunately, it will be environmentally sensitive. This problem may be reduced by using two frequency modulators that operate above and below a mean frequency. The optical path length difference decreases substantially if the gyroscope operates at the wavelength of minimum dispersion.

Status of Gyroscope Technology

Experimental fiber optic gyroscopes have demonstrated sensitivities in the degree per hour range [33], [35], [64] that are adequate for many low performance applications. These sensitivities are about two orders of magnitude better than the sensitivities demonstrated a year or two earlier. This increase in performance has been facilitated largely by the development of many fiber optic devices such as directional couplers, polarization transformers, phase modulators, polarizers and depolarizers, etc., which allow the integration of all the necessary optical components on a single uninterrupted length of fiber. By using these devices, many noise sources such as individual components motion and reflections from discrete components and fiber splices can be avoided. At the same time, a well-defined single mode propagates through the entire gyroscope. Better performances have been obtained with all-fiber devices, and gyroscopes that employ integrated optical components have not progressed as rapidly [35].

Two particular devices are singled out. One which relies on the propagation of a stable well-defined polarization state and one which propagates depolarized light in the interferometer ring. The first device is the complete all-fiber gyroscope, shown in Fig. 24, that has demonstrated a sensitivity of 16 deg/h [4] and very recently was reported to be in the degree per hour range or better [35]. The effect of environmental variations on this gyroscope have not been reported, but it obviously requires some control of the polarization in the fiber coil, either actively or passively with polarization-holding fiber, to achieve a constant scale factor. The second device, shown in Fig. 22, employs a depolarizer in the fiber ring and has the advantage of achieving a constant scale factor without additional polarization control. A long-term rms drift of approximately 10 deg/h has been demonstrated with this device [33].

Finally, typical results for a fiber gyroscope built in NRL are shown in Fig. 25. The gyroscope configuration is similar to that shown in Fig. 20, and the fiber length was 850 m wound on a 30 cm diameter drum. For the results shown in Fig. 25, an integration time of 1.25 s was used.

With the recent substantial interest in fiber optic gyroscopes, sensitivities will continue to improve and sensitivities of 0.1 deg/h and better have recently been seen at NRL, AEG Telefunken, M.I.T., and Stanford University.

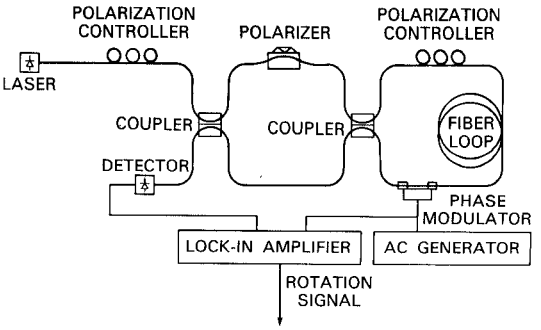

Fig. 24. Schematic configuration of the all-fiber gyroscope (after [34]).

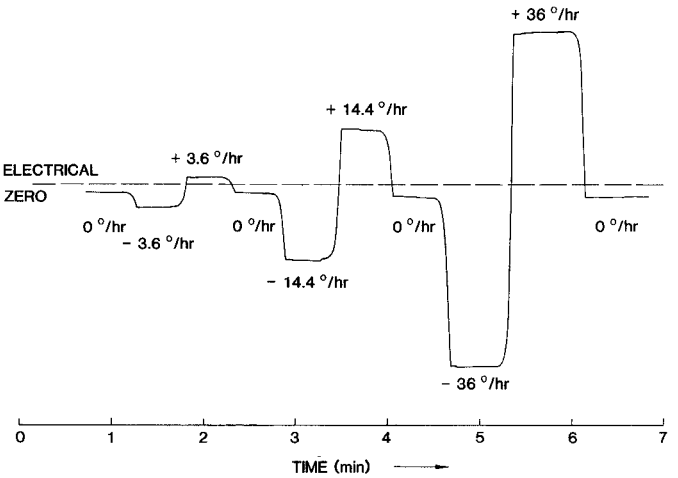

Fig. 25. Short-term sensitivity of an experimental gyroscope using 850 m of fiber wound on a 30 cm diameter drum.

V. Amplitude Sensors

Introduction

Sensor based on a wide range of transductance mechanisms can be characterized as amplitude sensors. Any transduction technique which produces a change in optical intensity proportional to an applied signal can be classified as such a sensor. Here, amplitude sensors are simply a class of sensors distinct from fiber interferometers [1], [2], [66], [67] or phase sensitive devices [68]. Although polarization-based sensors depend on detecting an optical phase shift, these sensors are included here for completeness.

As in the case for interferometric sensors, amplitude devices can be configured to detect a variety of fields [69], [70]. Since several amplitude sensors have been reviewed elsewhere [69], [71], the devices which have demonstrated encouraging performance as underwater acoustic sensors will be discussed. The acoustic detection threshold is an excellent parameter for sensor comparisons since the low underwater acoustic background makes the acoustic sensor performance most demanding.

A normalized modulation index

$$Q = \Delta I / I_o p \tag{36}$$

is a parameter which can be defined for any optical sensor. ΔI is the induced change in optical power, I_o is the output optical

power, and p is the pressure. The modulation index Q is attractive since the sensor response and the minimum detectable threshold are readily calculated from this parameter. Both the sensor response and the detection threshold are necessary to characterize the sensor performance. Following convention, the sensor response S is the differential voltage for a unit change in pressure

$$S = qI_oRQ \tag{37}$$

where q is detector responsivity in A/W and R is the detector load resistance in ohms.

Similarly, the shot noise limited detection threshold can be written as

$$P_{\min} = \frac{1}{Q}\left(\frac{2eB}{qI_o}\right)^{1/2} \tag{38}$$

where e is the electronic charge and B is the detection bandwidth.

The approach used here will be to calculate the normalized modulation index of several sensor types. The sensors included are fiber microbend [72]-[75] sensors, evanscent [76], [77], or coupled waveguide sensors [71], [78]. Moving fiber optic sensors [79], Schlieren [80] or grating sensors [81], polarization sensors [82]-[84], frustrated-total-internal-reflection [85] sensors, and the similar near-total-internal-reflection [86]. It is impossible for this paper to address each device in detail, therefore a brief description of each sensor and the normalized modulation index will be given. A more complete description of the microbend sensor will be given to familiarize the reader with the considerations of amplitude sensor design.

Fiber Microbend Sensor

The fiber microbend sensor [72]-[75] utilizes induced bending loss in an optical fiber. Light loss in the fiber depends upon inducing a coupling from propagating modes in the fiber to radiation modes. When the fiber is distorted in such a way that the distortion has wave numbers equal to the difference in wave number between the propagating and radiating modes, strong loss occurs.

Thus, as shown in Fig. 26, the microbend sensor employs a fiber between two ridged plates with an optimum periodicity depending upon the modal properties of the fiber. (This periodicity is typically in the millimeter range.) A displacement of the plates changes the amplitude of the bends resulting in intensity modulation. The modulation index can be written as

$$Q = \frac{dT}{dx}\frac{dx}{dp} \tag{39}$$

where T is the fiber transmission and x is the displacement of the plates. Although (39) is simple, it provides insight into the operation of fiber sensors. The modulation index depends on two parameters: dT/dx depends on the fiber properties and is strictly an optical parameter, while dx/dp depends on the mechanical design of the device. In order to optimize fiber sensors, both the optical and mechanical designs must be optimized and integrated.

Consider the optical portion of the modulation index. As previously mentioned, strong loss occurs when the wave number of the spatial distortion is equal to the difference in the wave number between the propagating and radiating modes. When periodic microbending is induced along the fiber axis, it has been demonstrated that power is coupled between modes [87] with longitudinal propagation constants β and β' such that

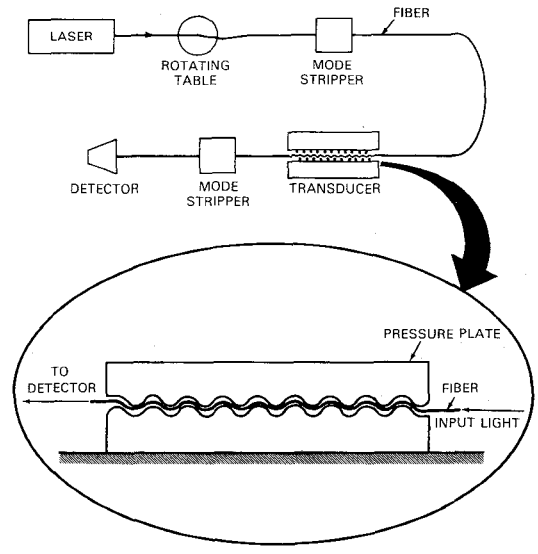

Fig. 26. Optical fiber sensor based on externally induced microbend losses (after [71]).

$$\beta - \beta' = \pm\frac{2\pi}{\Lambda} \tag{40}$$

where Λ is the mechanical wavelength of the periodic distortion. Using the WKB approximation [88], it can be shown that longitudinal propagation constants are given by [73]

$$\delta\beta = \beta_{m+1} - \beta_m = \left(\frac{\alpha}{\alpha+2}\right)^{1/2}\frac{2\sqrt{\Delta}}{a}\left(\frac{m}{M}\right)^{\alpha-2/\alpha+2} \tag{41}$$

where

m is the mode label,
M is the total number of modes,
α is a constant,
Δ is the fractional difference in refractive index between cladding and core center,

and

a is the core radius.

For parabolic index fibers $\alpha = 2$ and (41) yields [73]

$$\delta\beta = \frac{(2\Delta)^{1/2}}{a}. \tag{42}$$

This means that in a parabolic index fiber $\delta\beta$ is independent of m and all modes are equally spaced in k space. Thus, for parabolic index fiber a critical distortion wavelength exists for optimum coupling between adjacent modes [(40) and (42)] [73]

$$\Lambda_c = \frac{2a}{(2\Delta)^{1/2}}. \tag{43}$$

Fig. 27 plots dT/dx in μm^{-1} as a function of the mechanical

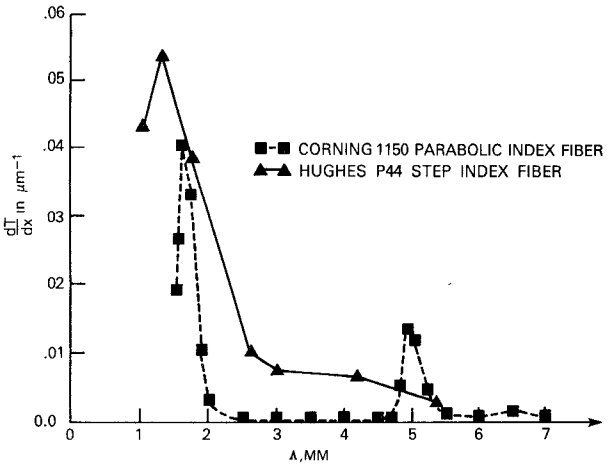

Fig. 27. Change in fiber transmission as a function of plate displacement (dT/dx) for parabolic and step index fibers (after [10]).

wavelength. The resonance phenomenon associated with the critical mechanical wavelength for parabolic fibers is clearly evident. A response at the third harmonic is also present. For step index fibers no such critical wavelength exists since the modes are not equally spaced [73]

$$\delta\beta = \frac{2\Delta^{1/2}}{a}\frac{m}{M}. \tag{44}$$

This shows that higher order modes are spaced further apart in k space than lower order modes, and therefore, small Λ's are required to couple higher order modes.

The optical transduction parameter dT/dx for step index fibers is also plotted in Fig. 27. It should be noted that the parabolic fiber was a commercially available fiber (Corning 1150) [73], while the step index fiber was specifically fabricated to enhance microbend losses [89, p. 44]. Available theory is not adequate, so currently fiber measurements similar to those of Fig. 2 are utilized to predict sensor response.

Calculation of the mechanical parameter dx/dp is also required to determine the modulation index. Optimization of this parameter has been analyzed in detail by Lagakos *et al.* [90] and therefore will not be discussed here.

In addition to optimizing the modulation index, the microbend sensor can utilize a specific optical bias to lower the detection threshold. If the sensor could be biased such that when no signal was present the photodetector is not illuminated (dark field) [72], the minimum detectable pressure then would be photodetector dark current limited:

$$P_{\min} = \frac{1}{Q}\frac{(2eI_{DC}B)^{1/2}}{qI_o} \tag{45}$$

where I_{DC} is the detector dark current. The microbend sensor, however, is nonlinear for this operating point. Determination of the potential improvement obtained by utilizing an optimum bias condition therefore includes a calculation involving the dynamic range. If a dynamic range of 100 dB is required, the maximum signal current is given by

$$I_{\max} = (2eI_{DC}B)^{1/2}10^5. \tag{46}$$

The dc current at the operating point must be at least as great as the desired signal current providing the detection threshold

$$P_{\min} = \frac{1}{Q}\frac{(2eI_{\max}B)^{1/2}}{qI_o}. \tag{47}$$

The ratio of (47) to (38) indicates that an improvement in the detection threshold of approximately 60 dB can be obtained by utilizing the optimum bias condition with $I_{DC} = 2.8 \times 10^{-11}$ A, $I_o = 1 \times 10^{-3}$ W, $q = 0.4$ A/W, and $B = 1$ Hz. The microbend sensor can utilize such a bias condition since the light which is radiated to the cladding, rather than that guided in the core, can be detected [72]. Thus, a microbend device must be designed such that the dc loss to the cladding is equal to $I_{\max}$.

An important advantage of the microbend sensor is that the optical power is maintained within a fiber. The transduction mechanism is compatible with multimode optical fibers and the prospect for low detection thresholds is promising. Recently, Lagakos [91] reported a detection threshold of approximately 60 dB re 1 μPa, a 40 dB improvement over the results of Fields and Cole [75]. Furthermore, these measurements were not made at the optimum operating point. Thus, substantial additional improvement is expected.

Evanescent or Coupled Waveguide Sensors

When the cores of two fibers are nearly adjacent over some distance, as shown in Fig. 28, light is coupled from one core to the other. For single-mode fiber, Sheem and Cole [76] have calculated the modulation index

$$Q = \sin\left(\frac{\pi L}{l}\right)\left\{\frac{\pi L}{Vl}\left[\frac{WV}{\rho}C_d + (3 + VD_o)(2\pi\rho/\lambda) \cdot (n_1^2 - n_2^2)^{-1/2} \cdot (n_1 C_{n1} - n_2 C_{n2}) + (3 + VD_o)\left(\frac{2\pi}{\lambda}\right) \cdot (n_1^2 - n_2^2)^{1/2} C_\rho\right] + \frac{2\pi c_L}{l}\right\} \tag{48}$$

where L is the interaction length, l is the beat length, V and W are parameters which depend on the modal properties of the fiber, ρ is the core radius, $D_o + 2$ is the ratio of core separation to core radius, n_1 is the index of the core, and n_2 is the index of the medium between the cores. The transduction coefficients C_d, C_{n1}, C_{n2}, C_ρ, and C_L are the rate of change with pressure of the core separation, core index, medium index, core radius, and interaction length, respectively. As can be seen, several physical effects take place to yield the resultant sensitivity.

It should be pointed out that their measured modulation index Q (7×10^{-11}/μPa) is several orders of magnitude higher than the calculated index Q(9×10^{-15}/μPa). Sheem and Cole [76] speculated that an accordian action which was not included in their calculation of C_d was responsible for the large sensitivity. Although single-mode technology was used in this demonstration, one of the principal advantages of amplitude sensors is that they may be fabricated with multimode fibers. Evanescent-type sensors have been demonstrated in multimode fibers with excellent results [77], [78]. Beasley [77] has measured detection thresholds on the order of 50 dB re 1 μPa for such a multimode device.

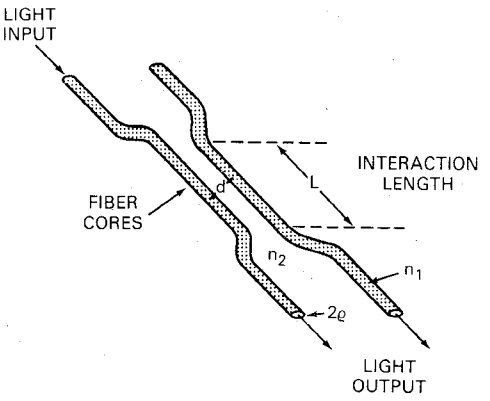

Fig. 28. Sensor configuration in which light intensity in one fiber is modulated by varing the evanescent coupling between two fibers (after [71]).

Although the demonstrated laboratory performance of the evanescent wave sensor is encouraging, a better understanding of the complex transduction mechanism is required. As in the microbend sensor, true optimization involves both optical and mechanical considerations. Any sensor utilizing a transduction mechanism which requires mechanical alignment with tolerances on the order of μm may be difficult to implement in practical devices.

Moving Fiber Optic Hydrophone

The moving fiber hydrophone [79] (Fig. 29) employs two fibers mounted such that their end surfaces are parallel, coaxial, and separated by about 2-3 μm. The acoustic waves or other perturbations to be measured in the medium induce relative motion between a fixed fiber and a fiber which is free to move. Relative fiber motion varies the light coupled between the two fiber ends, and thus modulates the transmitted light. Utilizing a simple geometric model, assuming a uniform light distribution in the core and that the fiber motion follows the acoustic displacement, the modulation index can be written as

$$Q = \frac{1}{\pi\omega\rho ca \sin\theta}(1 - \cos 2\theta) \tag{49}$$

where $\cos\theta$ is $d/2a$,

d is the dc fiber displacement,
a is the fiber core radius,
ω is the angular sound frequency,

and

ρc is the acoustic impedance.

Although this sensor has exhibited a moderate detection threshold of approximately 80 dB re 1 μPa [79], it lacks the appeal of other amplitude sensors. The major disadvantages of the moving fiber hydrophone is that it utilizes single-mode fiber, requires stringent mechanical tolerances, and the light is not confined to the fiber. The latter disadvantage may have a significant impact on long term reliability.

Schlieren or Grating Sensor

The Schlieren [80] or grating [81] sensor employs moving optical line gratings mounted to diaphragms which move under acoustic excitation (Fig. 30). Relative motion between the gratings in the direction perpendicular to the line pattern will modulate the transmitted light. Assuming that the gratings follow the acoustic displacement, the modulation index is given by

$$Q = 2/\rho c\omega\Gamma \tag{50}$$

where ρc is the acoustic impedance of the medium, ω is the angular sound frequency, and Γ is the grating period.

This sensor is promising since it does not appear to require the tight tolerances of the evanescent device. In addition, Spellman and McMahon [80] have demonstrated nonresonance detection thresholds on the order of 50 dB re 1 μPa. Conceptually, however, sensors like the microbend device which main-

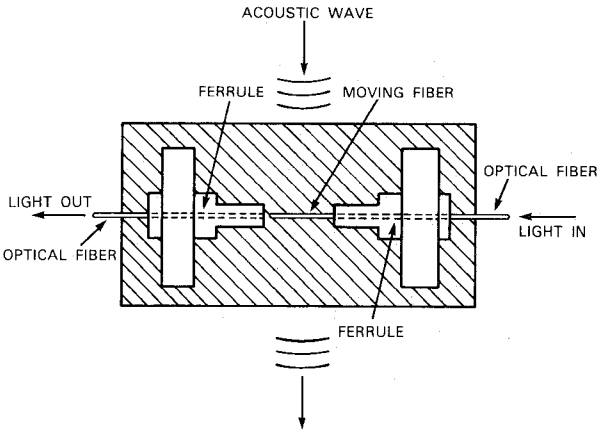

Fig. 29. Optical displacement sensor. Perturbations move one fiber relative to a second stationary fiber resulting in a modulation of transmitted light (after [79]).

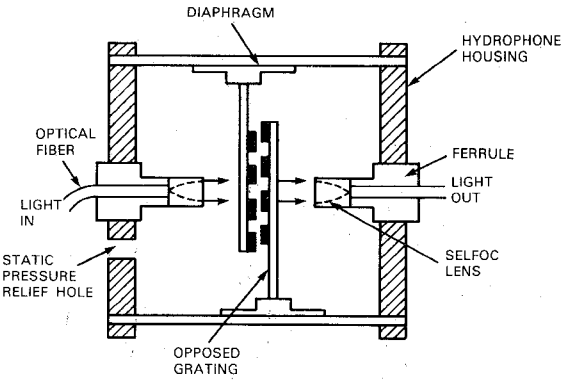

Fig. 30. Schlieren or moving grating sensor (after [80]).

tain the optical power within the fiber may provide better long term stability and reliability.

Polarization Sensors

Polarization sensors [82]-[84] are based on changes in the birefringence of single-mode fibers. A coil tension can be obtained by wrapping the fiber on a small cylinder which induces a large birefringence in the fiber. This birefringence provides independent propagation of two linearly polarized eigenmodes. An acoustic sensor, Fig. 31 for example, changes the birefringence of the fiber coil through variation of the strain induced in the fiber by the compliant cylinder. The resulting polarization rotation of the light propagating in the fiber is detected as an intensity change when the appropriate analyzer is used. Rashleigh [82] has predicted a sensor response which for small signals can be written as

$$Q = \frac{4.9 \times 10^6\, al}{Eb(1 - a^2/b^2)} \left(1\text{-}0.27\,\frac{a}{b}\right) \cdot \left[(1 - 2\nu) + (1 + \nu)\,\frac{a^2}{b^2}\right] \tag{51}$$

where

a is the fiber radius,
l is the fiber length,
E is the cylinder Young's modulus,
ν is the cylinder Poisson's ratio,

and

b is the cylinder radius.

In his acoustic sensor analysis [82] only the radial strain of the cylinder was considered. In a later paper on magnetic field sensing [83], Rashleigh points out that the axial strain of the cylinder contributes to improve sensor response. For high frequency applications, it has been demonstrated [84] that the polarization sensor response is comparable to that of interferometric devices.

The polarization-based sensors have many advantages. The light is confined within a single fiber and polarization components are simpler in principle than those required for the interferometer. The acoustic design of such a device benefits from the extensive research effort to optimize mandrel hydrophone configurations for the interferometric sensor. The chief disadvantage of these sensors is that like the interferometric devices they require single-mode fiber.

Frustrated-Total-Internal-Reflection Sensor

The frustrated-total-internal-reflection (FTIR) sensor [85] consists of two fibers with their ends polished at an angle to the fiber axis which produces total internal reflection (TIR) for all modes propagating in the fiber [Fig. 32(a)]. With the fiber ends sufficiently close, a large fraction of the light power can be coupled between the fibers. If one fiber is stationary and the second fiber experiences a vertical displacement, the light power coupled between the fibers varies due to the displacement and the light transmitted by the output fiber is modulated. Following the analysis of Spellman and McMahon [85], and assuming that the modulation index of the FTIR device is a function only of the gap displacement which equals the acoustic displacement

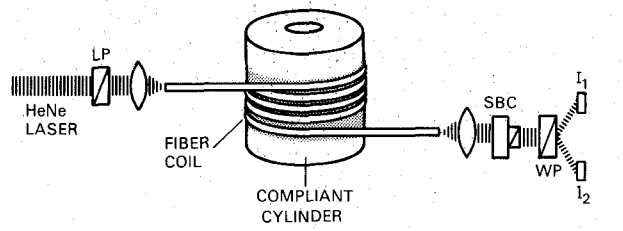

Fig. 31. Sensor configuration in which perturbations modify the polarization characteristics of light in the fiber resulting in an amplitude modulation of output signal (after [82]).

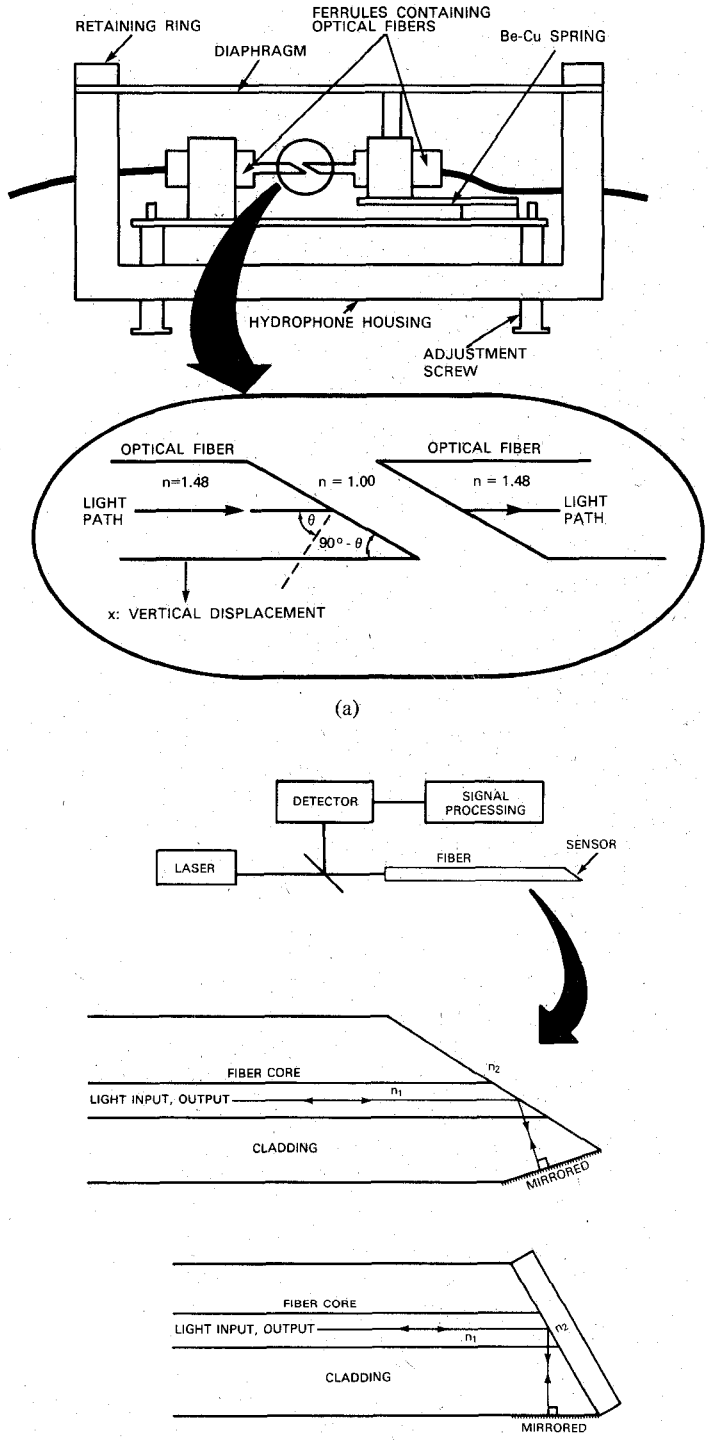

Fig. 32. (a) Frustrated-total-internal-reflection mode sensor (after [85]). (b) Near-total-internal-reflection sensor (after [86]).

$$Q = \frac{(z^2+\delta^2)^2\ [4z^2\delta^2\ \coth(\beta/2)\ \mathrm{csch}^2(\beta/2)]}{[(z^2+\delta^2)^2 + 4z^2\delta^2\ \coth^2(\beta/2)]^2} \cdot \left(\frac{4\pi}{\omega\rho c\lambda}\right)(n^2\ \sin^2\theta - 1)^{1/2} \quad (52)$$

where

ω is the angular frequency of the acoustic wave,
ρc is the acoustic impedance,

$$\beta = \left(\frac{4\pi x}{\lambda}\right)(n^2\ \sin^2\theta - 1)^{1/2}$$

x is the gap thickness,
λ is the optical wavelength,
n is the medium index of refraction,

and

θ is the incidence angle.

The functional form of $z(n, \theta)$ and $\delta(n, \theta)$ depends on the optical polarization, as indicated in [85].

The FTIR sensor has demonstrated a good detection threshold of approximately 60 dB re 1 μPa; however, the disadvantages of the sensor are that it requires tight mechanical tolerances and that the light is not maintained within the fiber. These disadvantages raise questions about the utilization of such sensors for field operation.

Near-Total-Internal-Reflection Sensor

The final sensor to be discussed, the near-total-internal-reflection (NTIR) or critical angle sensor [Fig. 32(b)] is very similar to the FTIR sensor. The NTIR sensor employs a single-mode fiber cut at an angle just below the critical angle. If the critical angle (given by $\theta_c = \sin^{-1}(n_2/n_1)$ is not near 45° (45° requires medium 2 to be a gas) then an additional angular cut is needed to allow the reflected beam to travel back through the fiber [see Fig. 32(b)]. This back reflected beam is then monitored after it exits the fiber. Acoustic pressure alters the index n_2 differently than n_1 and causes a slight shift of the critical angle, modulating the amount of light reflected. The modulation index has been determined [86]

$$Q = \frac{2hn_2^4\ \cos\theta\ (\cos\theta - (n^2 - \sin^2\theta)^{1/2})}{\rho c^2 n_1^2 (n^2 - \sin^2\theta)^{1/2}\ (\cos\theta + (n^2 - \sin^2\theta)^{1/2})^3} \quad (53)$$

where n_2 is the external medium index of refraction, n_1 is the fiber index of refraction, $n = n_2/n_1$, θ is the incidence angle, h is the photoelastic constant, ρ is the density of the medium, and c is the sound velocity.

The NTIR sensor is the only device included here which has not yet been demonstrated in a fiber configuration. This device is included since it operates on a fundamental optical mechanism which does not require mechanical designs typical of the other sensors. Therefore, the NTIR device has potential for operation as a tiny probe with a wide frequency response.

The modulation index is very dependent on how near to the critical angle the sensor is biased. The index can be increased by biasing closer to the critical angle; however, dynamic range and nonlinearity problems arise due to the shape of the reflectivity curve near θ_c. These problems suggest that feedback stabilization will be required to hold $\theta - \theta_c$ constant. As proposed by Phillips [86], a frequency tunable light source sensor is desirable for this since θ_c depends upon the optical wavelength. The NTIR device does not appear to offer the low detection thresholds of the other devices.

A comparison of amplitude sensors is shown in Table V. Although these devices are compared as acoustic sensors, they can sense a variety of fields. In general, the modulation index and the minimum detectable pressures are based on experimental results as indicated. The NTIR performance, however, was calculated from (53) utilizing a bias of $\theta - \theta_c = 0.01$ and the parameters of [86]. The NTIR sensitivity does not appear competitive with the other sensors; however, the unique properties of large bandwidth and small size make this device appealing for many applications. The response of all the other sensors depends critically on mechanical design which suggests a relatively narrow band of operation. Similarly, with the exception of the moving fiber and NTIR devices, the demonstrated performances are very competitive. The choice of an appropriate sensor thus depends on the specific application.

VI. Diode Laser Sensor

Introduction

In previous sections optical fiber sensors have been shown to offer great potential for a variety of applications. Such devices can be made extremely sensitive (in the case of interferometric sensors) by increasing the fiber length. However, for some applications less sensitive devices of very simple construction may be adequate for the application and more suitable because of their simplicity. In these cases interferometric fiber sensors appear somewhat unattractive because of their relative complexity. Recently, a new sensor [68], [92] has been developed which employs phase modulation of the light fed back into the cavity of a diode laser by an external reflector, i.e., a diode laser sensor. This device promises sensitivity competitive to existing devices and is packagable into a small device. The sensor also has the attributes of being very simple, relatively cheap, and having a large dynamic range. As in the case of the fiber sensors, the device can be configured so as to act as an acoustic, magnetic, current, and acceleration sensor.

Fig. 33 shows the most commonly utilized experimental arrangement. The sensor consists of a single-mode GaAlAs laser and an external reflector whose position is modulated by the incident field to be measured. The output signal is obtained either by monitoring the modulated intensity of the laser with a large area photodiode placed near to the facet of the laser, or by directly monitoring the diode drive current. In either of these configurations, the external reflector feeds light back into the semiconductor diode laser cavity; the phase of the light is determined by the distance d. When the light is fed back in phase with the light in the semiconductor laser cavity, the effect is to raise the facet reflectivity; conversely, when the light is fed back out of phase, the effective facet reflectivity is lowered.

The effective reflectivity of the laser cavity (typically, approximately 0.3) and the external reflector can be calculated as a function of d using the standard Fabry-Perot equation for a Fabry-Perot with three different reflectivity mirrors.

TABLE V
AMPLITUDE SENSOR DEMONSTRATED PERFORMANCE

SENSOR TYPE	MODULATION INDEX 1/μPa	MINIMUM DETECTABLE PRESSURE dB re 1μPa	ADVANTAGES	DISADVANTAGES
Microbend	4×10^{-10} (91)	60 (91)	Multimode fiber Light confined to fiber	Critical mechanical alignment
Evanscent	7×10^{-11} (76)	50 (77)	Multimode fiber Light confined to fiber	Critical mechanical alignment Light not confined
Moving Fiber	5×10^{-11} (79)	80 (79)		Single mode fiber Critical mechanical alignment Light not confined
Schlieren	1×10^{-10} (80)	50 (80)	Multimode fiber	Light not confined
Polarization	1×10^{-10} (82)	52 (82)	Light confined in fiber	Single mode fiber
FTIR	6×10^{-11} (85)	60 (85)	Multimode fiber	Critical mechanical alignment Light not confined
NTIR (86)	8×10^{-14} (Projected)	110 (Projected)	Point probe Large bandwidth	Single mode fiber critical mechanical alignment Low sensitivity

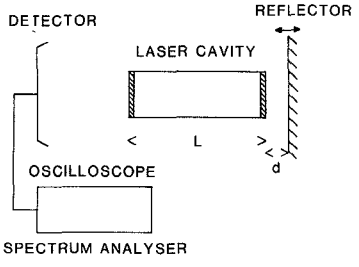

Fig. 33. Basic configuration of the diode laser sensor.

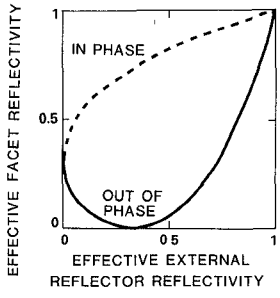

Fig. 34. Variation of the effective facet reflectivity with the effective external reflector reflectivity.

The values of the effective reflectance of the combination of the facet and external reflector as a function of the external reflector reflectance is shown in Fig. 34 for both the in-phase and out-of-phase case. Care must be taken in defining the external reflectance since it is difficult to couple 100 percent of the reflected light back into the diode. As a consequence of this, the external reflector reflectance is the product of external mirror reflectivity and coupling efficiency. As can be seen if the external reflector reflectance is equal to that of the laser cavity, the laser can be quenched by suitable adjustment of the external reflection position. However, experimentally, the effective reflector reflectance is below 10 percent; consequently, total quenching is never achieved. In any case it can be seen that the effective reflectivity of the combination is a strong function of the phase of the light feedback into the laser cavity, and consequently on the position of the external reflector. In the region where the values of external reflector reflectance are small, the following equation is appropriate for the effective facet reflectance.

$$R = R_o + 2(1 - R_o)\sqrt{rR_o}\ \cos\theta \tag{54}$$

where R_o is the facet reflectance without external feedback, r is the effective reflectance of the external reflector, and θ represents the phase of the reflected light.

The gain at lasing threshold g_o is given by

$$g_o = -\frac{1}{2L}\ln RR_o \tag{55}$$

where L is the laser cavity length and R is the effective facet reflectivity in the presence of feedback. Consequently, the threshold current level may be changed by altering the phase of the light fed back into the laser cavity [93]. Thus, by keeping the laser current constant (at threshold for the out of phase condition), a change in phase of the light fed back into the cavity results in a substantial change in the optical output of the laser. This effect constitutes the basic operating principle

of the diode laser sensor. Any field which perturbs the position of the external reflection may be measured by this technique. It should be pointed out that a fiber may be used to connect the external reflector to the diode laser. In this case the sensor may become sensitive to changes in the fiber characteristics and may be made an external sensor. Many of the characteristics of fiber sensors can then be incorporated into the diode sensor, thus affording added flexibility and perhaps sensitivity. When optical fibers are used in these sensors, the state of polarization of light propagating in the fiber and thus coupled back into the diode must be accounted for in the definition of the external reflectance.

Experimental Results

Fig. 35(a) illustrates how the output characteristics of an Hitachi HLP 1400 laser may be modified in the cases where there is: 1) no feedback, 2) feedback in-phase (to the left of the no feedback line), and 3) out-of-phase feedback (to the right) [68]. In this example, the reflectivity of the external reflector was 4 percent and the external reflector being positioned to within 10 μm of the laser's facet; the effective reflectivity was deduced to be less than 1 percent. By adjusting the laser's current to threshold for the out-of-phase feedback (approximately 72 mA) and continuously moving the reflector along an axis toward or away from the laser, the predicted intensity modulation takes place. For the HLP 1400 laser and a 4 percent reflector, the variation of laser output with reflector position is shown in Fig. 35(b) [68]. By placing the reflector at the point of maximum sensitivity A shown in Fig. 35(b), a small movement of the reflector (i.e., changing the phase of the feedback) results in relatively large changes in the output intensity. Consequently, the modulation of the external reflector's position (say by an acoustic wave) produces a substantial intensity modulation which is readily detected by the photodetector.

The sensitivity of this class of sensing device is determined by two factors: 1) the magnitude of the movement of the reflector to the incident field, and 2) the smallest detectable displacement of the reflector, i.e., sensor noise. Measurements of the minimum detectable movement of the reflector were made by mounting the reflector on a piezoelectric cylinder such that the reflector could be kept at the position of maximum sensitivity [point A in Fig. 35(b)]. The laser diode, reflector, and detector were mounted in an evacuated isolation chamber to remove extraneous noise produced by the ambient room noise. The frequency dependence of the minimum detectable displacement was then calculated from the noise voltage measured using a spectrum analyzer. Using this technique [68] displacements of approximately 3×10^{-4} nm and approximately 9×10^{-5} nm could be measured at 100 Hz and 1 kHz, respectively, with a 98 percent reflector, a 1 Hz bandwidth, and SNR of 1. The frequency dependence of the minimum detectable displacement for a 4 percent and 98 percent reflector placed approximately 10 μm from the laser facet is shown in Fig. 36. In both cases the minimum detectable displacement increases with a $f^{-1/2}$ dependence.

From Fig. 36 it can be seen that the minimum detectable phase shift is approximately 10^{-6} rad for the 98 percent

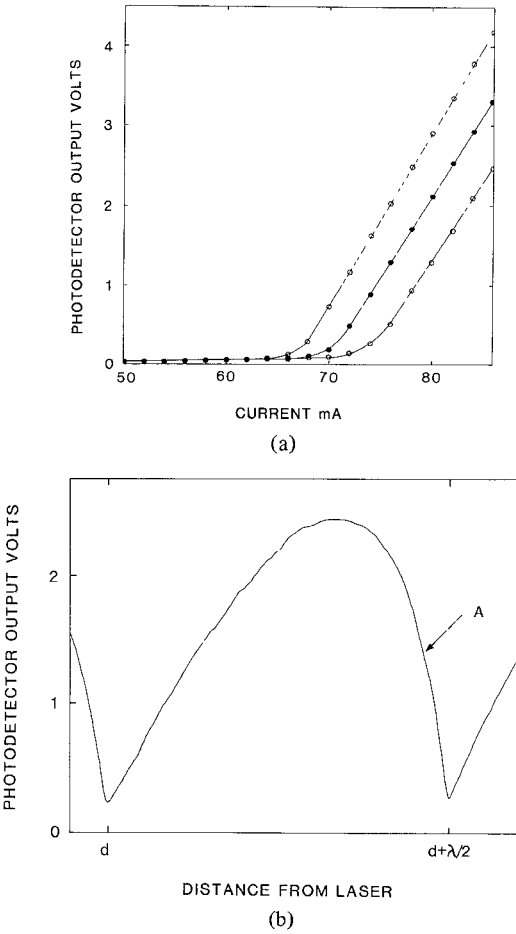

Fig. 35. (a) Laser output characteristics as a function of driving current for the free running laser (•) and the laser with feedback from a 4 percent reflector 10 μm away from the laser facet (○). (b) Laser output as a function of distance of the reflector from the laser facet; the periodicity is (λ/2). The optimum position for sensor application is marked by A (after [68]).

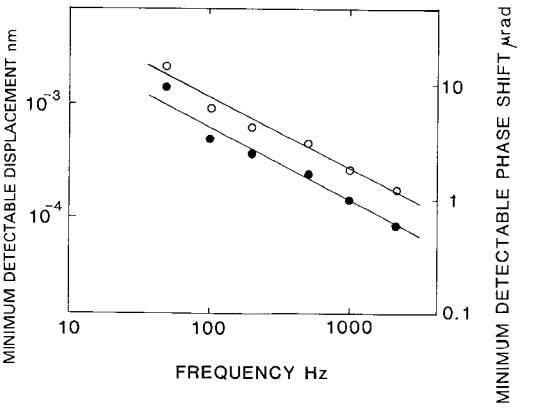

Fig. 36. Variation of the minimum detectable displacement and equivalent phase shift with frequency for 4 percent (○) and 98 percent (○) reflector (after [68]).

reflector. The calculated shot noise limit of this system corresponds to approximately 10^{-8} rad, similarly the thermal noise limit of the detector is approximately 10^{-8} rad. It can also be shown that the noise component due to low frequency fluctuation in the lasing wavelength of the diode laser [94]-[96] (the phase noise) corresponds to approximately 10^{-8} rad

owing to the small equivalent path length difference. However, measurements of the free running amplitude noise of the HLP 1400 laser [97] used in the experiment corresponds to approximately 10^{-6} rad phase shift, i.e., similar to that experimentally observed. Recent work by Goldberg *et al.* [98] has shown that feedback into the laser cavity has little or no effect (less than 1 dB on the amplitude noise of both CSP and BH GaAlAs laser which tends to confirm that it is the laser's intrinsic amplitude noise which limits the detectability to approximately 10^{-6} rad at 1 kHz. The frequency dependence of the amplitude noise ($f^{-1/2}$) is also similar [97] to that observed in the sensor configuration. It may be inferred that the greater sensitivity (see Fig. 36) of the sensor with the 98 percent reflector is due to the higher reflectivity allowing the laser to be run at a higher current (at the same modulation depth), thereby reducing the laser amplitude noise contribution [97].

To obtain a small minimum detectable phase shift in the sensor, it is necessary to lower the free running amplitude noise; this may be done in two ways: 1) use of transverse junction stripe type laser (e.g., the Mitsubishi TJS laser) whose free running noise is typically 10 dB lower than the CSP laser used to produce the durve shown in Fig. 36 [99], [100], or 2) cool the laser down to liquid nitrogen temperature (this has been shown to reduce the amplitude noise by a factor of ten). The frequency response of external mirror diode laser sensors is dependent on the mechanical resonances of the mirror and its support structure. For this reason membranes are used for most experiments so as to raise the resonant frequency. If the mirror is attached to a fiber and external perturbations of the fiber transmission properties are used to modify the characteristics of the reflected light, then the frequency response is dominated by the fiber characteristics and the discussions of Sections II and III apply.

The dynamic range of this sensor is limited by the minimum detectable phase shift (approximately 10^{-6} rad) and the maximum phase shift which is determined by the nonlinearity of the sensor response (i.e., approximately 0.1 rad). Thus, the dynamic range is approximately 10^5. This may, however, be increased by mounting the reflector on a piezoelectric cylinder and using an active feedback circuit to lock the sensor to the point of maximum sensitivity (phase-locked loop), as described by Dandridge and Tveten [101]. If there is sufficient gain in the electrical feedback loop, then the maximum phase shift may be increased to about π rad (dependent on frequency). Consequently, at low frequencies a dynamic range of 10^7 should be obtainable.

Sensor Configurations

1) Acoustic Sensor: The diode laser sensor may be configured as an acoustic sensor by using a thin glass membrane as the reflector (i.e., a 4 percent reflectance) [68]. The acoustic wave incident on the membrane modulates the membrane position so as to produce the change in phase of the feedback which is then measured as an intensity modulation by the photodetector. The sensor was adjusted to maximum sensitivity prior to measurement. A typical response is shown in Fig. 37, where a calibrated constant output acoustic source was used to drive the acoustic sensor. The device's response was similar over four orders of magnitude of acoustic sensitivity. A number of resonances (attributed to vibration resonances of the flexibility glass membrane) were noted. Careful design of the membrane will be necessary to move the resonances to higher frequencies yet still maintain a high sensitivity. Alternatively, an extended fiber coupled reflected may be employed to modify the frequency responses of the sensor.

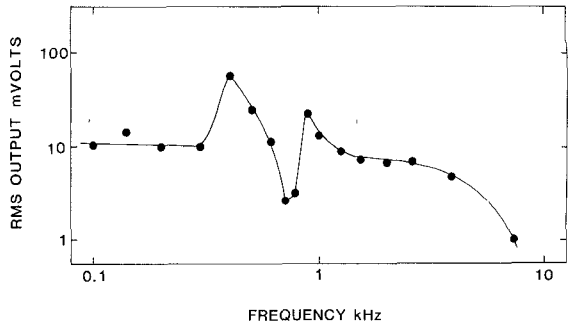

Fig. 37. Frequency response of the diode laser sensor acting as a microphone (after [68]).

2) Hydrophone: A simple hydrophone has been constructed using the principle employed with the acoustic sensor [100]. The whole sensor was placed within a plexiglas shell such that only the flexible membrane (in this case a thin gold coated mylar membrane) was in contact with the water. The configuration is shown schematically in the insert in Fig. 38. The response to underwater acoustic waves is shown in Fig. 38 along with the equivalent sea state zero noise. The device was tested without being backfilled; consequently, the device was very sensitive to small changes in depth. In later versions of this sensor, smaller membranes and backfilling with caster oil are being incorporated.

3) Magnetic Sensor: An ac magnetic field sensor was readily constructed using the diode laser sensor [92], [100]. A schematic of the sensor is shown in the insert of Fig. 39. The modulation of the reflectors position is achieved by mounting the reflector on a short piece of magnetostrictive Ni tubing. As in the previous sensors, the device was kept at maximum sensitivity by adjusting the voltage on the piezoelectric element with a compensator circuit. The frequency response of the sensor is shown in Fig. 39. The sensitivity of the device is dependent on the dc magnetic bias applied to the magnetostrictive element [83]. The frequency response was flat up to approximately 900 Hz, where the longitudinal resonance of the Ni tube is observed. The sensitivity at 500 Hz was approximately 4×10^{-5} G; this could be improved by making the magnetostrictive translation element from material with a larger magnetostrictive constant. As with the previous sensors, the response to the magnitude of the field was linear over greater than four orders of magnitude. Different configurations of the magnetic sensor using nonmagnetostrictive elements have also be constructed, which show similar performance characteristics to the device described above.

4) Current Sensor: The current sensor acts in a similar manner to the magnetic field sensor [92], [100]. A coil of wire through which the current to be detected is passed, is wrapped around the magnetostrictive element in the magnetic

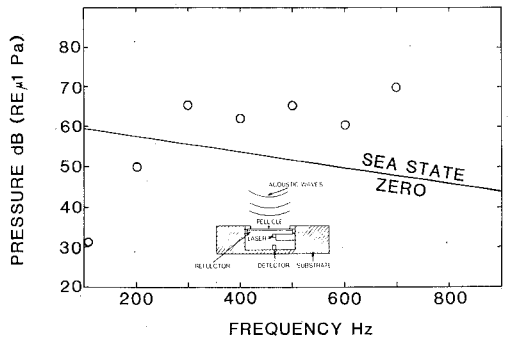

Fig. 38. Frequency response of the diode laser sensor acting as a hydrophone.

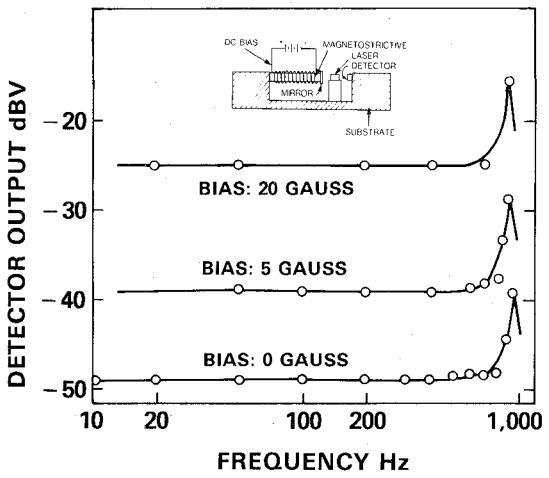

Fig. 39. Frequency response of the diode laser sensor configured as an ac magnetic field sensor. Results are shown for three different dc magnetic bias fields (after [92]).

sensor described above. The sensor then detects the magnetic field associated with the current passing through the wire. Consequently, the frequency response curve is identical to that of the magnetic sensor, again a dc bias magnetic field is used to increase the sensitivity. The absolute sensitivity of the device is dependent of the coil configuration, but typically current in the 10^{-5} to 10 A range may be measured [100].

5) Acceleration Sensor: The diode laser sensor was also configured to act as a sensitive accelerometer [100]. The external reflector is mounted on a short 4 mm cantilever arm, the external reflection (1 mm^2) also acts as the mass at the end of the cantilever. Acceleration along the axis of the laser cavity perturbs the position of the reflector from its rest position, thus producing the detectable phase shift. The device that has been constructed is very sensitive with a minimum detectable acceleration of approximately 10^{-6} G, but because of initial design deficiencies had a number of resonances in the frequency range of 10 Hz to 2 kHz. The device responded linearly to the magnitude of the acceleration. Straightforward improvements can be incorporated in these devices and devices with improved performance have been designed.

VII. Other Sensors

Optical fibers have been shown to offer great versatility for constructing sensors of various types and configurations. Changes in specially prepared fibers (specially doped or coated) have been used to sense a very large number of physical parameters. Additionally, traditional devices can be easily configured to accept fibers in place of previous electrical readout schemes. In this section many of these fiber sensor schemes will be examined.

Radiation Dosimeters

Glass fiber dosimeters are particularly well adapted to monitor radiation over large areas such as waste storage facilities, nuclear reactors, and accelerator compartments. The useful linear range of these devices range from below 10 mR to above 10^6 R and provide a 10^4 sensitivity increase over conventional glass block dosimeters. Fig. 40 shows a schematic representation of a fiber dosimeter. A typical fiber used for this application is a lead flint glass [102]. This type of fiber possesses the desired linearity to dosage and dosage rate, reasonable propagation loss, and acceptable damage fading characteristics.

In fiber dosimeters, the choice of light sources favors shorter wavelength regions [102], [103] because radiation induced losses increase dramatically as the wavelength decreases. In Fig. 41 the linear response of a Pb flint fiber is illustrated. As can be seen, it is linear over at least six orders of magnitude of dosage. The presence of large concentrations of lead in its fiber raises the absorption of X-rays relative to γ rays. Fiber coloration/damage is therefore energy-dependent with the optical loss induced per unit energy absorbed by 50 keV X-rays, a factor of 2.5 less than for γ-rays. Larger discrepancies for different X-ray energies exist [102] and the sensor must be calibrated for the energy of the ionizing radiation present.

The damage induced by ionizing radiation is known to fade with time and must be minimized while optimizing radiation sensitivity. Fig. 42 depicts the fading characteristics over 100 h interval of a sensing fiber waveguide (curve *a*) together with that of a DT-60 bulk glass block dosimeter (curve *b*). After 60 h the fiber dosimeter at 24° has stabilized with very little fading occurring. As the temperature increases, the fading increases up to a factor of ten for a 200°C temperature rise. Care must therefore be taken to know the environmental conditions the fiber dosimeter is exposed to.

A fiber dosimeter was tested and flown in the NTS-2 satellite [103]. This sensor outperformed the conventional dosimeters and illustrated two very desirable properties of fiber dosimeters: real-time dosimetry and quasi-archival dosimetry. These two characteristics heretofore were extremely difficult to achieve simultaneously.

Electrical Current Sensors

The principal sensors in this class to date rely on one of two effects—magnetooptics/striction or temperature effects. In its case of current induced temperature variations [104], a fiber was coated with a thin film of aluminum and a current passed down the metallic coating. Because of ohmic losses, the temperature of the coated fiber increased and this increase was sensed by placing the fiber in one arm of an interferometer. By changing the thermal mass of the control fiber, the frequency response of the sensor could be modified. ac response beyond 100 Hz could easily be achieved with microampere sensitivity being achieved at 10 Hz [104].

"Magnetostrictive" type current sensing has also been demonstrated with metal coated fibers [104], [105]. Using multimode coated fibers [105], a relatively high current sensor ($1\text{-}10^4$ A) was readily achieved, whereas the use of a single-mode coated fiber permitted 10^{-9} A to be measured. Sensi-

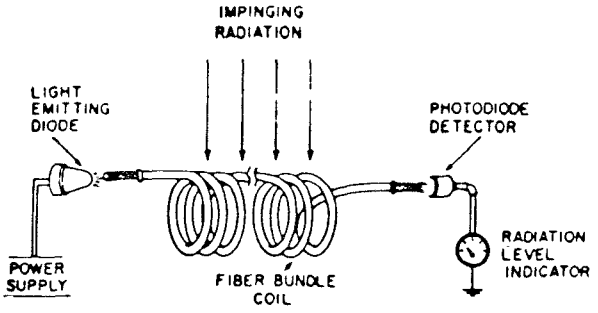

Fig. 40. Schematic representation of a fiber optic dosimeter. Ionizing radiation induces optical loss in the fiber and a photodetector records a reduced light level (after [103]).

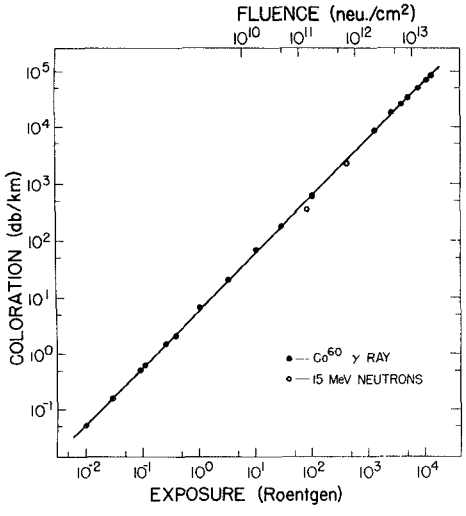

Fig. 41. Linearity of Pb flint fiber coloration versus gama ray exposure and 15 MeV neutron fluence at room temperature (after [102]).

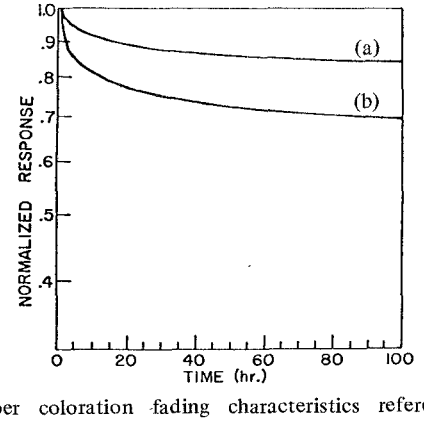

Fig. 42. Fiber coloration fading characteristics references to 1 h after removal from ionizing radiation. (a) Dosimeter sensing glass fiber, and (b) DT-60 glass dosimeter (after [103]).

tivities several orders of magnitude better than 10^{-9} A should be achievable with straightforward improvements. High frequency ac currents (>10 kHz) may be measured by these sensing techniques unlike the temperature type current sensors.

Magnetooptical effects in fibers have been utilized for fast response current sensing in high voltage applications [106]. In these sensors the sensor coil is wrapped around its current carrying conductor which has a magnetic field associated with it. This magnetic field interacts with the fiber via the Faraday effect and rotates the plane of polarization in the fiber. In twisted, low birefringent fibers, light is normally launched along a principal axis and the output state of polarization (SOP) is analyzed by detecting the intensities (I_1, I_2) in two orthogonal directions rotated by 45° to the principal axis. The two intensities are related to the Faraday rotation angle per unit length θ_F by [107]

$$P(z) = \frac{I_1 - I_2}{I_1 + I_2} = \frac{2\theta_F}{(\Delta B^2 + 4\theta_F^2)^{1/2}} \sin (\Delta B^2 + 4\theta_F^2)^{1/2}\, z.$$

The output in oscillatory with fiber length with maximum usable interaction length of $\Delta BL = \pi/2$, i.e., a quarter polarization beat period $L_p/4$. For adequate sensitivity, a long fiber is required and the intrinsic birefringence ΔB due to change irregularities and internal stresses must be minimized. To obtain the maximum interaction, twisting [106] and spinning birefringent fibers have been employed to overcome the linear birefringence. For large twist rates ($\xi \gg B$), the response is identical to a perfectly isotropic fiber ($P = \sin(2\theta_f z)$), with the amount of twisting or spinning depending on the size of ΔB in the untwisted fiber. Analysis indicates that if the spin rate [107] exceeds the intrinsic birefringence beat length by a factor of 10, residual polarization anisotropy may be reduced to a negligible value. Temperature variations were a major source of instability in these sensors and the use of twisted or spun fibers significantly decreases polarization variations with temperature. While magnetooptic current sensors are more sophisticated than other types of fiber current sensors, metallic coatings are not required, thus making them attractive for high voltage applications where the presence of a conductor may be undesirable.

Accelerometers

A highly sensitive single axis fiber accelerometer has been reported [108] with μg sensitivities and with the potential of at least an order of magnitude improvement possible. The accelerometer was in the form of a single harmonic oscillator consisting of a mass suspended between two fibers. When the device was accelerated in a direction along the fiber, a strain $\delta L/L$ was introduced in the supporting fiber proportional to the acceleration a. For a mass m, the induced phase shift for light propagating in the fiber of diameter d and with a Young's modulus Y was given by

$$\delta\phi = 2\pi m \delta L/\lambda = 8Lmn/\lambda Y d^2.$$

Placing the fiber accelerometer element (fiber and attached mass) in one arm of an interferometer, accelerations to 600 Hz were measured with sub-μg accuracies.

This single axis accelerometer demonstrated that fiber optical accelerometers could have better sensitivities than conventional devices. Further work is ongoing to reduce cross-axis coupling to below 2 $\mu g/g$, temperature sensitivities, and linearity to 1 part in 10^5. These improvements will make this accelerometer a prime candidate for aircraft navigational applications, and when used with a fiber gyro make possible on all fiber navigator.

A variant of the fiber accelerometer using the diode laser itself as an accelerometer is under development (see Section VI). In this case a small mass is attached to an external mirror which when accelerated becomes displaced. This displacement changes the phase of the light coupled back into the laser changing its optical output and current. Sensitivities similar to that of the fiber acceleration appear feasible. The advantage of this device configuration is its extremely small size (<1 cm^3).

Fiber Optical Spectrophones

This device is a derivative of the optical fiber acoustic sensors. In this case the fiber sensing coil is wrapped around/in an optical absorption cell containing the absorbing gas to be studied (Fig. 43). A modulated laser beam irradiates its cell and is absorbed by the trace gas/liquid to be detected. In the case of a gas, absorption of the radiation involves temperature and hence pressure change in the cell. Critical to this device is the ability to sense extremely small, modulated pressure signals induced via photoabsorption. The fiber sensor with its champion acoustic sensitivity is ideally suited for this application and its first successful demonstration of a spectrophone has recently been reported [109]. The initial device demonstrated an absolute sensitivity for a 1 dyn/cm^2 pressure of

$$\Delta\phi/\phi = 2 \times 10^{-10}.$$

Although the device was highly sensitive, it was a factor of 3 less sensitive than spectrophones using conventional piezoactive sensors. The fiber spectrophone sensitivity was limited by ambient noise and improvement of up to 10^4 appears feasible in the sensitivity of the fiber sensor. With these sensitivities, those spectrophones will become Brownian noise-limited. Experiments to demonstrate Brownian noise-limited optoacoustic detection with liquids are in progress with theoretical sensitivities corresponding to minimum detectable concentration of approximately 10^{-15} for typical absorbers appearing possible. The simplicity of construction and extreme sensitivity of these devices makes this fiber sensor the perfect candidate for highly sensitive spectrophone applications.

Temperature Sensors

There are several variations of this type of sensor which include placing an absorber, liquid crystal, or phosphor in the fiber path, or using the fiber itself as the sensor. In the case of all fiber sensor, a temperature change ΔT induces a phase shift $\Delta\phi$ in the light propagating in the fiber. This phase shift is readily detected using the fiber interferometer. The phase shift is given by

$$\frac{\Delta\phi}{\Delta T} = \frac{2\pi L}{\lambda}\left(\frac{ndL}{Ldt} + \frac{dn}{dT}\right)$$

which for fused silica fiber is dominated by the index change; however, the value of thermal expansion coefficients and the temperature dependence of the refractive index vary greatly for multicomponents glasses. Using typical glass fiber values, sensitivities of 10^{-8} °C are achievable. This extreme sensitivity is not required for the majority of applications where one degree accuracies are usually adequate. The fiber sensor can be made much less sensitive by proper choice of fiber glass composition or by coatings.

Other configurations which appear very attractive involve the use of semiconductor absorber in the light path. The variations of the semiconductor bandgap, and consequently optical absorption is used as the temperature sensitive probe. ±1°C accuracy was achieved over a 300°C temperature range [110].

The dielectric properties and high temperature characteristics of fiber temperature sensors make them particularly applicable to probing inside operating machines such as transformers and generators, in engine cavities, high voltage devices, and in chemical processing. The extreme sensitivities of these sensors make them attractive for scientific instruments and offer previously unachievable performance.

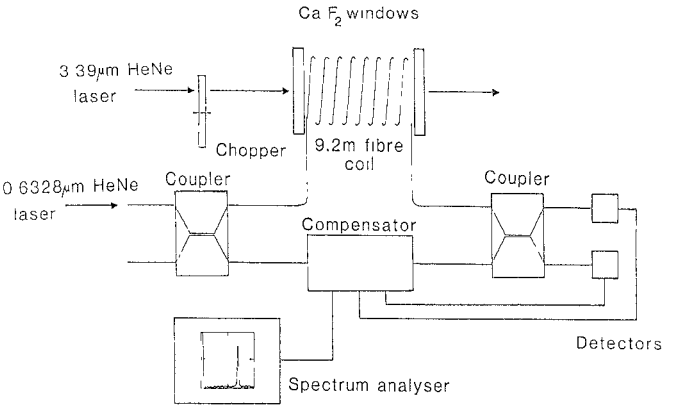

Fig. 43. Spectrophone configured using a fiber optical interferometric sensor (after [109]).

Miscellaneous Sensors

Various fiber sensor schemes have been envisioned for measuring liquid levels, displacement, strain, torque, fluid flow, etc. The first four of these in their many embodiments usually involved measuring a displacement. A coded mask is translated between the ends of an array of fibers. The number of fibers is usually determined by the accuracy required and the masks in many cases are Gray encoded. The masks are attached to the part whose displacement, strain, torque, or level is to be measured. Acceptable accuracies have been demonstrated in all of these sensor classes while operation in adverse environments (engine cavities, corrosive or electrically noisy environments, etc.) has been achieved. This latter advantage is one of the most attractive features of these sensors. In some of these sensor embodiments, fiber displacement of one fiber relative to a second fiber is the sensing mechanism, thus eliminating its need for a mask. In this case fiber displacement leads to a change in fiber transmission.

Fluid flow and vibration measurements in biological systems can be detected using the heterodyne signal from the moving item to be probed [111]. The fiber carries the light used to probe its desired event and scattered light is collected with a second fiber. Competitive sensitivities are usually achieved, while at the same time permitting probing in inaccessible areas with inert and nonpertubative probes.

VIII. Support Technology

Diode Laser Limitations

The small size, high efficiency and high output power of solid-state GaAlAs single-mode diode lasers make them a convenient source for fiber optic sensor systems. However, in changing from conventional gas laser sources (typically, HeNe lasers) to semiconductor sources, some disadvantages of the former are retained as well as new problems occurring. The problems of the output of these lasers, which manifest themselves as a loss of sensor sensitivity, may be split into three basic groups as follows:

1) amplitude noise,
2) coherence length,
3) phase noise.

However, the laser's performance is also strongly dependent

on light fed back into the laser cavity. The amplitude and phase of the light fed back into the laser cavity as well as the external cavity length are all important in determining the quality of the laser's output. Although many different structures of single-mode GaAlAs lasers have been fabricated, they all show generally similar behavior, when their optical output is considered. Although some of the relatively small differences in output with different structure lasers may be significant, it will be shown that although the output characteristics of diode lasers impose certain restrictions on the design of fiber optic sensors, it is still possible to build devices of high sensitivity.

It should be noted that although many papers have been written on diode laser noise, almost all have concentrated on high frequency (>100 kHz) noise. In sensor applications, typically low frequency properties (below 50 kHz) are of interest; consequently, only these papers will be discussed.

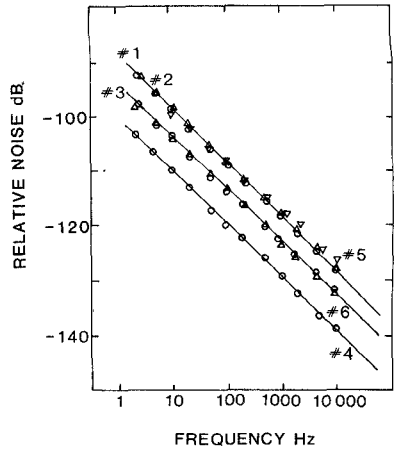

Fig. 44. Free running low-frequency amplitude noise of GaAlAs diode lasers, 1 Hz bandwidth. The lasers are described and numbered in the text (after [113]).

Amplitude Noise

In a conventional homodyne fiber interferometer configuration, the presence of amplitude noise of the source will produce a signal which will be indistinguishable from the interferometer's phase signal of interest [97]. In the interferometer a phase shift in one arm of the interferometer of frequency ω_m appears as a signal on the output of the interferometer at ω_m (the first order Bessel function J_1) [28], [112], the interferometer being electronically kept in quadrature. In the phase shift range below 0.1 rad, the phase shift at ω_m is directly proportional to the output of the interferometer at ω_m. The amplitude of J_1 of the signal at ω_m reaches a maximum $J_1^{\max}$ at a phase shift of approximately 1 rad (all values in rad correspond to rms values); this corresponds to almost the full modulation of the interferometer output. Consequently, to measure phase shifts of approximately 10^{-6} rad, it is necessary that one measure fluctuations at the signal frequency ω_m of approximately 10^{-6} of the dc output (in the quadrature condition the dc output of the interferometer is the mean of the maximum and minimum output of the interferometer). Thus, to detect 10^{-6} rad, the relative amplitude noise ($\Delta s/s$) of the source must be less than -120 dB (i.e., 10^{-6}). If the interferometer fringe visibility v is less than 1, then the minimum detectable phase shift ϕ_m is approximated by

$$\phi_m \simeq \left(\frac{\Delta S_m}{S}\right)_v^{\perp} \tag{56}$$

where ΔS_m represents the amplitude noise at ω_m and S the dc level.

Shown in Fig. 44 is the amplitude noise plotted as a function of frequency for a number of single-mode diode lasers [113]. The lasers shown in this figure are: 1) Hitachi HLP 1400 (channel substrate planar), 2) Hitachi HLP 2400u (buried heterostructure), 3) Hitachi 3400 (buried heterostructure), 4) Mitsubishi ML4307 (transverse junction stripe), 5) Laser Diode Lab CS234 (channel substrate planar), and 6) General Optronics TB47 (proton bombarded buried heterostructure with a tellurium mask to reduce spontaneous emission). Measurements of lasers within the same batch indicate that amplitude noise varies by ±2 dB for most of the devices. All of the lasers show a characteristic $f^{-1/2}$ dependence of the noise (note: this is a f^{-1} dependence when the electrical noise power, rather than voltage, from the detector is considered). The Mitsubishi TJS laser was the quietest of the six lasers investigated. From Fig. 44 it can be seen that below 1 kHz laser amplitude noise may be a potential problem. The problem may be reduced by using amplitude subtraction schemes which have been shown to reduce the noise by more than a factor of 10 at low frequencies. Consequently, for frequencies above 10 Hz by using amplitude subtraction and an interferometer of good fringe visibility, 10^{-6} rad phase shift may be achieved. From Fig. 44 it can be seen that some form of noise reduction will always be necessary for good (10^{-6} rad) sensor performance below 1 kHz.

It has been shown that relatively small amounts of light (approximately 10^{-3} percent) fed back into the laser cavity can cause the laser to jump to another longitudinal mode [114], [115] (but not always adjacent to the mode previously lasing). The phase and amplitude of the feedback may be adjusted so as to cause the laser to oscillate between longitudinal modes [115]. This has been shown to produce 20-60 dB of excess noise which is very undesirable [115]. It should be noted that longitudinal mode hopping in an unbalanced interferometer would typically produce a greater noise contribution owing to the wavelength shift than that due to the amplitude noise. It is therefore a requirement to suppress feedback induced mode jumping as the incurred noise is clearly unacceptable. It is necessary to ensure that fiber ends are either cut at an angle or index matched so as to avoid reflections. Splices and couplers in sensor systems must also be of high quality to avoid the 10^{-2}-10^{-3} percent reflections which are sufficient to produce mode hops.

Coherence Length

The linewidth of CW diode lasers have been measured by several authors. Nakawura *et al.* [116] reported measuring a linewidth less than 30 MHz at room temperature, using the Hitachi 1000 series CSP laser with a 10 cm Fabry-Perot etalon. Voumard [117], using a strip-geometry diode laser with the front facet antireflection coated and an external reflector to define the laser cavity, observed a linewidth of 17 MHz. Both these measurements were limited by the spectrometer used to measure the linewidth. More recent measurements by Miles *et al.* [118] and Okoshi *et al.* [119] have in-

dicated that typical linewidths in the free running GaAlAs are between 5 and 10 MHz. However, recent linewidth measurements of both channel substrate planar and buried heterostructure lasers have indicated that linewidth between similar lasers may vary 5 MHz and 100 MHz, presumably dependent on sample variations and age.

It can be seen that the lowest values of coherence length still correspond to 3 m, therefore path matching of the interferometer need only be made to approximately 1 m to obtain good fringe visibility. However, in the presence of optical feedback, line broadening, line narrowing, satellite-mode generation, and multimode generation have all been observed [118], [120]. Different modal structures observed under different values of feedback are shown [118] in Fig. 45. As can be seen, only relatively small amounts of feedback (<0.04 percent) are required to induce the relaxation oscillations shown in Fig. 45(b) and (c). Fig. 45(d) and (e) shows the laser running simultaneously on different longitudinal modes of the laser cavity. It should also be noted that at these latter levels of feedback the laser is exciting many longitudinal modes of the external cavity, which in conjunction with broadening of the external cavity modes, appears as severe line broadening of the laser's longitudinal cavity modes. In Fig. 45 it is these convoluted values of linewidth $\Delta\nu$ that are given. Broadening and satellite mode generation require path lengths to be matched to approximately 1 cm, whereas multilongitudinal mode operation of the laser cavity requires path length matching to 0.1 mm to ensure good fringe visibility [118]. Fortunately, relatively large amounts of feedback (>0.1 percent) are required to induce the deleterious effects associated with multimode operation. Backscattering from long lengths of fiber may, however, be a problem [121] and some form of isolation may be required. Line narrowing occurs with small amounts of feedback (approximately 10^{-3} percent), but line narrowing has been shown not to induce noise in interferometer systems [122].

It is clear that coherence length problems with the diode laser are not a serious problem in interferometer systems provided excessive values of optical feedback are not encountered. As mentioned above, care in design is necessary to ensure that reflection is kept below approximately 10^{-2} percent.

Phase Noise

Phase noise in an interferometer system is due to a change in the wavelength of the interferometer's light source and is strongly dependent on the optical path difference between the arms of the interferometer. If a HeNe laser is used to power the interferometer and the path difference is changed between 0 and 1 m, almost no increase in noise is noted in the interferometers output owing to the laser's good frequency stability. Very low frequency (<1 Hz) drifts may be observed and are due to macroscopic changes in the length of the laser's cavity. If, however, a diode laser is substituted as the source, the noise is observed to increase linearly [94], [96], [123], [124] with path difference, and at 1 m path difference the noise (at quadrature) may be approximately 3000 times greater than that observed at zero path difference. Results for a typical diode laser (a channel substrate planar Hitachi HLP 1400) are shown in Fig. 46 [94], [123], where the bandwidth is 1 Hz. The phase noise has a quasi $f^{-1/2}$ dependence similar to that observed for the amplitude noise [97], [123]. From Fig. 46 it can be seen that at 50 Hz the minimum detectable phase shift is approximately 100 μrad for a 40 cm path difference; this performance is unacceptable for many sensor applications. To achieve sensitivities below 1 μrad, it is necessary to match the paths of the interferometer to better than 1 mm, which may prove difficult for sensors whose arms may be 100 m long. The phase noise of different structures of laser (channel substrate planar, buried heterostructure, and transverse junction stripe) has also been investigated [123]; these results are very similar to those in Fig. 46.

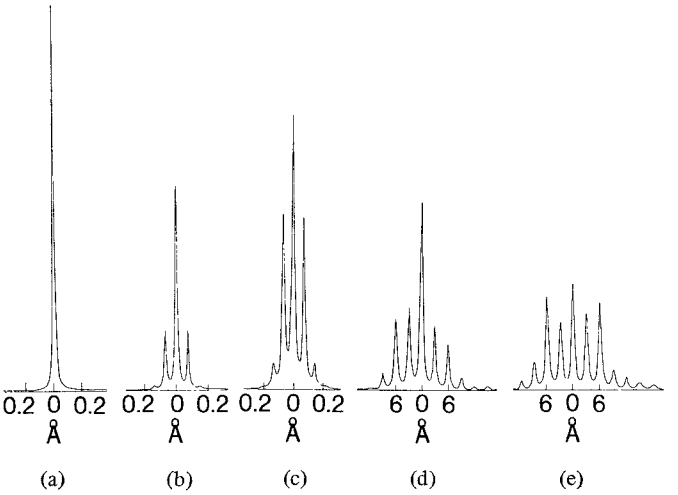

Fig. 45. Modal output of the Hitachi HLP 1400 diode laser for various amounts of optical feedback. (a) Free running laser, linewidth $\Delta\nu \simeq$ 5 MHz, (b) 0.04 percent feedback, $\Delta\nu$ = 0.02 GHz, (c) 0.06 percent feedback, $\Delta\nu$ = 0.12 GHz, (d) 0.3 percent feedback, $\Delta\nu$ = 1 GHz, and (e) 1.5 percent feedback, $\Delta\nu$ = 5 GHz (after [118]).

To reduce the effect of the phase noise contribution to the interferometer, it is possible to set up two interferometers powered by the same source and subtract the outputs (both interferometers being in quantrature). Thus, if only one arm of one interferometer is coupled to the external field to be measured, this combination would enable approximately 1 μrad sensitivity to be achieved for path length differences below 1 m. However, this method is unattractive and in practice may be unworkable. If small amounts of light are fed back (approximately 10^{-5} percent to 10^{-3} percent) into the laser cavity, before line broadening and multimode behavior occur, the linewidth of some lasers is observed to narrow [122], [125]. Typically, with lasers that exhibit this effect, the line may be narrowed by up to a factor of 100. Under these conditions, it has been noted that the diode laser phase noise has been reduced by up to a factor of ten [122]. However, the line narrowing and phase noise reduction effects are strongly dependent on the phase of the light fed back into the laser cavity (as well as the amplitude and external cavity length) [122]; consequently, some form of active phase compensation may be necessary to use these line narrowed lasers.

At the present moment, to avoid excess noise due to phase noise, it is necessary to use sensors such as the polarimetric type described by Rashleigh [82], [83], which have an in-

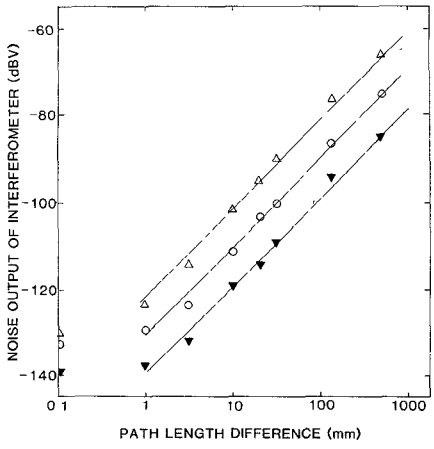

Fig. 46. Phase noise. Variation of the noise output of the interferometer (at maximum sensitivity, quadrature) in dB as a function of path length difference: △ 50 Hz, ○ 500 Hz, ▼ 2 kHz, 1 Hz bandwidth (after [123]).

trinsically small path difference, or to balance the Mach-Zehnder fiber interferometers paths to approximately 1 mm. It has been shown that matching of path lengths (to within ±1 mm) is possible in the following manner [126]. A sinusoidal current modulation of frequency ω is applied to the diode laser so as to produce a frequency modulation of amplitude f_ω such that the output of the interferometer is sinusoidal with amplitude ΔV_ω:

$$\Delta V_\omega = \frac{f_\omega 2\pi D}{c}$$

where c is the velocity of light in free space and D is the optical path difference. This equation only holds for voltage excursions within the interferometer's linear response region, and of course refers to the interferometer in quadrature. As the interferometer path difference can be determined absolutely, the longer arm of the fiber interferometer may be trimmed so as to produce $\Delta V_\omega = 0$. It should be noted, however, that differences in temperatures between the sensor and reference arm of the interferometer may substantially unbalance the interferometer's paths if long lengths of fiber are used.

Conclusion

The various properties of diode lasers that impose limitations and restrictions on the design of fiber optic interferometers have been discussed. It has been shown that by ensuring optical feedback levels below approximately 10^{-3} percent, path length differences are approximately 1 mm and amplitude subtraction schemes are used, 1 μrad performance down to 10 Hz should be possible.

Detection Systems

General Considerations: The purpose of the detection system is to transform the optical output of the sensor into an electrical signal proportional to the amplitude of the signal field. The detection systems for interferometric sensors are of necessity more complex than those for amplitude sensors. Therefore, the bulk of this section deals with the former category. A brief discussion of amplitude sensor detection systems is included as the last subsection. The starting point for the discussion of detection systems is the form of the electric field corresponding to the optical power in the signal and reference arms of the Mach-Zehnder interferometer. A generalized form of the interferometer connected to a generalized detection system is shown in Fig. 47. In the interest of simplicity the signal is considered to act only on the signal arm and the detection system to act only on the reference arm. The essential features of the various detection systems can be adequately discussed if the analysis is limited to linearly polarized light and the optics, including the fibers, is assumed to be polarization insensitive. In this case the electric field in the signal arm just before the combiner can be represented as

$$\vec{E}_s = \vec{E}_s^o \exp\left[i\omega t + S(t) + \phi_s\right]. \tag{57a}$$

The electric field at the corresponding point in the reference arm is

$$\vec{E}_r = \vec{E}_r^o \exp\left[i\omega' t + A(t) + B(t) + \phi_r\right]. \tag{57b}$$

In these expressions $S(t)$ is proportional to the signal amplitude. Typically, $S(t) \ll \pi$. The arbitrary phase factors in the signal and reference arms are ϕ_s and ϕ_r, respectively. In an ideal case ϕ_s and ϕ_r would be constant. However, in fiber interferometers ϕ_s and ϕ_r drift in a quasi-random fashion. In a few seconds the amplitude of this drift can easily be on the order of 2π or greater. Two modulator type terms (A and B) are included in the phase of the reference arm. These phase terms are generated [127] by stretching sections of fiber wound on piezoelectric cylinders by applying electrical signals to the piezoelectric elements. Depending on the type of detection system actually used, either A or B or neither is present. The convention used in this discussion is that A represents a phase produced by a feedback circuit to hold the interferometer at the quadrature condition. The phase B is always of the form $\phi_m \sin(\omega_m t)$. It is produced by driving the piezoelectric element with an oscillator.

The detection systems currently in use fall into five classes. These are passive homodyne (HOM), homodyne with dc phase tracking (PTDC), homodyne with ac phase tracking (PTAC), true heterodyne (HET), and synthetic heterodyne (SHET). The configuration in terms of Fig. 47 for each of these is given in Table VI.

Passive Homodyne: The most straightforward detection system in terms of electrical interaction with the interferometer is passive homodyne (HOM). Simple interference [128] of E_r and E_s in the balanced optical mixer implemented by the combining coupler and two photodiodes produces two electric signals V_1 and V_2.

$$V_1 = V_o\left[1 + \alpha\cos\left(S(t) + \phi_s - \phi_r\right)\right]$$

$$V_2 = V_o\left[1 - \alpha\cos\left(S(t) + \phi_s - \phi_r\right)\right]$$

$$V_3 = V_1 - V_2. \tag{58}$$

The signal V_o is proportional to the input optical power. The mixing efficiency α is dependent on the polarization state (angle between E_s^o and E_r^o) and on the splitting ratio of the combining coupler. The familiar quardrature condition is

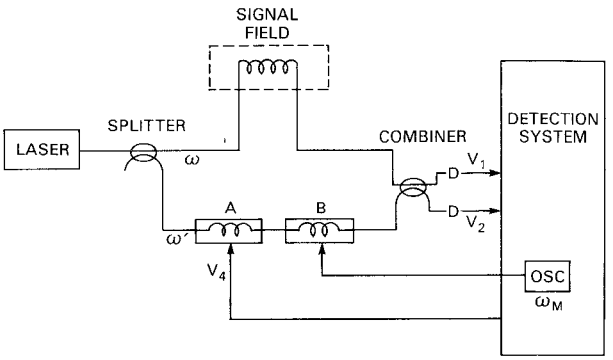

Fig. 47. Generalized fiber interferometer system. See Table VI and text for key to specific configurations.

TABLE VI
CONFIGURATION OF INTERFEROMETER FOR USE WITH VARIOUS DETECTION SYSTEMS. SEE TEXT FOR DEFINITION OF SYMBOLS.

Detection System	Frequency	A	B
HOM	$\omega = \omega'$	No	No
PTDC	$\omega = \omega'$	Yes	No
PTAC	$\omega = \omega'$	Yes	Yes
HET	$\omega \neq \omega'$	No	No
SHET	$\omega = \omega'$	No	Yes

$\phi_s - \phi_r = \pi/2$, for which case V_3 is proportional to $S(t)$ if $S(t) \ll 1$. The large drift in ϕ_s and ϕ_r causes fading by taking the interferometer away from the quadrature condition. In fact, the linear signal drops out completely if $\phi_s - \phi_r = 0$.

The processing of the signal $\cos(S(t) + \phi_s - \phi_r)$ is a nontrivial task. Although $S(t)$ and $\phi_s - \phi_r$ are usually confined to different frequency bands, the amplitude of $\phi_s - \phi_r$ is large and the cosine is a nonlinear function. Unless special circumstances prevail, there is no simple way to extract $S(t)$ from V_3. If another signal, proportional to $\sin(S(t) + \phi_s - \phi_r)$, in addition to V_3 is available, a solution to this problem is possible. To see this, let the signal proportional to the cosine be V_3 and that proportional to the sine be V_3'. Then

$$V_3 \frac{d}{dt} V_3' - V_3' \frac{d}{dt} V_3 \propto \frac{d}{dt}(S(t) + \phi_s - \phi_r). \tag{59}$$

The operations of differentiation and multiplication would typically be implemented with analog circuits. The result [rhs (59)] is a linear combination of $S(t)$ and $\phi_s - \phi_r$. If the drift in ϕ_s and ϕ_r is in a different frequency band than $S(t)$, this drift can be filtered from the output. The price in complexity of this HOM detection system is that two output signals 90° apart must be produced. A method for performing this function using a 3 × 3 coupler instead of the standard 2 × 2 as the arm combiner has recently been published [129]. Other methods using multiple interferometers may be possible.

The performance limitation in the HOM detection system is the distortion induced by the nonlinear processing. An examination of (59) reveals that an analog circuit realization of the identity $\sin^2\theta + \cos^2\theta = 1$ is necessary. All real four quadrant analog multipliers have inaccuracies which will corrupt the detected signal and limit the minimum detectable signal $S(t)$. In particular, if the drift is large enough so that the magnitude of $d/dt\ (\phi_s - \phi_r)/2\pi$ expressed in hertz is near the signal band, there will be significant signal degradation. Note that this condition can be achieved by a large steady drift. Drift frequency components near the signal band are not needed.

Phase Tracking Homodyne Detection Systems: The other two types of homodyne systems, PTDC and PTAC, employ piezoelectric stretching devices to maintain the quadrature condition $-\phi_r - A(t) + \phi_s$ approximately $\pi/2 + 2n\pi$. The phase A is obtained by applying a voltage to the piezoelectric stretching element which stretches the reference arm. The operation of the PTDC is the simpler of the two. In this case, the signal V_3 of (57) becomes

$$V_3 = 2V_o \alpha \cos(S(t) + \phi_s - \phi_r - A). \tag{60a}$$

Near the quadrature condition this becomes

$$V_3 = 2V_o \alpha [S(t) + \phi_s - \phi_r - A - \pi/2]$$
$$\equiv 2V_o \alpha [+\epsilon - A]. \tag{60b}$$

In this expression we have implicitly taken the phase modulo 2π. Since V_3 vanishes at the desired quadrature condition, it is an ideal error signal from the view point of linear control theory. If an appropriate feedback voltage can be produced from V_3 and applied to the piezoelectric element, the phase A can be made to exactly cancel ϵ, thus driving the error signal to zero. Such a feedback signal is the integral of V_3

$$V_4 = g \int_0^\tau V_3(t')\, dt'. \tag{61}$$

The complete form of this simple PTDC scheme is found in Figs. 47 and 48. The differential equation for the feedback signal V_4 is

$$\dot{V}_4 + g h 2V_o \alpha V_4 = g \alpha 2V_o \epsilon \tag{62}$$

where h is the volts to radians constant of the piezoelectric stretcher. The combination $gh2V_o\alpha$ is the gain bandwidth product of the feedback circuit. If the variation in $S(t)$ corresponds to frequencies much less than the gain bandwidth product, (62) ensures that $A = V_4 h = \epsilon$, the quadrature condition. Since $hV_4 = \epsilon = S(t) + \phi_s - \phi_r - \pi/2$, V_4 is linear in the signal S. Thus, $S(t)$ can be separated from ϕ_s and ϕ_r by appropriate filtering.

The strong point of the PTDC detection system is that it involves only linear operations. This is possible because the phase shift A produced by the piezoelectric element is a very linear function of the feedback voltage V_4. A drawback to the PTDC scheme is that the voltage range of the integrator producing V_4 is limited in a practical system to ±10 V. Once this voltage is approached, V_4 must be reset to zero. This reset produces a glitch in the output which must be appropriately smoothed out. The frequency of these resets can be reduced by making the piezoelectric element bigger and associated fiber longer. However, the larger the cylinder the more troublesome are cylinder resonance problems. An advantage of the PTDC scheme is that the feedback and balanced mixer

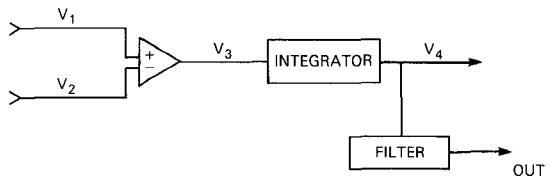

Fig. 48. Simple phase tracking dc (PTDC) detection system. The signal levels V_1, V_2, and V_4 are connected to the interferometer, as indicated in Fig. 41.

hold V_3 near zero, thus ensuring that amplitude fluctuations are common mode to both arms and thus cancel out.

More elaborate implementations of the PTDC scheme are possible [127]. Various filters can be incorporated to allow high gain bandwidth ratios to be used. Some gain control can be used to stabilize the gain bandwidth product. In the simple version described here, the output signal V_4 is independent of the optical power and mixing efficiency, but the gain bandwidth product depends on these parameters. Some of these improvements have been incorporated in NRL hydrophones. The hydrophones uses the PTDC scheme and has achieved very low noise and low distortion performance.

The PTAC scheme is a variant of the PTDC system. This system [130] uses an oscillating phase term (B) as well as a feedback phase (A). The oscillating phase causes the V_1 and V_2 signals to oscillate at ω_m (approximately 100 kHz) and its harmonics. The oscillating signal V_3 is mixed with the local oscillator which drives the "B" piezoelectric element (refer to Fig. 47). This mixing produces a slowly varying signal proportional to $\cos(S(t) + \phi_s - \phi_r - A)$. This will be recognized as being of the same form as V_3 in the PTDC scheme. The rest of the details of the feedback circuit are essentially identical to those of the PTDC detection system. The difference between the PTDC and PTAC scheme is that the PTDC scheme uses the low frequency signal V_3 directly as the error signal, while the PTAC scheme uses the amplitude of a high frequency "dither" signal as the error signal. In the appropriate small signal analysis, the error signal in both cases is proportional to $S(t) + \phi_s - \phi_r - A - \pi/2$.

Relative to the PTDC scheme, the PTAC scheme has the disadvantage of greater complexity and the advantage of better control of the gain bandwidth product. This PTAC detection system was used on the NRL Glassboard hydrophone [70]. Certain Sagnac effect gyroscopes have used a similar technique, although for a different objective.

Heterodyne Detection Systems: The heterodyne detection system (HET) is one of the simplest in concept [71]. Typically, a Bragg cell (not shown in Fig. 47) is used to shift the optical frequency of one arm of the interferometer with respect to the other. The output signal V_3 is in this case

$$V_3 = 2V_o\,\alpha \cos((\omega - \omega')\,t + S(t) + \phi_s - \phi_r). \tag{63}$$

Typically, $\omega' - \omega$ is in the range of 100 kHz. Equation (63) has the classic form of a phase modulated carrier. There are a number of ways of extracting a signal linear in $S(t)$ from this type of signal. Perhaps the simplest is to apply V_3 to the input of an FM discriminator tuned to $\omega' - \omega$. The output of the FM discriminator is then $d/dt\,(S(t) + \phi_s - \phi_r)$.

Before discussing the various methods of FM demodulation, we will consider another method for obtaining a signal of the form (63). It is desirable to identify another method because the Bragg cell is an undesirable bulk optical element which consumes at least a watt of electronic power and introduces alignment problems. We refer to this other method as synthetic heterodyne detection system (SHET) [5]. The signal V_3 in this case is

$$V_3 = 2V_o\,\alpha \cos(\phi_m \sin \omega_m t + S(t)\,\phi_s - \phi_r). \tag{64}$$

Typically, ϕ_m is approximately 1, ω_m approximately 100 kHz. This signal, which has components at ω_m, $2\omega_m$, etc., is the input to the circuit depicted in Fig. 49. The detailed operation of this circuit is described elsewhere [5]. In brief, one branch of the circuit produces

$$V_T = \cos(3\omega_m t) \sin(S(t) + \phi_s - \phi_r)$$

and the other produces

$$V_B = \sin(3\omega_m t) \cos(S(t) + \phi_s - \phi_r).$$

In one case $2\omega_m$ from the oscillator combines with ω_m from V_3 to produce $3\omega_m$. In the other case ω_m from the oscillator combines with $2\omega_m$ from V_3 to produce $3\omega_m$. Since the circuit operates at high frequency, 90° phase shifts are easy to obtain as required. The adder produces

$$V_H = V_B + V_T = \sin(3\omega_m t + S(t) + \phi_s - \phi_r). \tag{65}$$

This signal has essentially the same form as the heterodyne signal of (63). In fact, it is a heterodyne signal synthetically produced. The advantage of this method of producing the heterodyne signal is that bulk optics are not needed. Only a piezoelectric stretcher is used, and in principle, one such stretcher could serve a number of interferometers. A disadvantage of the synthetic approach is that phase drifts and amplitude mismatches will give rise to an output signal that is not a pure heterodyne signal. This will corrupt the output of the FM discriminator and limit the minimum detectable signal. Not enough data are available at this time to determine how serious a problem this is.

The final step in the heterodyne detection systems is the extraction of $S(t)$ from a signal of the form (65). As mentioned above, the simplest approach is to use an FM discriminator tuned to ω_m. However, conventional design of FM discriminators focuses on the problem of weak carrier amplitude and moderately strong signal. The interferometer, on the other hand, produces a strong carrier amplitude, but a very weak signal. In fact, $S(t)$ can be on the order of 10^{-6}. This corresponds to a modulation index of 10^{-6}. To deal with such a small modulation index, an FM discriminator with a very linear frequency transfer function is needed. Nonlinearity will effectively cause mixing of $S(t)$ and $\phi_s - \phi_r$, thus corrupting the signal. A special FM discriminator that can detect $S(t)$ of approximately 10^{-6} at 10 Hz in the presence of slow drift in $\phi_s - \phi_r$ has been built as part of the FOSS Program [131].

An alternative method for processing the heterodyne signal is a type of phase tracking using an all electronic feedback circuit [111], [132]. In this method the heterodyne signal is mixed with a local oscillator at ω_m which has an electrically controlled phase. The result of this mixing is of the form

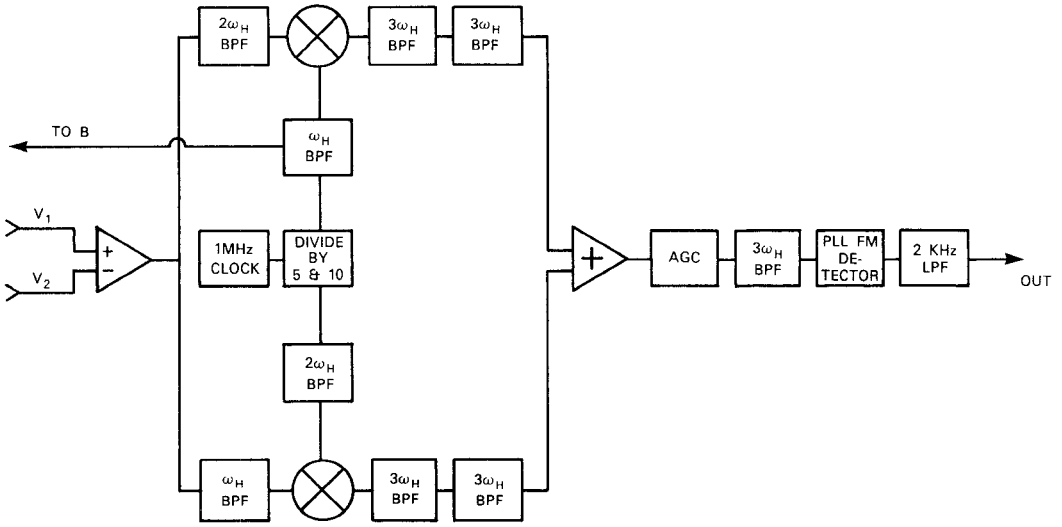

Fig. 49. Synthetic Heterodyne Detection System (SHET). The block element decoding is BPF = bandpass filter, LPF = low-pass filter, AGC = automatic gain control, PLL = phase-locked loop. The signal levels V_1, V_2, and B are connected to the interferometer, as indicated in Fig. 41.

of (60) with A now replaced with the controllable phase of the local oscillator. The feedback circuit is very similar to that used in the PTDC approach except that the feedback is to the electrically controlled phase of the local oscillator. It is possible to realize digital versions of this type of circuit using digitally controlled phase variation circuits and voltage controlled oscillator/counter combinations to digitize and integrate the error signal.

The principal advantage of the heterodyne detection systems is that no feedback to the interferometer is required. This avoids the reset problem that is common to both the PTDC and PTAC detection systems. Thus, the heterodyne approach may be favored if the drift rates are very large. A drawback of the heterodyne scheme is that the 100 kHz oscillator has some phase noise which corrupts the signal at low frequencies. In addition, FM discriminators are intrinsically less sensitive to low frequency signals than to high frequency signals. Thus, the heterodyne approach does not appear attractive for signals below 10 Hz.

Interferometric Sensor Detection System Tradeoff: There is no single optimum detection system for all applications of fiber optic interferometric sensors. Each scheme has advantages and drawbacks which must be evaluated in light of a particular application. Unfortunately, this evaluation is made more difficult because not all the detection systems have been investigated in sufficient detail. This is particularly true of the HOM and SHET systems. The current understanding of the tradeoff analysis is given in Table VII. Work aimed at better understanding this tradeoff problem is currently underway.

Amplitude Sensor Detection Systems: The generic amplitude sensor is very simple in concept. Optical power is carried to the sensor by an input fiber and an output fiber carries power away from the sensor to a photodetector. The power in the output fiber P_{out} is related to that in the input P_{in} by

$$P_{\text{out}} = P_{\text{in}}\, g\,(S(t) + S_o)$$
$$\simeq P_{\text{in}} \left[g\,(S_o) + \left(\frac{\partial}{\partial x} g(x) \right)_{x=S} S(t) + 0\,(S^2) \right]. \qquad (66)$$

Here g is a nonlinear function characteristic of a particular amplitude sensor, $S(t)$ is the signal field amplitude, and S_o is a bias. Unlike the case of interferometric sensors, the bias is conceived of as being stable—needing adjustment (by mechanical means) only at sensor calibration. The only issue that needs to be addressed from the viewpoint of detection systems is the choice of the bias.

There are three considerations which enter into the selection of the bias value: sensitivity, dynamic range, and noise. To maximize sensitivity, S_o is chosen to maximize $d(g(x))/dx/x = S$. Dynamic range is related to an appropriate distortion specification. The contribution from the terms higher than linear in (66) will introduce distortion into the output. This is particularly true in the dark field limit. In terms of (66) the dark field limit corresponds to $g(S_o) = 0$. However, $g(x)$ is a nonnegative function so that in the dark field limit the linear term is zero and the higher order terms dominate the output. Fluctuations in the first term in the square bracket of (66) produce noise. Larger values of $g(S_o)$ produce more noise. If this noise source is significant, operation near the dark field limit is favored. One possible source of fluctuation is laser

TABLE VII
INTERFEROMETRIC SENSOR DETECTION SYSTEM TRADEOFF CONSIDERATIONS

	HOM	PTDC	PTAC	HET	SHET
Feedback to interferometer required	No	Yes	Yes	No	No
Special interferometer configuration required	Yes	No	No	Yes	No
Signal distortion characteristics	Fair	Good	Good	Good	Fair
Complexity of electronics	Medium	Low	Medium	Medium	High
Freedom from reset glitch	Yes	No	No	Yes	Yes
Freedom from oscillator phase noise	Yes	Yes	Yes	No	No
Laser amplitude noise rejection	Yes	Yes	No	No	No

amplitude noise. It is possible, in principle, to cancel this noise if an independent monitor of the laser power is available.

More specific discussion of the tradeoff analysis governing the selection of the bias setting is possible only if the form of $g(x)$ is known. In general, there will be an optimal operating point for sensitivity, another for dynamic range, and a third for noise reduction. In the interferometric sensor, these three coalesce at the quadrature point. For the amplitude sensor a more complicated situation prevails.

IX. Summary and Conclusion

As a result of several years of research, a well-developed technology in the area of fiber optical sensors has evolved. Substantial progress has been realized and has been manifested in the form of new classes of sensors with unparalleled sensitivity, geometric versatility, and integrability. Completely optical systems appear feasible with small integrated fiber optical multisensors and optical telemetry capabilities. Efforts are presently under way to take the initially developed sensors tested in controlled environments, and to incorporate them in full field demonstrations. Prototype systems demonstrations involving the various sensors have the threefold purpose of technically evaluating components and systems concepts, of developing techniques for incorporation of these sensors into present systems, and of demonstrating and establishing the practical performance advantages of optical fibers.

Although not discussed in detail in this paper, the remarkable progress in the field of fiber sensors has come about in part because of substantial progress in componentry developments directed at fiber sensor applications. In particular, the availability of high quality fibers and semiconductor sources for telecommunications applications permitted the development of fiber sensors to capitalize on a large, existing guided wave componentry base. Componentry specialization has, however, been required to meet unique needs arising from several of the fiber sensor characteristics. Ruggedized 3 dB single-mode coupler development has been spurred almost entirely by the demands for this component in interferometric fiber sensors. This component more than any other has led to the realization of practical interferometric sensor configurations suitable for field deployment. Research on low frequency noise in diode lasers, polarization preserving fibers, and fiber compatibility detection techniques have also been accelerated by the drive to demonstrate high performance fiber sensors. These developments are expected in turn to increase the technology base for the guided wave telecommunications industry.

In this paper an outline of the advantages of optical fiber sensors has been discussed as well as a number of the existing technological problems. Amplitude sensors have been demonstrated for sensing magnetic, acoustic, acceleration, temperature, liquid levels, displacement, torque, and strain and offer cheap, easy to fabricate sensors suitable for harsh environmental deployment. Adequate sensitivities are readily achieved and packaging techniques have been demonstrated or appear to be available for many of these sensors. Remaining problems exist in several of the sensor types in the area of sensor biasing and calibration drift; however, efforts are being devoted to remedy these problems and solutions are becoming available, but are beyond the scope of this paper. Since the output of amplitude sensors is a modulated beam of light, these sensors are very compatible with fiber optical telemetry links. Higher sensor bandwidths and sensor output multiplexing schemes have been discussed by several laboratories and are being implemented.

The highest performance and the greatest flexibility in design of fiber sensors arise in the interferometric sensor designs. As is well known, optical interferometry is the most sensitive technique for measuring very small displacements. This capability has been capitalized on for the first time for field deployable application by the all fiber optical sensor. Extremely good sensitivities have been realized for several of the sensor types already; however, several other sensor types, most notably the fiber gyro, still remain to be demonstrated with performance approaching theoretical. The extended sensor configuration and very achievable geometric diversity in sensor design offered by fibers permit one to realize designs previously described analytically but heretofore not implemented using conventional technologies. Sensor loops, meshes, line arrays, spatially shaded elements, and point sensors are but a few of the geometries already demonstrated. The performance of these geometries verified previously predicted sensor characteristics and in many cases advantages were realized over existing technology.

Interferometric sensors appear to benefit most from fiber coatings technology. By changing the coating on the fiber, the sensing element can be changed from acoustic to magnetic or other sensor type. As an example, metal coatings are used to make current or magnetic sensor elements and to desensitize elements to acoustic fields. Compliant polymer coatings are generally used to enhance element sensitivity to acoustic fields and to damp out temperature effects. Placing the sensor element fiber on a suitable mandrel can be used to further increase sensitivity by as much as 15 dB. Having a common detection technology and changing only the coating on the fiber permits cost effective implementation of these sensors. Multisensors can easily be configured using a common detection scheme and various coated fiber sensor elements. This feature should find widespread application in specialized areas as oil field exploration, weapons guidance and targeting, and industrial processing control.

Prototype demonstrations have and are being planned for various fiber sensor types and indicate a high level of commercial and military interest. The technical competitiveness of optical sensors has been unquestionably demonstrated. Military and commercial interest stems in part from greater sensitivity, greater sensor versatility, compatibility with operation in harsh or noisy environments, and potentially lower cost. Increased performance will assist in improving laboratory instrumentation and appears suitable as calibration standards.

From the preceding discussions it can be concluded that toward the middle to end of the 1980's optical sensors are likely to find widespread usage. Market trends in this development were projected in a study [133] which predicts a \$58 million dollar market by 1990. This study indicates initial growth in the government/military and research and development markets with a \$2.4 million dollar level in 1980. This figure appears to be a factor of at least four lower than the actual figures spent in 1990 alone. Consequently, the \$58

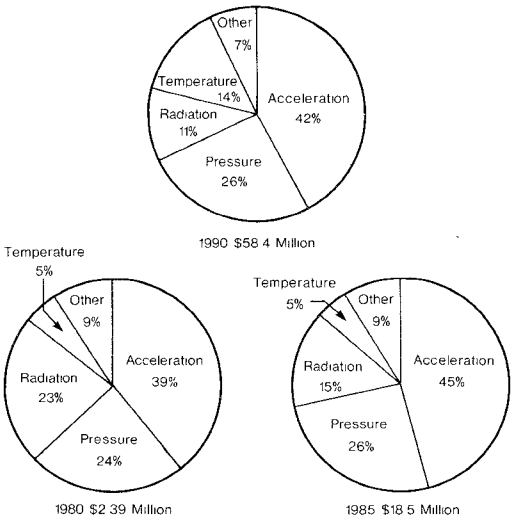

Fig. 50. Fiber sensor market projections (after [133]).

million dollar level for the 1980 time frame is considered to be very conservative. The survey concentrated on componentry and limited systems applications which have to date received the most publicity. Commercial and military systems' applications currently under discussion and development may not have been factored into this report. In any case, substantial market growth is projected in the 1980's as fiber sensors are perfected and incorporated into prototype and production systems. In Fig. 50 the functional application of fiber sensors are outlined [133]. Acceleration and rate sensors are felt to represent the largest market for fiber sensors in the GNOSTICS Concepts Inc. study [133]. Acoustic and pressure sensors for sonar applications were projected to make up 25 percent of the market in 1990. Twenty-one percent of the 1990 market was targeted to go for industrial uses such as temperature, fluid level, flow rate, current, strain, and magnetic field.

Unlike optical fiber development, the military was the first to heavily invest in fiber sensors in the late 1970's and led the development of this field. Their participation in this technology is seen as major throughout the 1980's with commercial concerns subsequently exploiting the technology base being developed. While the technical competitiveness of fiber sensors has been established, economic viability and field reliability are yet to be fully explored and it is these latter two factors which will determine the rate of commercial market exploitation and utilization of this technology.

In summary, optical fiber sensor technology has progressed rapidly during the past few years and the technical advantages are well documented and reviewed in this paper. Unique properties and outstanding sensitivity for several of the sensors ensure at the very minimum a specialty market. System level demonstrations are being planned by several major laboratories which, if successful, will secure a major market for the technology. From the preceding comments we conclude that optical fiber sensors will impact existing sensor markets in a significant fashion and that several sensing functions which were previously difficult to perform now become tractable and amenable to solution. During the next few years the viability of this technology will be established and substantial growth is expected.

Acknowledgment

The authors would like to thank their co-workers A. B. Tveten, K. Koo, R. O. Miles, C. A. Villarruel, H. F. Taylor, W. K. Burns, H. D. Dardy, J. Jarzynski, N. Lagakos, D. Tran, R. P. DePaula, and others whose work has been reported in this paper and whose efforts have helped achieve the rapid progress realized in fiber sensor development.

References

[1] J. A. Bucaro, H. D. Dardy, and E. Carome, "Fiber optic hydrophone," *J. Acoust. Soc. Amer.*, vol. 62, pp. 1302-1304, 1977.
[2] J. H. Cole, R. L. Johnson, and P. B. Bhuta, "Fiber optic detection of sound," *J. Acoust. Soc. Amer.*, vol. 62, pp. 1136-1138, 1977.
[3] D. A. Jackson, R. Priest, A. Dandridge, and A. B. Tveten, "Elimination of drift in a single-mode optical fiber interferometer using a piezoelectrically stretched coiled fiber," *Appl. Opt.*, vol. 19, pp. 2926-2929, 1980.
[4] J. A. Bucaro and T. R. Hickman, "Measurement of sensitivity of optical fibers for acoustic detection," *Appl. Opt.*, vol. 18, pp. 938-940, 1979.
[5] J. H. Cole, B. A. Danver, and J. A. Bucaro, "Synthetic-Heterodyne interferometric demodulation," this issue, pp. 540-543.
[6] J. H. Cole, T. G. Giallorenzi, and J. A. Bucaro, "Fiber interferometric demodulation and noise," in *Proc. Fiber Optics and Commun.*, Information Gatekeepers Inc., Brookline, MA, Mar. 1981.
[7] B. Budiansky, D. C. Drucker, G. S. Kino, and J. R. Rice, "The pressure sensitivity of a clad optical fiber," *Appl. Opt.*, vol. 18, pp. 4085-4088, 1979.
[8] R. Hughes and J. Jarzynski, "Static pressure sensitivity amplification in interferometric fiber optic hydrophones," *Appl. Opt.*, vol. 19, pp. 98-107, 1980.
[9] G. B. Hocker, "Fiber optic sensing of pressure and temperature," *App. Opt.*, vol. 18, pp. 1445-1448, 1979.
[10] J. F. Nye, *Physical Properties of Crystals*. Oxford, England: Oxford Univ. Press, 1976.
[11] S. P. Timoshenko and J. N. Goudier, *Theory of Elasticity*. New York: McGraw-Hill, 1970, ch. 4.
[12] N. Lagakos, E. U. Schnaus, J. H. Cole, J. Jarzynski, and J. A. Bucaro, "Optimizing fiber coatings for interferometric acoustic sensors," this issue, pp. 529-535.
[13] N. Lagakos and J. A. Bucaro, "Pressure desensitization of optical fibers," *Appl. Opt.*, vol. 20, pp. 2716-2720, 1981.
[14] G. B. Hocker, FOSS Workshop, Naval Res. Lab., Washington, DC, Dec. 12-14, 1979.
[15] J. Jarzynski, R. Hughes, T. R. Hickman, J. A. Bucaro, "Frequency response of interferometric fiber optic coil hydrophones," *J. Acoust. Soc. Amer.*, vol. 69, pp. 1799-1808, 1981.
[16] R. C. Jones, *J. Opt. Soc. Amer.*, vol. 31, pp. 488-503, 1941.
[17] L. Flax, P. K. Raju, J. George, and H. Uberall, "Resonating fields inside elastic scattering objects," *J. Acoust. Soc. Amer.*, vol. 68, pp. 973-979, 1980.
[18] E. K. Sittig and G. A. Coquin, *J. Acoust. Soc. Amer.*, vol. 48, pp. 1150-1159, 1970.
[19] S. K. Sheem and T. G. Giallorenzi, "Single mode fiber optical power divider: Encapsulated etching technique," *Opt. Lett.*, vol. 4, pp. 29-31, 1979.
[20] J. H. Cole and J. A. Bucaro, "Measured noise levels for a laboratory fiber interferometeric sensor," *J. Acoust. Soc. Amer.*, vol. 67, pp. 2108-2109, 1980.
[21] A. M. Smith, "Polarization and magnetooptic properties of single mode optical fiber," *Appl. Opt.*, vol. 17, pp. 52-56, 1978.
[22] A. Yariv and H. Winsor, "Proposal for detection of magnetostrictive perturbation of optical fibers," *Opt. Lett.*, vol. 5, pp. 87-89, 1980.
[23] F. M. Bozorth, *Ferromagnetism*. New York: Van Nostrand, 1951.
[24] A. Dandridge, A. B. Tveten, G. H. Sigel, Jr., E. J. West, and T. G. Giallorenzi, "Optical fiber magnetic field sensor," *Electron. Lett.*, vol. 16, pp. 408-409, 1980.
[25] J. Jarzynski, J. H. Cole, J. A. Bucaro, and C. M. Davis, Jr., "Magnetic field sensitivity of an optical fiber with magnetostrictive jacket," *Appl Opt.*, vol. 19, pp. 3746-3748, 1980.
[26] J. H. Cole, N. Lagakos, J. Jarzynski, and J. A. Bucaro, "Magneto-optic coupling coefficient for fiber interferometric sensors," *Opt. Lett.*, vol. 6, pp. 216-218, 1981.

[27] S. C. Rashleigh, "Magnetic field sensing with a single mode fiber," *Opt. Lett.*, vol. 6, pp. 19-21, 1981.
[28] D. A. Jackson, A. Dandridge, and S. K. Sheem, "Measurement of small phase shifts using a single mode optical interferometer," *Opt. Lett.*, vol. 5, pp. 139-141, 1980.
[29] K. Koo and G. H. Sigel, Jr., "Fiber optic magnetic sensors based on metallic glasses," to be published.
[30] G. B. Hocker, "Fiberoptic sensing of pressure and temperature," *Appl. Opt.*, vol. 18, pp. 1445-1448, 1979.
[31] V. Vali and R. W. Shorthill, "Fiber ring interferometer," *Appl. Opt.*, vol. 15, pp. 1099-1100, 1976.
[32] S. C. Lin and T. G. Giallorenzi, "Sensitivity analysis of the Sagnac-effect optical-fiber ring interferometer," *Appl. Opt.*, vol. 18, pp. 915-931, 1979.
[33] K. Bohm, P. Martin, K. Petermann, E. Weidel, and R. Ulrich, "Low-drift fiber gyro using a superliminescent diode," *Electron. Lett.*, vol. 17, pp. 352-353, 1981.
[34] R. A. Bergh, H. C. Leferere, and H. J. Shaw, "All-single-mode fiber-optic gyroscope," *Opt. Lett.*, vol. 6, pp. 198-200, 1981.
[35] H. J. Arditty, M. Papuchon, and C. Puech, "Fiber-optic rotation sensor: Toward an integrated device. A review," in *Proc. CLEO 1981*, paper THE1.
[36] A. Yariv, *Optical Electronics*. New York: Holt, Rinehart, and Winston, 1976.
[37] H. F. Taylor, Naval Res. Lab., Washington, DC, unpublished.
[38] R. Ulrich and M. Johnson, "Fiber-ring interferometer: Polarization analysis," *Opt. Lett.*, vol. 4, pp. 152-154, 1979.
[39] G. Schiffner, W. R. Leeb, H. Krammer, and J. Wittmann, "Reciprocity of birefringent single-mode fibers for optical gyros," *Appl. Opt.*, vol. 18, pp. 2096-2097, 1979.
[40] R. Ulrich, "Fiber-optic rotation sensing with low drift," *Opt. Lett.*, vol. 5, pp. 173-175, 1980.
[41] K. Koo, D. Tran, and S. Sheem, "Single-mode fiber directional couplers fabricated by twist-etching techniques," in *Proc. 3rd Int. Conf. on Int. Opt. and Optical Fiber Commun.*, San Francisco, CA, Apr. 1981, paper TuJ1.
[42] M. Johnson, "In-line fiber-optical polarization transformer," *Appl. Opt.*, vol. 18, pp. 1288-1289, 1979.
[43] H. C. Leferere, "Single-mode fiber fractional wave devices and polarization controllers," *Electron. Lett.*, vol. 16-17, p. 778, 1980.
[44] R. Ulrich, "Polarization stabilization on single mode fiber," *Appl. Phys. Lett.*, vol. 35-37, p. 840, 1979.
[45] D. M. Shupe, "Thermally induced nonreciprocity in the fiber-optic interferometer," *Appl. Opt.*, vol. 19, pp. 654-655, 1980.
[46] G. Schiffner, "Optical fiber gyroscope utilizing the Sagnac-effect," *Siemens Res. Rep.*, vol. 9, pp. 16-25, 1980.
[47] G. L. Mitchell, Honeywell Syst. Res. Cen., Minneapolis, MN, unpublished.
[48] W. C. Goss, R. Goldstein, M. D. Nelson, H. T. Fearnehaugh, and O. G. Ramer, "Fiber-optic rotation sensor technology, " *Appl. Opt.*, vol. 19, pp. 852-858, 1980.
[49] M. Papuchon and C. Puech, "Integrated optics–A possible solution for the fiber gyroscope," *Proc. Photo-Opt. Instrum. Eng.*, vol. 157, pp. 218-223, 1978.
[50] C. H. Bulmer and R. P. Moeller, "Fiber gyroscope with nonreciprocally operated, fiber-coupled $LiNbO_3$ phase shifter," *Opt. Lett.*, vol. 6, pp. 572-574, Nov. 1981.
[51] R. Ulrich and S. C. Rashleigh, "Beam-to-fiber coupling with low standing wave ratio," *Appl. Opt.*, vol. 19, pp. 2453-2456. 1980.
[52] M. H. McLandrich, "Fiber interferometer gyro performance and analysis," presented at Conf. on Phys. of Fiber Opt., Chicago, IL, Apr. 1980.
[53] S. K. Sheem, "Fiber-optic gyroscope with 3 × 3 directional coupler," *Appl. Phys. Lett.*, vol. 37, pp. 869-871, 1980.
[54] S. C. Rashleigh and W. K. Burns, "Dual-input fiber-optic gyroscope," *Opt. Lett.*, vol. 5, pp. 482-484, 1980.
[55] K. Hotate, Y. Yashida, M. Higashiguchi, and N. Niwa, "Rotation detection by optical fiber laser gyro with easily introduced phase-difference bias," *Electron. Lett.*, vol. 16, pp. 941-942, 1980.
[56] E. C. Kintner, "Polarization control in optical fiber gyroscopes," *Opt. Lett.*, vol. 6, pp. 154-156, 1981.
[57] R. H. Stolen, V. Ramaswamy, P. Kaiser, and W. Pheibel, "Linear polarization in birefringent single mode fibers," *Appl. Phys. Lett.*, vol. 33, pp. 699-701, 1978.
[58] I. P. Kaminow, "Polarization in optical fibers," *IEEE J. Quantum Electron.*, vol. QE-17, pp. 15-22, Jan. 1981.
[59] S. C. Rashleigh and R. Ulrich, "High birefringence in tension-coiled single-mode fiber," *Opt. Lett.*, vol. 5, pp. 354-356, 1980.
[60] S. C. Rashleigh, W. K. Burns, R. P. Moeller, and R. Ulrich, "Polarization holding in birefringent single mode fibers," *Opt. Lett.*, vol. 7, p. 40, Jan. 1982.
[61] T. Katsuyame, H. Matsumura, and T. Sugamume, "Low-loss single-polarization fibers," *Electron. Lett.*, vol. 17, p. 473, 1981.
[62] C. C. Culter, S. A. Newton, and H. J. Shaw, "Limitation of rotation sensing by scattering," *Opt. Lett.*, vol. 5, pp. 488-490, 1980.
[63] K. Bohm, P. Russer, E. Weidel, and R. Ulrich, "Low-noise fiber-optic rotation sensing," *Opt. Lett.*, vol. 6, pp. 64-66, 1981.
[64] R. Bergh, H. Leferere, and H. J. Shaw, "All single mode fiber gyroscope," in *Proc. 3rd Int. Conf. on Integrated Opt. and Opt. Fiber Commun.*, San Francisco, CA, Apr. 1981, paper W12.
[65] R. F. Cahill and E. Udd, "Solid-state phase-nulling optical gyro," *Appl. Opt.*, vol. 19, pp. 3054-3056, 1980.
[66] P. Shajenko, "Fiber optic acoustic array," *J. Acoust. Soc. Amer.*, vol. 59, p. 592, 1976.
[67] B. Culshaw, E. Davies, and S. Kingsley, "Acoustic sensitivity of optical-fiber waveguides," *Electron. Lett.*, vol. 13, pp. 760-761, 1977.
[68] A. Dandridge, R. O. Miles, and T. G. Giallorenzi, "Diode laser sensor," *Electron. Lett.*, vol. 16, pp. 948-949, 1980.
[69] J. A. Bucaro, J. H. Cole, J. Jarzynski, W. K. Burns, and T. G. Giallorenzi, "Optical fiber sensor development" in *Physics of Fibers, vol. 2, Advances in Ceramics*, Bendow and S. S. Mitra, Eds. Columbus, OH: Amer. Ceramic Soc., 1981, pp. 493-514.
[70] J. H. Cole, T. G. Giallorenzi, and J. A. Bucaro, "Advances in optical fiber sensors, Integrated optics," *Proc. Soc. Photo-Opt. Instrum. Eng.*, vol. 269, pp. 115-124, 1981.
[71] J. A. Bucaro and J. H. Cole, "Acousto-optics sensor development," in *Proc. EASCON 1979*, IEEE Pub. 79CH1476-1 AES pp. 572-580.
[72] N. Lagakos, T. Litovitz, P. Macedo, R. Mohr, and R. Meister, "Multimode optical fiber displacement sensor," *Appl. Opt.*, vol. 20, pp. 167-168, 1981.
[73] J. N. Fields, E. K. Asawa, C. P. Smith, and R. J. Morrison, "Fiber-optic hydrophone" in *Physics of Fibers, vol. 2, Advances in Ceramics*, Bendow and S. S. Mitra, Eds. Columbus, OH: Amer. Ceramic Soc., 1981, pp. 529-538.
[74] N. Lagakos, P. Macedo, T. Litovitz, R. Mohr, and R. Meister, "Fiber optic displacement sensor" in *Physics of Fibers, vol. 2, Advances in Ceramics*, B. Bendow and S. S. Mitra, Eds. Columbus, OH: Amer. Ceramic Soc., 1981, pp. 539-544.
[75] J. N. Fields and J. H. Cole, "Fiber microbend acoustic sensor," *Appl. Opt.*, vol. 19, pp. 3265-3267, 1980.
[76] S. K. Sheem and J. H. Cole, "Acoustic sensitivity of single mode optical power dividers," *Opt. Lett.*, vol. 4, pp. 322-324, 1979.
[77] J. D. Beasley, "Multimode optical evanscent-wave acoustic sensor," *J. Acoust. Soc. Amer.*, vol. 68, pp. 595-598, 1980.
[78] E. F. Carome and K. P. Koo, "Multimode coupled waveguide sensors," *Opt. Lett.*, vol. 5, pp. 359-361, 1980.
[79] W. B. Spellman, Jr. and R. L. Gravel, "Moving fiber-optic hydrophone," *Opt. Lett.*, vol. 5, pp. 30-31, 1980.
[80] W. B. Spellman, Jr. and D. H. McMahon, "Schlieren multimode fiber-optic hydrophone," *Appl. Phys. Lett.*, vol. 37, pp. 145-147, 1980.
[81] B. W. Tietjen, "The optical grating hydrophone," *J. Acoust. Soc. Amer.*, vol. 69, pp. 933-997, 1981.
[82] S. C. Rashleigh, "Acoustic sensing with a single coiled mono-mode fiber," *Opt. Lett.*, vol. 5, pp. 392-394, 1980.
[83] —, "Magnetic-field sensing with a single-mode fiber," *Opt. Lett.*, vol. 6, pp. 19-21, 1981.
[84] R. P. DePaula, L. Flax, J. H. Cole, and J. A. Bucaro, "Single mode fiber ultrasonic," this issue pp. 526-529.
[85] W. B. Spellman and D. H. McMahon, "Frustrated-total-internal-reflection multimode fiber optic hydrophone," *Appl. Opt.*, vol. 19, pp. 113-117, 1980.
[86] R. L. Phillips, "Proposed fiber-optic acoustical probe," *Opt. Lett.*, vol. 5, pp. 318-320, 1980.
[87] L. Jeunhomme and J. P. Pocholle, "Mode coupling in a multimode optical fiber with microbends," *Appl. Opt.*, vol. 14, pp. 2400-2405, 1975.
[88] D. Gloge and E. A. J. Marcatilli, "Multimode theory of graded-core fibers," *Bell Syst. Tech. J.*, vol. 52, pp. 1563-1578, 1973.

[89] L. Figueroa, P. L. Lewis, J. L. Pikulski, J. A. Wysocki, and G. L. Tangonan, Hughes Res. Lab., unpublished.
[90] N. Lagakos, W. J. Trott, J. H. Cole, and J. A. Bucaro, "Microbend fiber-optic acoustic sensors," to be published.
[91] N. Lagakos, "Intensity sensors–Microbend," presented at Fiber Opt. Sensor Syst. Workshop, Naval Res. Lab., May 27–29, 1981.
[92] R. O. Miles, A. Dandridge, A. B. Tveten, and T. G. Giallorenzi, "Fabry-Perot interferometric sensor," in *Proc. Conf. Integrated Opt. and Opt. Fiber Commun.*, San Francisco, CA, Apr. 1981.
[93] H. Kressell and J. K. Butler, *Semiconductor Lasers and Heterojunction LED's*, New York: Academic, 1977, pp. 261–265.
[94] A. Dandridge, A. B. Tveten, R. O. Miles, D. A. Jackson, and T. G. Giallorenzi "Single-mode diode laser phase noise," *Appl. Phys. Lett.*, vol. 38, pp. 77–78, 1981.
[95] A. Dandridge, A. B. Tveten, and T. G. Giallorenzi, "Phase noise measurements of six single mode diode lasers," in *Proc. Conf. Integrated Opt. and Opt. Fiber Commun.*, San Francisco, CA, Apr. 1981.
[96] E. Weidel and K. Petermann, "Semiconductor laser noise in an interferometer system," in *Proc. Conf. Integrated Opt. and Opt. Fiber Commun.*, San Francisco, CA, Apr. 1981; also in *IEEE J. Quantum Electron.*, vol. QE-17, pp. 1251–1256, July 1981.
[97] A. Dandridge, A. B. Tveten, R. O. Miles, and T. G. Giallorenzi, "Laser noise in fiber-optic interferometer systems," *Appl. Phys. Lett.*, vol. 37, pp. 526–528, 1980.
[98] L. Goldberg, A. Dandridge, R. O. Miles, T. G. Giallorenzi, and J. F. Weller, "Noise characteristics in line-narrowed semiconductor lasers with optical feedback," *Electron. Lett.*, vol. 17, 1981.
[99] R. O. Miles, A. Dandridge, A. B. Tveten, and T. G. Giallorenzi, "Limitation of diode laser sources in fiber interferometer sensor system," in *Proc. Conf. Lasers Electro-Opt.*, Washington, DC, June 1981.
[100] A. Dandridge, R. O. Miles, A. B. Tveten, and T G. Giallorenzi, "Semiconductor laser sensor: Sources and configurations," in *Proc. European Conf. Integrated Opt.*, London, England, Sept. 1981.
[101] A. Dandridge and A. B. Tveten, "Noise reduction in fiber-optic interferometer systems," *Appl Opt.*, vol. 20, pp. 2337–2339, 1981.
[102] B. D. Evans, "Glass fiber-optic dosimetry," in *SPIE, Vol. 77, Fiber and Integrated Optics*, pp. 88–94, 1970.
[103] B. D. Evans, G. H. Sigel, J. B. Longworthy, and B. J. Faraday, "The fiber optic dosimeter on the navigational technology satellite 2," *IEEE Trans. Nucl. Sci.*, vol. NS-25, pp. 1619–1624, 1978.
[104] A. Dandridge, A. B. Tveten, and T. G. Giallorenzi, "Interferometric current sensors with optical fibers," *Electron. Lett.*, vol. 17, pp. 523–524, 1981.
[105] G. L. Tangonan, D. I. Persechimi, R. J. Morrison, and T. A. Wysocki "Current sensing with metal coated multimode fibers," *Electron. Lett.*, vol. 16, p. 958, 1980.
[106] A. M. Smith, "Polarization and magnetooptic properties of single mode optical fiber," *Appl. Opt.*, vol. 17, p. 52, 1978; A. Papps and H. Harms "Polarization optics of liquid core fibers," *Appl. Opt.*, vol. 16, p. 1315, 1977; S. C. Rashleigh and R. Ulrich, "Magneto optical current sensing with birefringent fiber," *Appl. Phys. Lett.*, vol. 34, pp. 768–770, 1979.
[107] A. J. Barlow, J. J. Ramskov-Hansen, and D. N. Payne, "Birefringence and polarization mode-dispersion in spun singlemode fiber," *Appl. Opt.*, vol. 20, pp. 2962–2977, 1981.
[108] A. B. Tveten, A. Dandridge, C. M. Davis, and T. G. Giallorenzi, "Fiber optic accelerometer," *Electron. Lett.*, vol. 16, pp. 854–855, 1980.
[109] D. H. Leslie, G. L. Trusty, A. Dandridge, and T. G. Giallorenzi, "A fiber optic spectrophone," *Electron. Lett.*, vol. 17, pp. 581–582, 1981.
[110] K. Kyuma, S. Tai, T. Sauada, and M. Nunoshita, "Fiber optical instrument for temperature measurement," this issue, pp. 522–525.
[111] M. Nokes, B. C. Hill, and A. E. Barell, "Fiber optical heterodyne interometer for vibration measurements in biological systems," *Rev. Sci. Instr.*, vol. 49, pp. 722–728, 1978.
[112] P. R. Dragsten, W. W. Webb, J. A. Paton, and R. R. Caprancia, "Light-scattering heterodyne interferometer for vibration measurements in auditory organs," *J. Acoust. Soc. Amer.*, vol. 60, pp. 665–671, 1976.
[113] A. Dandridge, R. O. Miles, A. B. Tveten, and T. G. Giallorenzi, "Noise and spectral properties of single-mode cw diode lasers," in *Proc. Conf. Integrated Opt. and Opt. Commun.*, San Francisco, CA, Apr. 1981.
[114] T. Kanada and K. Nawata, "Injection laser characteristics due to reflected optical power," *IEEE J. Quantum Electron.*, vol. QE-15, pp. 559–565, 1979.
[115] R. O. Miles, A. Dandridge, A. B. Tveten, T. G. Giallorenzi, and H. F. Taylor, "Low-frequency noise characteristics of channel substrate planar GaAlAs laser diodes," *Appl. Phys. Lett.*, vol. 38, pp. 848–850, 1981.
[116] M. Nakawura, Kaiki, N-Chinome, R. Ito, and J. Umeda, "Longitudinal-mode behaviors of mode-stabilized $Al_xGa_{1-x}As$ injection lasers," *J. Appl. Phys.*, vol. 49, pp. 4644–4648, 1978.
[117] C. Voumard, "External cavity controlled 32 MHz narrowband cw GaAlAs diode lasers," *Opt. Lett.*, vol. 1, pp. 61–63, 1977.
[118] R. O. Miles, A. Dandridge, A. B. Tveten, H. F. Taylor, and T. G. Giallorenzi, "Feedback-induced line broadening in cw channel substrate planar laser diodes," *Appl. Phys. Lett.*, vol. 37, pp. 990–992, 1980.
[119] T. Okoshi, K. Kikuchi, and A. Nakayama, "Novel method for high resolution measurement of laser output spectrum," *Electron. Lett.*, vol. 16, pp. 620–621, 1980.
[120] L. Figueroa, K. Lou, and A. Yariv, "Intensity self-pulscutions in (GaAl)As injection lasers operating in an external cavity," *Appl. Phys. Lett.*, vol. 36, pp. 248–250, 1980.
[121] A. Dandridge and R. O. Miles, "Spectral characteristics of semiconductor laser diodes coupled to optical fibers," *Electron. Lett.*, vol. 17, pp. 273–275, 1981.
[122] L. Goldberg, A. Dandridge, R. O. Miles, T. G. Giallorenzi, and J. F. Weller, "Noise Characteristics in line-narrowed semiconductor lasers with optical feedback," *Electron. Lett.*, vol. 17, pp. 677–678, 1981.
[123] A. Dandridge and A. B. Tveten, "Phase noise of single-mode diode lasers in interferometer systems," *Appl. Phys. Lett.*, vol. 39, pp. 530–532, 1981.
[124] Y. Yamamoto, T. Mukoi, and S. Saito, "Quantum phase noise and linewidth of a semiconductor laser," *Electron. Lett.*, vol. 17, pp. 327–329, 1981.
[125] S. Saito and Y. Yamamato, "Direct observation in Lorentzian lineshapes of semiconductor laser and linewidth reduction with external grating feedback," *Electron. Lett.*, vol. 17, pp. 325–327, 1981.
[126] A. Dandridge, A. B. Tveten, and T. G. Giallorenzi, "Single-mode interferometer current sensors with optical fibers and diode lasers," in *Proc. European Conf. Integrated Opt.*, London, England, Sept. 1981.
[127] This method is described in [3]. Other methods are also possible. For example, the laser frequency can be toned. P. Shajenko and E. L. Green, "Signal stabilizing of optical interferometric hydrophones by tuning the light source," *Appl. Opt.*, vol. 19, pp. 1895–1897, 1980; A. Olsson, C. L. Tang, and E. L. Green, "Active stabilization of a Michelson interferometer by an electroptically tuned laser," *Appl. Opt.*, vol. 19, pp. 1887–1899, 1980.
[128] We neglect phase shifts occurring in the combiner. These are constants and therefore do not affect the results of the analysis. See S. K. Sheem, T. G. Giallorenzi, and K. Koo, "Optical techniques to solve the signal fading problem in fiber interferometers," *Appl. Opt.*, Feb. 1982.
[129] S. K. Sheem, "Optical fiber interferometer with 3 × 3 directional couplers: Analysis," submitted to *J. Appl. Phys.*, 1981.
[130] I. J. Bush, "Accurate phase measurement system for a fiber optic interferometer," in *Dig. Conf. on Lasers and Electroopt.*, IEEE/OSA, Washington, DC, June 10–12, 1981.
[131] W. H. Glenn, "Investigation of techniques for the detection of small phase shifts in optical fibers," United Technol. Res. Lab., Rep. R80-925261.
[132] D. A. Jackson, "A prototype digital phase tracker for the fibre interferometer," *J. Phys. E.*, vol. E14, pp. 1274–1278, 1981.
[133] L. Vanmeter, "A bright future for fiber optical sensor systems," *Int. Fiber Opt. Commun. J.*, vol. 2, pp. 19–25, 1981.

Thomas G. Giallorenzi, for a photograph and biography, see *IEEE J. Quantum Electron.*, p. 458.

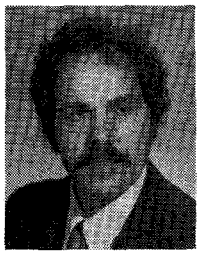

Joseph A. Bucaro received the B.S. and M.S. degrees from John Carroll University, Cleveland, OH, in 1967, and the Ph.D. degree in physics from Catholic University of America, Washington, DC, in 1971.

He joined the Naval Research Laboratory, Washington, DC, in 1971, and carried out research in acoustic surface wave propagation and the mechanical properties of surfaces. In 1973 he formed the Acousto-Optics Section at the NRL and began programs in acoustic imaging, acoustooptic materials, and optical fiber sensors. He became head of the Physical Acoustics Branch, Naval Research Laboratory, in 1978 where he has been managing a number of programs in acoustics and acoustooptics and is continuing research in optical fiber optics.

Anthony Dandridge, for a photograph and biography, see *IEEE J. Quantum Electron.*, p. 564.

G. H. Sigel, Jr., photograph and biography not available at the time of publication.

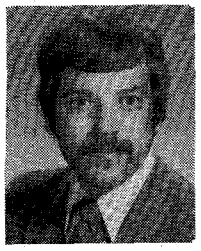

James H. Cole completed graduate work at Pennsylvania State University, University Park, in 1973.

He joined the TRW Defense and Space Systems Group in 1973. Initially, his efforts were aimed at lowering the applicable frequency range of Bragg and Raman Nath imaging systems. An investigation of optical techniques for detection of low frequency sound followed the imaging work. This effort was extended to fiber-optic detection techniques in 1975, and led to one of the first fiber-optic acoustic sensor publications. Since 1978, he has been with the Naval Research Laboratory, Washington, DC, where he directs and performs research investigating fiber sensor transduction mechanisms. He has numerous publications in the areas of acoustooptic imaging and fiber sensor technology.

Scott C. Rashleigh (S'72-M'74) was born in Queensland, Australia in 1949. He was awarded the B.E. and Ph.D. degrees in electrical engineering from the University of Queensland, Australia, in 1971 and 1975, respectively.

For two years he was with the Institute of Advances Studies, Australian National University, where he conducted research in electromagnetic acceleration of macroparticles. From 1977 to 1979 he was an Alexander von Humboldt Fellow at the Max Planck Institute for Solid State Research, Stuttgart, Germany, where he worked on the polarization optics of single-mode fibers and fiber optic sensors. Since 1979 he has been with the Naval Research Laboratory, Washington, DC. His present research interests include fiber optic sensor systems and polarization holding in single-mode fibers.

Dr. Rashleigh is a member of the Optical Society of America.

Richard G. Priest was born in Rochester, NY, on December 19, 1946. After attending secondary school in Rochester, he entered Fordham University, New York, NY, in 1964. He graduated in 1968 with the B.S. degree magna cum laude. He did his graduate work at the Department of Physics, University of Pennsylvania, Philadelphia. While completing his thesis work he held an IBM graduate fellowship. He was awarded the Ph.D. degree in 1972.

He held a postdoctoral fellowship at the Department of Physics, University of Maryland, College Park, from 1972-1974. Following this appointment he won a National Research Council fellowship tenable at the Naval Research Laboratory. In 1976 he became a permanent member of the staff of the Optical Sciences Division, Naval Research Laboratory, Washington, DC. His principal interest is the development and analysis of mathematical models for physical systems. He has worked in the fields of liquid crystals, electrooptic devices, artificial membranes, phase transitions, polymer structure, and fiber optic interferometric sensors. In the latter area, he has worked on models of component performance and of noise generation and propagation. He is currently engaged in a study of detection system distortions and transient response.

Dr. Priest is a member of the American Physical Society.